DEVELOPING AND TAILORING MULTI-FUNCTIONAL CARBON FOAMS FOR MULTI-FIELD RESPONSE

A Dissertation

by

MELANIE DIANE SARZYNSKI

Submitted to the Office of Graduate Studies of
Texas A&M University
in partial fulfillment of the requirements for the degree of

DOCTOR OF PHILOSOPHY

May 2008

Major Subject: Mechanical Engineering

DEVELOPING AND TAILORING MULTI-FUNCTIONAL CARBON FOAMS FOR MULTI-FIELD RESPONSE

A Dissertation

by

MELANIE DIANE SARZYNSKI

Submitted to the Office of Graduate Studies of
Texas A&M University
in partial fulfillment of the requirements for the degree of

DOCTOR OF PHILOSOPHY

Approved by:

Chair of Committee,	Ozden Ochoa
Committee Members,	Harry Hogan
	Dimitris Lagoudas
	J. N. Reddy
	Scott Schaefer
Head of Department,	Dennis O'Neal

May 2008

Major Subject: Mechanical Engineering

ABSTRACT

Developing and Tailoring Multi-functional Carbon
Foams for Multi-field Response. (May 2008)
Melanie Diane Sarzynski, B.S., Texas A&M University;
M.S., Texas A&M University
Chair of Advisory Committee: Dr. Ozden Ochoa

As technological advances occur, many conventional materials are incapable of providing the unique multi-functional characteristics demanded thus driving an accelerated focus to create new material systems such as carbon and graphite foams. The improvement of their mechanical stiffness and strength, and tailoring of thermal and electrical conductivities are two areas of multi-functionality with active interest and investment by researchers.

The present research focuses on developing models to facilitate and assess multi-functional carbon foams in an effort to expand knowledge. The foundation of the models relies on a unique approach to finite element meshing which captures the morphology of carbon foams. The developed models also include ligament anisotropy and coatings to provide comprehensive information to guide processing researchers in their pursuit of tailorable performance. Several illustrations are undertaken at multiple scales to explore the response of multi-functional carbon foams under coupled field environments providing valuable insight for design engineers in emerging technologies. The illustrations highlight the importance of individual moduli in the anisotropic stiffness matrix as well as the impact of common processing defects when tailoring the bulk stiffness. Furthermore, complete coating coverage and quality interface conditions are critical when utilizing copper to improve thermal and electrical conductivity of carbon foams.

In gratitude to my family and friends for their inspiration, encouragement and confidence during the long and arduous journey

TABLE OF CONTENTS

Page

Page

LIST OF FIGURES

FIGURE Page

FIGURE Page

FIGURE Page

FIGURE Page

LIST OF TABLES

1. INTRODUCTION

1.1. Overview of Carbon and Graphite Foams

As technological advances occur in industrial, commercial and military fields, many conventional materials are incapable of providing the unique multi-functional characteristics demanded, driving the need for new material systems. For instance, in thermal management applications such as heat exchangers, thermal conductivity is a critical property while strength and stiffness are also important. In biomedical orthopedic devices, the stiffness is critical and should be tailorable as the bone fracture heals. Carbon and graphite foams provide a distinctive set of properties and features that meet these requirements and act as unique solutions for emerging technologies.

The first generation of carbon foams (reticulated vitreous carbon, or RVC) was developed in the 1960's by pyrolysis of thermosetting polymer foams to obtain a carbon skeleton [1]. RVC foam is a low cost material system for thermal insulation, impact absorption, porous electrodes, filtration and scaffolding. Although many applications take advantage of RVC foam, complete graphitization is not achievable, thus limiting its impact in applications where high thermal conductivity is desirable [2].

A few decades later in the 1990's, the Air Force Research Laboratory (AFRL) discovered a new processing technique (thermodynamic flash) utilizing a mesophase pitch precursor and ignited a new wave of carbon foam research [3-4]. A refined technique using mesophase pitch precursor was developed at Oakridge National Laboratory (ORNL) and led to successful extrusion and casting of carbon foam [5-9]. The ORNL method can also accommodate a coal precursor as demonstrated by researchers at West Virginia University [10-13].

This dissertation follows the style and format of *Composite Materials*.

The thermodynamic flash processing technique begins by grinding mesophase pitch into a fine powder [14-15]. The pitch powder is then pressed into a compact token and placed into a reactor purged with an inert blowing agent such as nitrogen. The chamber is heated under pressure until the mesophase pitch liquefies. When the reactor pressure is released, the absorbed gas expands from thermodynamic instabilities producing the porous foam structure. After cooling to room temperature, the foam is removed from the reactor and stabilized through oxidation to prevent secondary foaming during high temperature heat treatments. Optional post foaming heat treatments include carbonization (1000°C) or graphitization (3000°C), which alter the molecular structure and elicit changes in the mechanical, thermal and electrical material response.

Although there are several variations of processing carbon foam, each method results in a characteristic morphology composed of ligaments and nodes generally classified as open cell. The ligaments, or truss like structures, are curved along their length with a varying triangular cross section. As shown in Figure 1.1, carbon foam nodes are the junction of four ligaments at tetrahedral angles (109.5º) to each other. In RVC foams, the ligaments are more linear in nature forming a polyhedral shaped pore, while in the mesophase pitch based carbon foams, the pores are more ellipsoidal, with a thin shell wall produced between adjacent ligaments. It is possible to minimize this shell feature by altering the processing conditions thus producing a more polyhedral shaped microstructure.

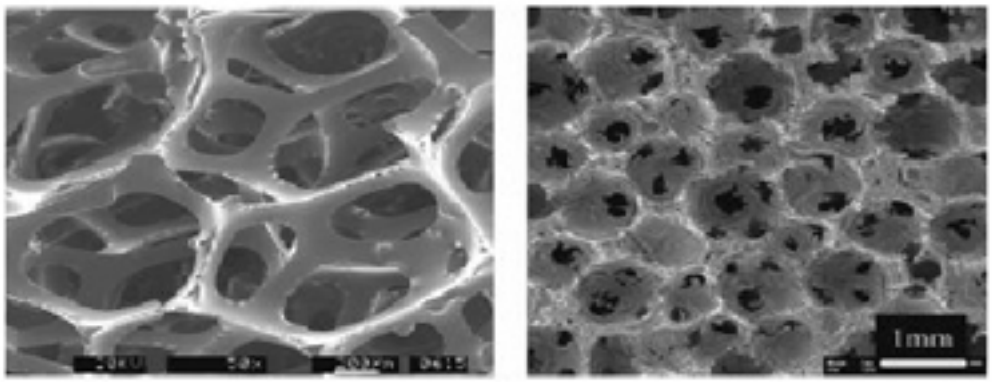

(a) (b)

Figure 1.1. Microstructure in (a) RVC and (b) mesophase pitch carbon foams [16]

The range of typical carbon foam properties are listed in Table 1.1 with carbon fiber (PAN) and solid copper properties included for comparison. Carbon foam properties should be examined on a per unit weight, or specific value, basis as all properties are strongly dependent on foam density; however, the properties in Table 1.1 are presented as available from open literature [14-15].

Table 1.1. Properties of conventional and carbon foam materials

	Density *g/cm³*	Modulus[1] *GPa*	Strength[1] *MPa*	Coefficient of Thermal Expansion *10⁻⁶ 1/°C*	Bulk Thermal Conductivity *W/m-K*	Electric Resistivity *ohm-m*
CARBON FOAM						
RVC [17-18]	0.042	0.031 ~ 0.062	0.28 ~ 1.20	2.2 ~ 3.2	0.085 ~ 0.882	5.00E-04
AFRL [14-15, 19]	0.048 ~ 0.8	0.148 ~ 0.288	1.4 ~ 41	--	0.05 ~ 210	--
ORNL [1, 20-21]	0.25 ~ 0.65	0.144 ~ 0.431	1.0 ~ 3.5	2	0.3 ~ 180	1.2E-2 ~ 3.9E-2
WVU [22]	0.27	0.55	6.2	5	0.25 ~ 25	1E-2 ~ 1E7
CONVENTIONAL						
PAN fiber [23]	1.78 ~ 2.15	230 ~ 390	2400 ~ 3300	7.0 ~ 10.0 (t) -0.5 ~ -0.7 (l)	7 ~ 70 (l)	9.5E-6 ~ 18E-6
Copper [23]	7.5 ~ 8.9	97 ~ 110	125 ~ 310	16 ~ 22	105 ~ 398	1E-8 ~ 17E-8

1) Tensile except for foam properties

When carbon foams are compared to conventional structural materials as in a stiffness design space illustrated in Figure 1.2, they become serious candidates for core materials in sandwich structures. Although carbon foam stiffness is in the range of engineering polymers such as polyethylene, its low density leads to significantly higher specific stiffness. When these same polymers are foamed, this discrepancy in density is alleviated; however, polymer foams cannot achieve the high stiffness of carbon foam. This difference is attributed to the base material involved, as the modulus of carbon/graphite is 3-4 times that of a typical engineering polymer. Carbon foam processing can produce near net shape products through mold selection, and holes, grooves or other fine details can be machined with standard tools resulting in device manufacturing savings [24]. Structural panel applications where carbon foam may be used include offshore crew quarters, aircraft carrier elevator flooring, mirror support structures and impact absorbing automotive panels [14-15, 25].

Heat treatment on the carbon foam alters its material properties allowing them to be tailored to meet specific design specifications. As the heat treatment temperature increases, more order is developed in the carbon molecular structure as indicated in Figure 1.3, leading to increases in the thermal conductivity of the carbon foam [14-15, 26]. Carbon foam specific thermal conductivity has been reported as five times that of conventional thermal management materials such as copper and aluminum [27]. It also has a relatively low coefficient of thermal expansion (CTE) value making it dimensionally stable in high temperature applications. These unique characteristics make it a candidate for many thermal management applications including leading edges, heat exchangers and radiators, fuel cells, brake/clutch cooling and power electronic cooling [14-15, 25, 28]. Carbon foams are also combustion resistant and do not ignite, a critical requirement for offshore and naval application where fire prevention is vital [29].

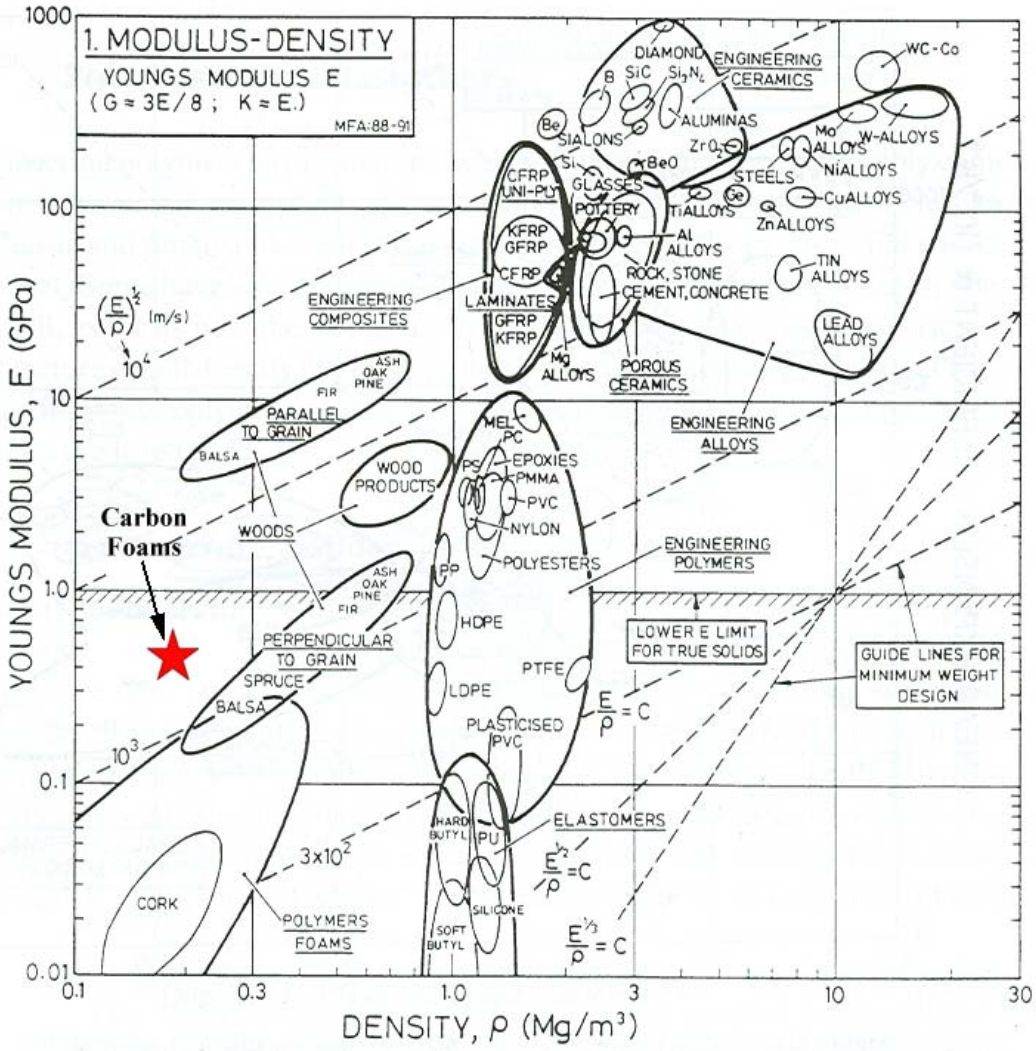

Figure 1.2. Stiffness design space for conventional materials and carbon foams [14, 30]

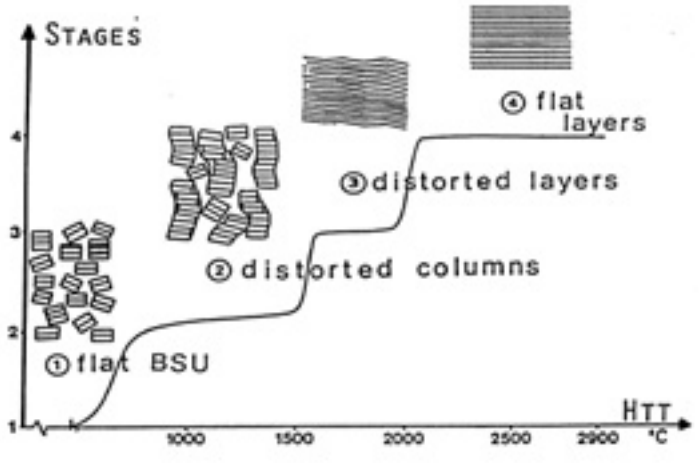

Figure 1.3. Molecular changes in carbon as a function of heat treatment temperature [26]

Beyond these structural and thermal management designs, other applications take advantage of the architecture of carbon foam. The open cell nature makes it a candidate for filtration and catalyst beds, as well as for noise reduction applications [14-15, 25]. Other research is focusing on EMI (electro-magnetic interference) and radar-selective shielding applications in stealthy aircraft [14-15, 31]. Furthermore, carbon foam is under investigation in many biomedical applications such as dentistry and orthopedics.

Although carbon foams show great promise in many applications, the spectrum of possibilities is dramatically increased when designing in multi-functionality. By requiring performance in two or more material response areas, many applications utilizing multi-functional materials become more efficient and simpler in design. Areas of functionality include structural loading, energy storage, power generation, thermal management, sensing abilities, optical characteristics and self-healing or repair functions.

As an example, consider a leading edge application, where multi-functional materials could make a significant impact. Leading edges refer to the front edge of a structure

moving through a fluid medium, i.e. the front edge of an airfoil, a ship's rudder or a turbine blade. In each of these cases, material response requirements are identified, providing a basis for tailoring the material to meet the performance demands. In the example of an airfoil leading edge, the material must meet the structural requirements of the aircraft wing including strength, impact resistance, stiffness and fatigue. From a thermal standpoint, the leading edge must be able to undergo the thermal cycles that occur as a plane goes from ground temperature to a cold soak at altitude and return to the ground throughout the lifetime of the aircraft. Furthermore, it might be beneficial to increase the functionality of the wing by adding an optical quality by incorporating reflectors or lights into the wing structure. Perhaps the wing material might generate power and store energy, serving as a battery for the electronic components. In order to meet all of these requirements, it is necessary to consider material systems that can be tailored to create an optimal response in each functional area.

Two main categories of multi-functionality are of interest in the carbon foam material system—to improve and/or tailor mechanical stiffness and strength, and thermal and electrical conductivities of carbon foams. Although these foams have low densities, their specific strengths and stiffness do not yet meet critical structural performance requirements. Some work has been undertaken to improve this by incorporating the foam into a sandwich structure, however the brittle failure mode of the carbon foams leave these panels at risk for catastrophic failure with little warning [25]. In addition to improving the overall strength and stiffness, there are certain applications that require tailoring of these properties over time. For instance, in biomedical orthopedic devices typically using titanium metals, the stiffness of the device is often several orders of magnitude higher than that of the bone [32]. This leads to stress shielding as the bone undergoes the healing process, and results in weaker bone formation post healing. If however, a device could be manufactured which more closely mimics the properties of bone in the initial stages of healing and then slowly degraded in stiffness throughout the healing process, the resulting healed bone would be stronger over the life of the patient.

The second area of multi-functionality is improvement or tailoring of the thermal and electrical conductivities. The carbon foam community is currently focused on utilizing processing changes, such as heat treatments, to achieve higher conductivities. Specifically by heating the carbon foam to graphitization temperatures, order develops in the molecular structure leading to higher conductivities in all directions. It is of interest, however, to tailor the conductivity in specific directions or along given paths creating functionally gradient behavior. As an example, consider transforming a block of carbon foam into an electric circuit where a region of the carbon foam acts as a power source, or battery, while individual ligaments are transformed into positive and negative leads connecting other devices embedded elsewhere in the foam. In this case, the electrical conductivities of individual ligaments must be tailored to avoid interference and short-circuiting.

In order to achieve these two areas of multi-functionality in mechanical, thermal and electrical response, several mechanisms for altering the carbon foams are currently under investigation. The precursor material—polymer, mesophase pitch or coal—is one tailorable parameter. Carbon foams produced from mesophase pitch are thermally and electrically conductive, while polymer and coal precursors are naturally insulative. In addition, each of these precursors has varying elastic moduli and strength as a direct result of differing geometric morphologies and ligament compositions.

Additional tailorability is achievable through alteration of the carbon foam microstructure by changing the processing variables (blowing agent, pressure, temperature, et cetera). Furthermore, additives may be incorporated into the precursor base material to enhance material response. As an example, Lafdi et al. focused on carbon fibers and nanotubes, silver particulate and exfoliated graphite as additives to improve the mechanical response of carbon foams by altering the anisotropy of the molecular structure [14-15]. Finally, heat treatments are also used to tailor the carbon

foam with higher temperatures producing higher thermal conductivity values as more order is developed in the molecular structure.

The final method to achieve multi-functionality is with post-foaming alteration. This includes coatings or infiltration with polymeric, ceramic or metallic materials. Consider an application where the strength and stiffness requirements are met only by carbon foam produced with a polymer precursor. By coating this initially insulative carbon foam, the thermal and electrical conductivities can be significantly improved to meet other functional requirements. In the reverse case, consider a thermal radiator application utilizing high thermal conductivity carbon foam. In order to meet the structural requirements, the carbon foam could be combined with composite face sheets to form a sandwich panel with high strength and stiffness.

1.2. Literature Review

1.2.1. Analysis of Porous Materials

Analytical modeling of porous materials, or foams, is an extensive research area where the initial step is determination, or assumption of how the ligaments, or struts are connected to form the microstructure. Other considerations are the classification of the foam as either open or closed cell, which determines other assumptions, used in the analysis.

Ko determined equivalent elastic constants for foamed elastomers in the mid 1960's, where the ligament structure is based on interstitial space for close packed spheres of identical size [33]. Two packing configurations—face centered cubic and hexagonal—were considered where both have a packing density (or void content) of 0.74. An equilateral triangle was used to approximate the cross section of the ligament and was

uniform along the length. Beam theory was used to find the deformation of each packing configuration and the effective elastic modulus and Poisson's ratio were calculated based on the slenderness ratio (l^2/A) of the ligaments. Finally, the results of the two configurations were combined using a rule of mixture formulation to account for varying void geometries in actual foams. The result of this work is a direct relationship between equivalent mechanical properties, both modulus and Poisson's ratio, and the void density, or porosity, for a given foam. For both configurations, as the slenderness ratio increases (void density increases), the effective Poisson's ratio increases while the effective modulus decreases as shown in Figure 1.4.

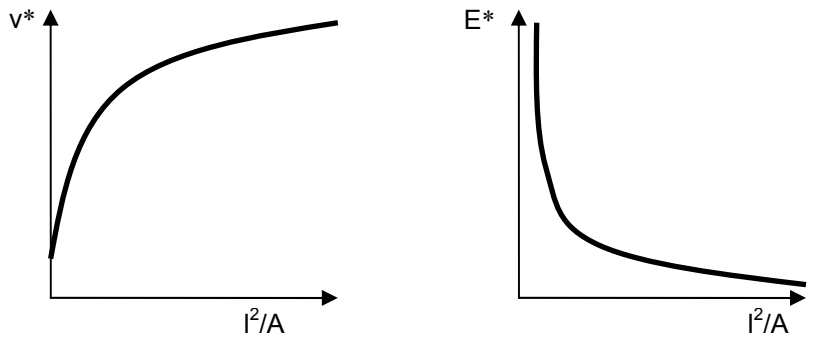

Figure 1.4. Effective mechanical properties as a function of ligament slenderness ratio for work of Ko [33]

In the 1980's, Christensen focused on finding effective property relationships in both open and closed cell foams [34]. In this study, both cell classifications were investigated for three-dimensional isotropic materials. Randomly oriented struts, or ligaments, were connected in such a way to ensure isotropic bulk behavior. Each strut was uniform in cross section with load transfer accomplished through axial deformation. The formulation accounts for the stress and strain in an individual strut and then averages over every possible orientation in three-dimensional space. The resulting relationships further verified a direct relationship between effective mechanical properties and the void volume fraction. In the case of open cell foams, the effective Poisson's ratio is found to be independent of the material (ν=1/4) while the effective modulus is a linear inverse relationship as shown in Figure 1.5.

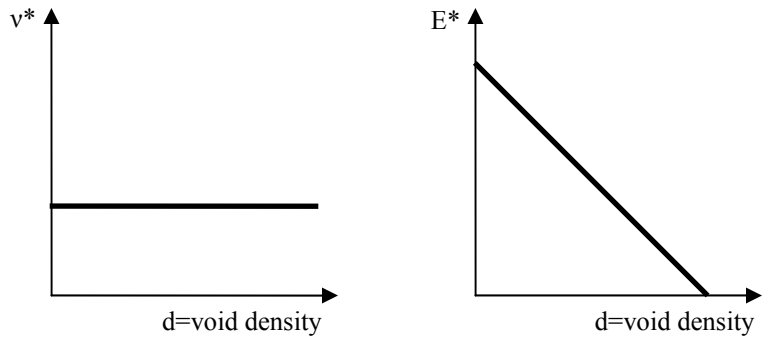

Figure 1.5. Effective mechanical properties as a function of void density in work of Christensen [34]

Using a similar approach, Warren and Kraynik used a regular tetrahedral unit cell randomly oriented to generate isotropic mechanical properties [35]. Four half struts, or ligaments, were modeled to join at equal angles to the node. The ligament cross section was allowed to vary along its length with deformation in both bending and axial modes. The effective stress and strain values for the unit cell was calculated and then averaged

over all possible orientations to determine effective properties for the foam structure. When considering uniform triangular struts, the effective properties are again directly proportional to the void volume fraction, or porosity, and show a form similar to that found by Ko in Figure 1.4.

Later studies by Warren and Kraynik used a higher order polyhedral unit cell known as a tetrakaidecahedron [36]. This fourteen-sided unit cell was placed on a body centered cubic lattice to fill space creating an open cell foam configuration and anisotropic response. Using constant cross section struts, beam theory was used to evaluate effective properties for the bulk foam where deformation in bending, stretching and twist was allowed. Several different cross sectional shapes were considered including circular, square, triangular and a plateau border. As in their previous work, the effective properties were dependent on porosity and the elastic properties were similar to the relationships depicted in Figure 1.4.

Gibson and Ashby simplified the analysis by using relative density to eliminate any geometric constants and extend the effective property relationships to an arbitrary periodic structure [30]. Initially, a cubic unit cell of ligaments was assumed where the cross section was square and constant along the length. Additionally, adjacent cells are offset with joining at the midpoints. Deformation was determined through beam theory analysis for a compressive loading scenario. Finally, to remove the geometric constants, the second moment of inertia and the relative density were assumed proportional to ligament dimension relationships. Therefore, the resulting effective moduli each have a geometric constant of proportionality used to fit experimental data. The results again confirm that the effective moduli are a function of the overall porosity of the foam where decreasing relative density (increasing porosity) leads to linearly decreasing moduli as in Figure 1.5. Furthermore, the effective Poisson's ratio was found to be constant and a function of the two proportionality constants in the effective moduli functions.

Porous material analysis relies on volumetric averaging of stress and strains to predict effective properties for the bulk foam. In addition to the above methods that assume a periodic microstructure, other techniques can be applied without this assumption and are useful when considering closed cell foam morphologies. For these types of structures, ellipsoidal shaped pores are assumed and effective moduli predicted using techniques such as Composite Spheres Model, Generalized Self-consistent Method or Mori-Tanaka Method [37-41]. When using these averaging schemes other assumptions are invoked, and in most cases void-void interaction is not considered, thus limiting their application to open cell morphologies with high porosity, as in the case of carbon foams.

As a final component of micromechanics approaches to porous materials, bounds on effective properties can be generated to narrow the range of possible predictions and provide a quantitative method for evaluating the validity of each approach. The Voigt and Reuss bounds are the least conservative and were developed through energy minima assuming uniform stress and strain fields [42]. The lower bound (Reuss) mimics springs in series, while the upper bound (Voigt) is analogous to springs in parallel. Both of these bounds take the form of weighted combinations of the individual constituents' properties as in the rule of mixtures.

The Hashin-Shtrikman bounds were also developed through minimum principles of elasticity, but by introducing admissible stress and strain fields [43]. The upper and lower bounds are higher order combinations of the constituent properties and their respective volume fractions. Unlike the Voigt-Reuss bounds, these bounds take into account both constituent moduli in predicting individual effective moduli. Without any assumption regarding constituent geometry, Hashin-Shtrikman bounds are the most restrictive bounds on isotropic effective properties that can be formulated for isotropic constituents [42].

Although each of the above micromechanics approaches addresses the mechanical properties, each can be generalized and extended to thermal and electrical predictions. In the case of effective thermal conductivity, there are four contributions to heat transfer—conduction through the solid, conduction through the pore, convection in the pores and radiation through the pore walls and across the voids. The two conduction modes are the most important with convection playing a negligible role based on the geometric characteristics of existing foams [30]. Radiation, on the other hand, can play a significant role in heat transfer through porous media especially at low relative densities (high porosity). However the majority of the approaches to effective thermal conductivity prediction focus solely on conduction as means of heat transfer.

Furthermore, coatings or infiltrations of the porous structure are readily integrated into the volume averaging techniques by considering an additional constituent phase [37-41]. In the case of infiltrations, the void space is replaced with the infiltration material maintaining a two-phase system. By assuming a complete infiltration (no void space remaining), the second phase is considered perfectly bonded to the ligament structure and the system can be thought of as spherical particles of the infiltration material embedded in a solid matrix phase (carbon).

To include coating in porous media analysis techniques, two courses of action are available. The first is to generate an equivalent ligament using a rule of mixtures approach on concentric cylinders. In this case, a uniform coating is placed around a characteristic ligament (length and cross section) and effective ligament properties are generated similar to springs in parallel. This equivalent ligament is used in the existing approaches with the condition that the ligament constitutive properties remain isotropic. A second approach to modeling coatings is to assume a three-phase system—void, ligament and coating—again maintaining the isotropic nature of each individual constituent. Both approaches generate effective moduli and conductivities for uniform, perfectly bonded coatings on periodic structures.

Some researchers have progressed beyond the assumed periodic unit cell assumptions in predicting effective property values by using experimental data of the microstructure to generate finite element analysis (FEA) models. Garboczi and Day developed a technique to compute effective elastic properties of random heterogeneous solids without the required periodic boundary condition by relating the problem to a network of springs [44]. The approach is applicable on an arbitrary digital image in either two or three dimensions, obtained using optical microscopy, X-ray micro-tomography, serial sectioning or magnetic resonance imaging (MRI). For instance, each pixel in a two dimensional X-ray image was considered a linear finite element, and standard FEA techniques used to solve the spring network. By applying strains and computing stresses, the effective properties were determined using volume averaging methods described previously. This method accounts for the maximum resolution of the image (one pixel equals one finite element) and is adaptable to higher order elements, as well as to three-dimensional images where each voxel (three-dimensional equivalent to a pixel) is considered a single hexahedral element.

This methodology has been used to find the effective elastic properties of sandstone samples by Arns et al. [45]. In this case, X-ray computed tomography was used to generate image data for a core of Fontainebleau sandstone. These images showed a bimodal grayscale distribution, one for void space the other for grain structure. The predicted effective moduli were in agreement with the wide range of experimental data available. After verifying the model, further studies were undertaken to generate effective properties for dry, water saturated and oil saturated conditions, which were also in good agreement with experimental values.

A similar approach was used in biomedical research, where it has been shown that the grayscale values of individual pixels on an X-ray image can be correlated directly to Young's modulus value or spring stiffness [46]. Using this constituent information, the previously discussed averaging schemes can be used to predict overall effective

properties of bones. Micro-CT X-ray imaging was undertaken at specified stages of healing through the life of the patient in order to generate effective time dependent properties. This information is especially useful in determining the best orthopedic devices (pins, plates, screws, et cetera) to use for a given fracture classification.

Furthermore, the image based analysis techniques are extendable to thermal material response as demonstrated by Saadatfar et al. on polymeric cellular foam products [47]. In this study, several specimens were considered with varying porosity values. From individual segmented images, approximate density values were obtained for the overall foam and compared favorably with nominal densities measured on a larger specimen. Additional material property predictions obtained directly from the segmented images include porosity, pore/solid volume to surface area and the relative interconnectivity of the material. The final study used the three-dimensional microstructure where each voxel was considered a resistor and volume-averaging techniques were used to predict effective thermal properties for the polymeric foam.

A few researchers have progressed further than spring networks in image based modeling for prediction of effective properties. In these cases, more complex steps are undertaken in converting the raw image information into acceptable finite element models. The focus of this effort is to closely mimic imaged geometries (foam architectures, et cetera) without conforming to the inherent voxel grid. By using these techniques, the influence of specific geometric phenomenon (bent ligaments, holes, et cetera) can be isolated. In research by Jaecques et al., micro-CT (computed tomography) X-ray images were processed using a software package to segment and reconstruct bone geometry [46]. An analytical surface was generated to represent the outer bone surface, and subsequent meshing was completed to generate a FEA model. This research also investigated bone scaffolds fitted to a particular bone defect, such as a tumor removal, captured through micro-CT X-ray. The outer geometry of the scaffold

engages precisely with the defect shape, while device porosity is altered for optimal stiffness response during healing.

Youssef et al. has used similar methods on images of polymeric foam from X-ray tomography to generate a computational model of the foam microstructure [48]. Initially each serial section image was processed to reduce noise. Next, a surface consisting of triangular elements was created to describe the air-solid interface from which a solid mesh is defined. Analysis variables investigated include mesh density, material property input and boundary conditions with a focus on the elastic response of these foams.

Other research has focused on algorithms to computationally generate random structures on which the above effective property prediction techniques are applied. By statically generating these microstructures rather than directly imaging them, the impact of microstructural changes on effective properties is determined through an optimization study. It is also possible to study other cellular materials, such as sponges, cork or bone which are not created through a traditional foaming physics. Roberts and Garboczi describe several techniques for generation of an open cell solid from a random three-dimensional seed point Monte-Carlo distribution [49]. Voronoi tessellation was used to create the random cellular microstructure. By growing spheres from each seed point and stopping growth when two spheres contact, the resulting pore represents the region of space that is nearest that particular seed point. This concept is similar to the actual process of liquid foam formation. Roberts and Garboczi also undertook another technique where the random seed points were connected to their nearest neighbors to create a ligament network of beam elements. This approach was used approximate the microstructure of cellular solids such as cork or bone.

Research by Ravindran et al. to predict effective thermal conductivity in dendritic regions details another methodology [50]. Dendritic regions form as molten metal cools, and are geometrically similar to a network of ligaments. In this approach, random

geometries were formed from computational algorithms based on the physics of dendrite growth. From the generated geometries, effective properties were generated through the previously described methods.

1.2.2. Processing and Characterization of Carbon Foam

Considerable research efforts were undertaken to understand the processing conditions required to produce certain morphologies in early carbon foam research. Sandu and Hager were some of the first to investigate the effect of processing variables on the carbon foam morphology [51]. The specific processing procedure began with heating of the mesophase pitch under pressure until the bubble nucleation sites reach equilibrium. From these critical nuclei, the model predicts the transient bubble growth from diffusion, the minimum distance between adjacent bubbles during growth and average distance between bubbles at the initiation of cooling. The result is a set of mathematical equations relating processing variables (pressure, temperature and blowing agent concentration) to geometric outcomes such as pore radius, total number of pores, distance between adjacent pores and void fraction.

Further investigation of processing conditions on pore, or bubble, formation was undertaken by Rosebrock et al. to understand both growth and movement in mesophase pitch carbon foams [52]. The results indicate that although bubble movement does occur, when compared in magnitude to the bubble growth, it can be neglected. Parametric studies were then undertaken to investigate specific contributions of pressure, viscosity and bubble radius to final morphology.

Another contribution to process modeling is the effort of Beechem et al. to remove the assumption of spherical bubble growth [53]. In this research, the bubbles were allowed to grow in an elliptical fashion as the mesophase pitch foams. Initial pressure and radius

of the bubble along with viscosity were identified as important processing variables. A correlation between these variables, bubble growth and final shape was identified which emphasizes how controlled foaming can be achieved.

Further research was conducted to characterize the geometric features present in carbon foams. Anderson et al. undertook the initial studies to identify the microstructural unit cell [54]. The effort used experimental observation under optical light microscope (OM) and scanning electron microscopy (SEM) to ascertain the preferred structure in carbon foams. The investigation concluded that carbon foam structure is characterized by ligaments formed by three intersecting faces meeting in groups of four at the nodes. Dodecahedral-like cells were observed with the majority of the faces being five sided and a small number of four or six sided faces. From these observations, the task of finding a space filling unit cell composed of irregular polyhedral with mostly five sided faces was undertaken. The result was a geometric model of the carbon foam useful for generating statistical parameters—solid angles, ligament lengths and face angles—regarding the geometry not previously available.

Hager identified an alternate unit cell configuration that meets the criteria observed by Anderson et al. [55]. Point lattices with spherical bubbles were investigated to find one that produced the geometric structure required. The result is spherical bubbles placed on body centered cubic lattice, creating a polyhedral unit cell referred to as a tetrakaidecahedron. This meets most of the observed geometric features, but is unable to fulfill the requirement for four ligament intersection at a tetrahedral angle. It does, however, meet the space-filling requirement, and serves as one geometric basis for micromechanics modeling of carbon foam deformation and effective properties.

A novel technique for characterizing the microstructure of carbon foams was developed by Maruyama et al. [56]. In this work, serial sectioning was employed to capture the foam microstructure directly using an automated system composed of a polishing stage,

cleaning station and bright field microscope. For each serial section, a sequence of high magnification images were obtained and then stitched together to form a single high-resolution image. The compilation of images was then used to reconstruct the carbon foam microstructure following manual preparation of individual images to correct image processing defects.

Additional research on carbon foams focused on characterizing the anisotropic nature of carbon foam. Mukhopadhyay et al. studied the structural and chemical characteristics of pitch foams under SEM, transmission electron microscopy (TEM) and X-ray photoelectron spectroscopy [57]. Chemically, the carbon atoms are bonded in a manner analogous to single crystal graphite. Folds of these graphene layers are present in the carbon foam ligaments and cell walls. This indicates a highly anisotropic ligament in graphitized carbon foams.

The graphitization aspect of carbon foams was further investigated by Mehta et al. [58]. The objective was to characterize the degree of graphitization possible in carbon foams produced from two different mesophase pitch processing methods. The results compare favorably with values obtained from carbon fibers spun from the same precursor. Other findings suggest that the fragile nature of the graphitic foam is due to defects in the ligament structure that develop during the foaming procedure not the heat treatment processes. Therefore, refinement of the processing procedure is required to improve the overall strength of the graphitic foams.

Additional characterization of the carbon foam anisotropy was undertaken by Klett et al. [59]. In this work, two mesophase precursors were identified and underwent the same foaming procedure and graphitization heat treatment. Using optical and polarized light microscopy, SEM and X-ray diffraction, the graphitic nature of each foam was characterized. Additional thermal conductivity experiments were also conducted to determine the effect of precursor on thermal performance. The results indicate that the

graphitic characteristics—lattice parameters and thermal conductivity—are insensitive to a particular precursor material, but are dependent on the processing variables such as pressure and temperature.

1.2.3. Analysis of Carbon Foams

The analysis of carbon foams has focused on applying the porous media techniques to the carbon foam based on the characterization findings in section 1.3.2 of its geometric microstructure. The tetrakaidecahedron unit cell identified by Hager as a space filling periodic cell configuration in carbon foams was further investigated by Li et al. using energy methods [60]. The struts, or ligaments, were assumed isotropic and linearly elastic with constant cross sectional areas along the length. Each strut was allowed to deform according to beam theory with Castigliano's second theorem used to calculate the deformation. Several cases of cross section were investigated—circular, trigonal and square—and effective isotropic properties calculated. The results indicate that effective properties depend on the overall density, strut cross section and strut properties.

Using a tetrahedral shaped unit cell with triangular cross section ligaments, Shin and Roy analyzed the carbon foam first as a series of beam elements and secondly as a solid three-dimensional mesh [19, 61]. In generating the geometry, spheres are subtracted from a tetrahedral solid to form the representative volume element. By varying the sphere size, various porosity values are obtained ranging from open to closed cell classifications. The resulting effective properties were determined through a volume-averaging scheme as the unit cell was rotated through all possible orientations. In addition to relating isotropic ligament properties to overall bulk properties, this work aimed to investigate the effect of anisotropic ligament properties. It was determined that the transverse Young's modulus and shear modulus of the ligaments were more significant than the longitudinal Young's modulus in the effective bulk mechanical

properties confirming that analysis should include bending effects in addition to axial stretching of the ligaments.

Since the carbon foam can be graphitized resulting in high conductivities, additional research has been conducted to predict the effective thermal material properties using extensions of the porous media techniques. For instance using a periodic cubic unit cell, Yu et al. studied heat transfer and fluid flow in porous carbon foam [62]. The heat transfer model incorporates the exposed surface areas and the void opening size as a function of porosity and pore diameter. Major assumptions include uniform voids represented as spheres centered in a cube. These pores are regularly arranged in space where each pore connects with six adjacent pores on each of the unit cell faces. This arrangement creates ligaments with four curved faces rather than the characteristic triangular cross sectional shape. The pure conductive heat transfer model was developed through the analogy of series and parallel circuits. The resulting relationship shows that effective conductivity decreases with increasing porosity due to the reduction of the solid phase material, and it was shown in good agreement with experimental values.

Tee et al. developed an approach to modeling the carbon foam microstructure in an effort to identify the impact of porosity, morphology and temperature on the overall thermal conductivity [63]. This model consisted of randomly oriented and distributed cubic cells formed by twelve struts with square cross sections and eight cubic junctures. The struts were considered anisotropic with the longitudinal and transverse directions having independent properties, along with the junctions where graphitic folding occurs. The heat conduction relationship in an individual cell was developed using a parallel and series approach to thermal and electric resistors. The resultant relationship was averaged over all possible orientations forming an effective thermal conductivity for the graphitic carbon foam. The model was also refined to account for non-prismatic struts by using a parabolic relationship to describe the strut curvature on each face, while maintaining the cubic juncture and cell shape. The study found that the juncture significantly reduced

the overall conductivity since graphitic crystal misalignment is prevalent in these areas. In addition, the transverse conductivity of individual ligaments was negligible and the focus should be on identifying a proper longitudinal conductivity for high bulk thermal conductivity.

In summary, the focus of carbon foam analysis to date has been on understanding and improving the processing to morphology correlation in order to produce foams with desired property ranges. Even though some architectural features were included, they are generally limited to a periodic unit cell representation to predict effective properties. Very few researchers have analytically addressed thermal-electrical or thermo-mechanical tailorability and most studies are limited to isotropic constituents ignoring the anisotropy present in graphitized carbon foams.

1.3. Research Objective

The research objective is to develop comprehensive microstructure based analytical models to design and predict the coupled field response of multi-functional carbon foam at multiple scales.

By approaching the problem at multiple geometric scales, the role of geometric features—curved ligaments, as-foamed geometries, filament bridges, holes and changing cross sections—is identified. In addition, the impact of geometric scale and the consequences of certain common idealizations on prediction of effective properties are identified. By incorporating anisotropy at the ligament scale as well as coatings and infiltration, a design parameterization problem is established to provide essential feedback to the processing researchers who are creating and experimentally characterizing these multi-functional carbon foams.

Finite element analysis serves as the analytical approach, with the computational mesh generated directly from micro-CT (computed tomography) X-ray images, which capture the precise three-dimensional morphology of the carbon foam. The design space consists of anisotropy of individual ligaments and various coatings and infiltration, including imperfect coverage or bonding. The fields under investigation include pure mechanical and thermal boundary value problems (BVP), sequentially coupled thermo-mechanical BVPs and fully coupled thermal-electrical analysis problems. Qualitative inferences on material response include alteration of the stiffness, strength and thermal or electrical conductivities. The overriding principle for multi-functionality is to increase strength and stiffness while controlling thermal and electrical conductivities to meet specific design objectives.

2. ANALYTICAL FOUNDATIONS

2.1. Carbon Foam Characterization

2.1.1. Microstructure

Many optical methods are used to visualize the carbon foam and characterize its microstructure. Initial visual inspection identifies gross changes that occur when changes to the processing parameters are attempted. This qualitative inspection identifies the degree of foaming, the resulting surface finish and possible fracturing during processing.

More quantitative visual analysis is completed with the use of optical light microscopy (OM). Initially, a small sample of processed carbon foam is infiltrated with epoxy using a vacuum system. After curing, the sample is polished using standard procedures and then examined under the microscope as in Figure 2.1. By isolating the specimen cross section, a statistical pore size distribution is identified by measuring the pore diameters [14-15]. This information is valuable in determining the uniformity of the pores along the foaming direction and identifying density gradients. Other statistical information available through OM analysis includes ligament length and diameter distributions. Finally, OM images also provide qualitative information regarding the characteristic shell feature typically appearing in pitch based carbon foams.

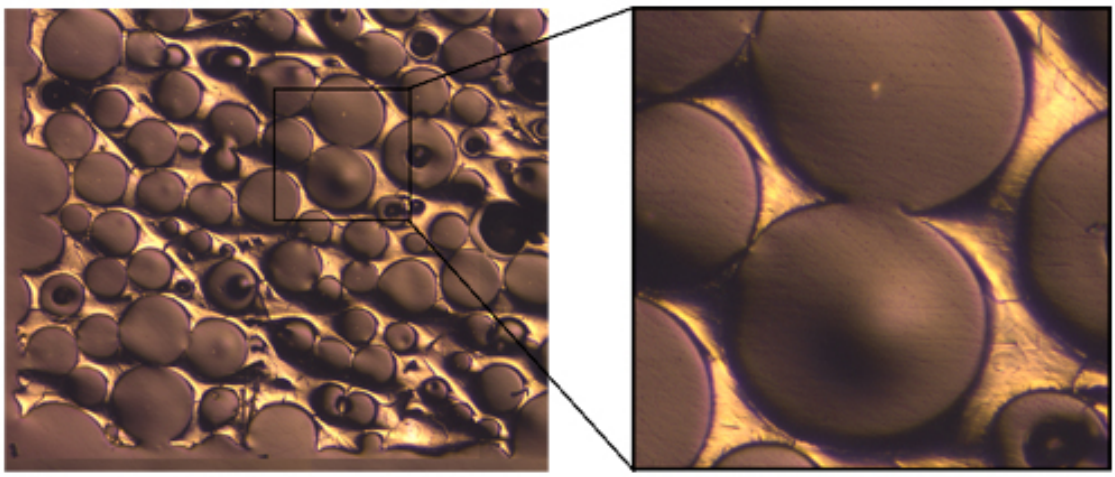

Figure 2.1. Polished mesophase pitch carbon foam cross section under optical microscope

Scanning electron microscopy (SEM) or transmission electron microscopy (TEM) provides additional insight into pore shape, degree of open cell porosity and interface quality between additives or coatings and the carbon foam substrate. The shell feature is readily apparent under SEM and the integrity of the pore wall is qualified.

Although the above methods provide much needed information regarding the foam morphology, they are limited to a two-dimensional plane of information. Only through additional polishing steps or slicing can additional cross sections be investigated. A final observation method, micro-CT (computed tomography) X-ray, is used to generate three-dimensional information about the carbon foam morphology including the precise ligament cross section with any tapering, bending or twisting along its length. Micro-CT also captures any artifacts in the foam—small holes, filament bridges, or un-characteristic node geometries such as those in Figure 2.2—for incorporation into the analytical model.

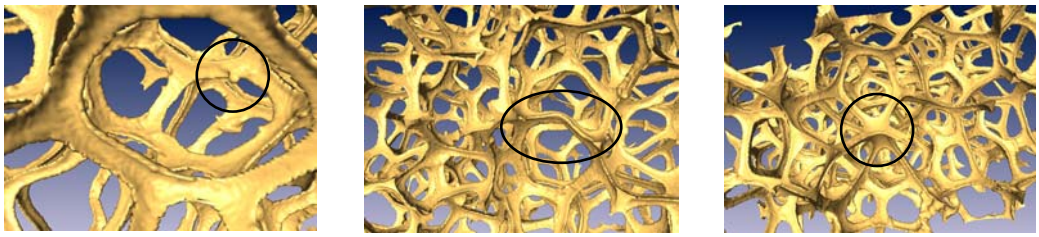

(a) (b) (c)

Figure 2.2. Captured processing artifacts in carbon foam
(a) globule (b) bent ligament and (c) double node

The SkyScan 1172 micro-CT X-ray system is used to generate high resolution images of processed carbon foams [64]. The maximum resolution of this system is 5 μm which precludes the capturing of thin, 2-3 μm, coatings. In addition, metallic coatings tend to shield the X-rays thus preventing the imaging of a thicker copper coating or a complete infiltration. A schematic of a general micro-CT X-ray system is in Figure 2.3, where the specimen is fixed and the X-ray source and detector rotate during the scan. A typical X-ray image, such as Figure 2.4 is generated every few degrees through a complete 360 degree rotation [65].

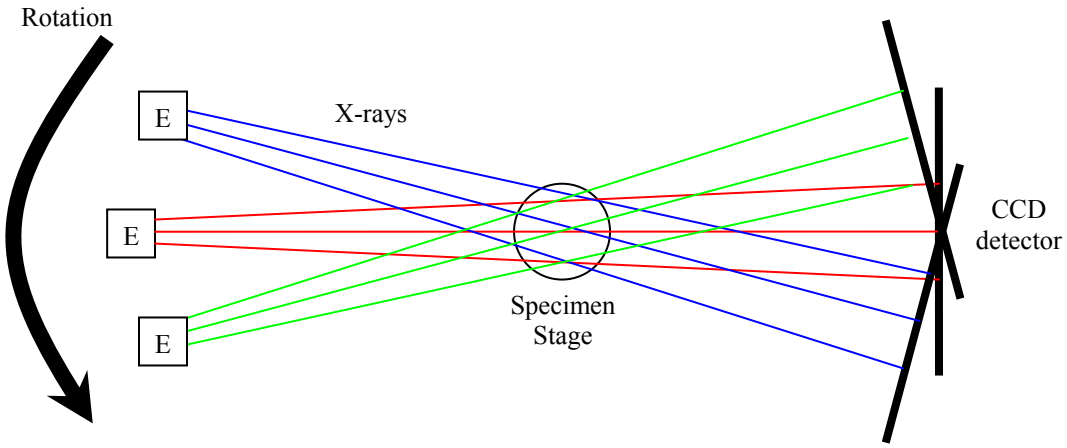

Figure 2.3. Schematic of a micro-CT X-ray system

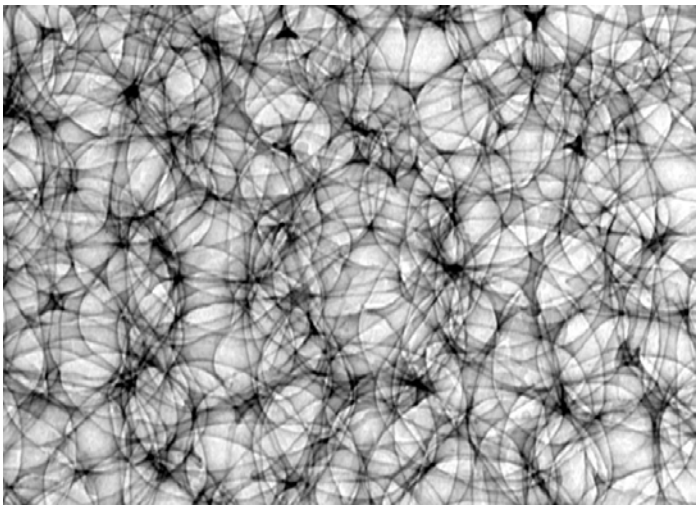

Figure 2.4. X-ray image from carbon foam scan with micro-CT system

After generating these X-ray images, the next step is to reconstruct the data into two-dimensional slices. Initially, the first and last X-ray images are checked for alignment. These two images are taken of the same image plane; however due long scan times usually over several hours, the samples occasionally shift position creating misalignment across the full rotation. If the alignment is poor, the scan must be repeated. If the alignment is good, the reconstruction parameters are entered and the dataset can be processed further.

This reconstruction process can be described conceptually by considering an empty cube split into voxels, or three-dimensional pixels. For each CCD X-ray image, darken the voxels according to the original grayscale images which shows where matter is detected. Rotation through all the CCD images (360°) results in some of the voxels being very dark, while others are lighter in intensity based on what is detected at the various angles of rotation. Then a computer algorithm is used to reconstruct this data into two-dimensional planes which are perpendicular to the axis of rotation as depicted in Figure 2.5 [66]. An example of a reconstructed image from a carbon foam scan is shown in Figure 2.6.

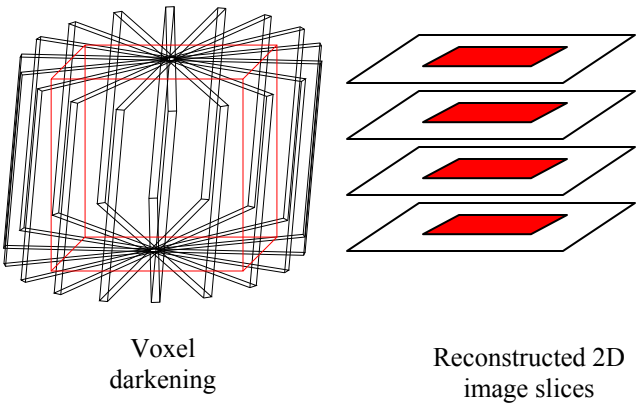

Figure 2.5. Conceptual description of micro-CT X-ray image reconstruction procedure

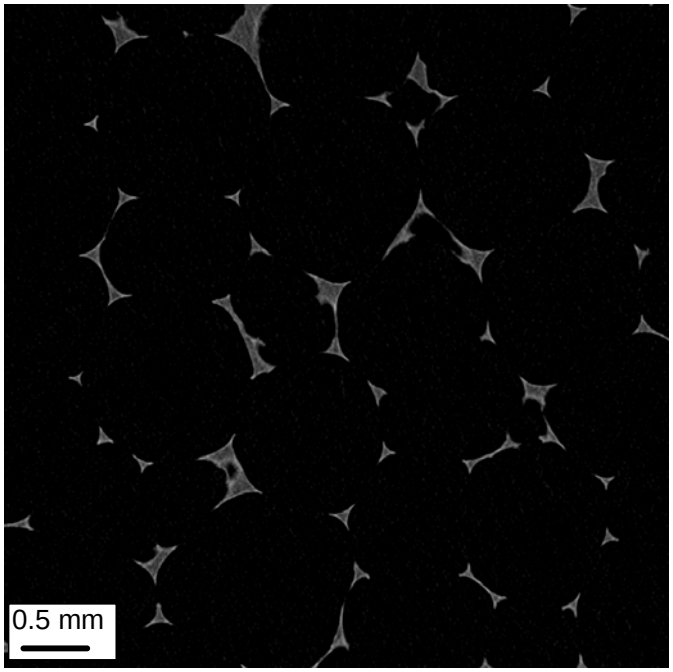

Figure 2.6. Reconstructed image from micro-CT X-ray scan of carbon foam

Each individual reconstructed image represents a two-dimensional plane of information similar to the optical microscopy data and consequently can be used to identify pore distribution, ligament length or other statistical data. However, the full set of reconstructed images can be used to create a three-dimensional representation of the carbon foam morphology. For example, using special rendering algorithms described in the next section, it is possible to study the morphology in a virtual three-dimensional environment using a stereo-projector. In this case, two simultaneous images of the digital model are created from slightly different perspectives. By wearing special anaglyph glasses (one red lens, one blue), the human brain is tricked into seeing a third dimension thus generating depth perception for the models. This type of rendering is highly useful when investigating complex three-dimensional data sets or models and can provide insight beyond traditional two-dimensional projections of the data.

In addition, micro-CT X-ray is a nondestructive evaluation of the morphology unlike more traditional serial sectioning via polishing. Therefore, scanned samples may be taken into an experimental laboratory to generate data for comparison to any computational models generated from the X-ray data, providing a unique ability to independently validate models from a single source.

2.1.2. Material Anisotropy and Crystallinity

In addition to characterization of the carbon foam morphology, additional investigation of the microstructure is undertaken to understand the molecular structure of the individual ligaments. When carbon foams undergo post processing heat treatments such as carbonization or graphitization, the molecular structure of the ligaments undergo changes. As the heat treatment temperature increases, more order is developed in the molecular structure of the graphene planes as shown in Figure 1.3. If complete graphitization is achieved, a hexagonal crystal structure emerges as seen in Figure 2.7,

where the carbon atoms are bonded into layers. In order to qualitatively observe the degree of anisotropy, carbon foams are studied using optical polarized light microscopy.

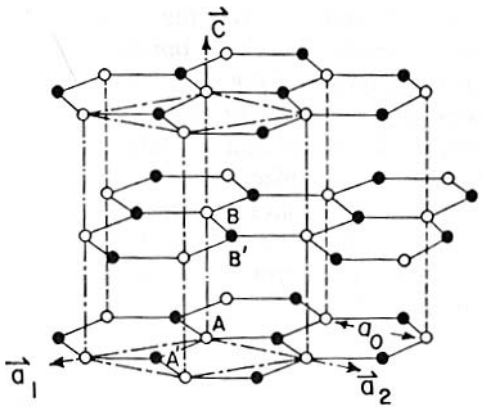

Figure 2.7. Hexagonal crystal structure of graphite [67]

Polarized light microscopy is a technique to study the orientation of doubly refracting, or birefringent materials [68]. It is ideal for studying aligned plate-like or prismatic crystals such as the hexagonal crystal structure of graphene. A standard bright field optical microscope can be transformed to a polarized light microscope with the addition of a polarizing filter and an analyzer, which sandwich the specimen under investigation.

As light passes through the polarizing filter, it is restricted to a single plane of vibration. As this polarized light passes through the material, the uniform light waves diffract resulting in interference. This diffraction causes changes in the wavelength of the light and as it strikes the analyzer, a standard color spectrum pattern is created. By investigating the color pattern, inferences about the nature of the crystal can be made, identifying areas where the graphene orientation changes.

Specifically for carbon foam, polarized light microscopy images such as that in Figure 2.8 are quantified by identifying the regions of magenta, blue, yellow and black, which

reflect changes in the graphene orientation relative to each other. The yellow and blue colors reflect positive and negative 45 degree rotations from the magenta orientation, while the black represents a 90 degree rotation from magenta as shown in Figure 2.9. Furthermore, the planes of graphene tend to conform to the shape of the ligament wall as you traverse the pore boundaries. This indicates that the ligament axis tends to be parallel to the graphene planes as shown in Figure 2.10.

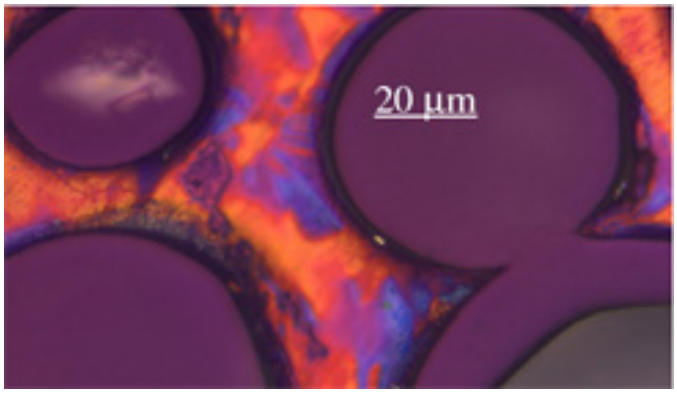

Figure 2.8. Polarized OM image of a carbon foam showing anisotropy

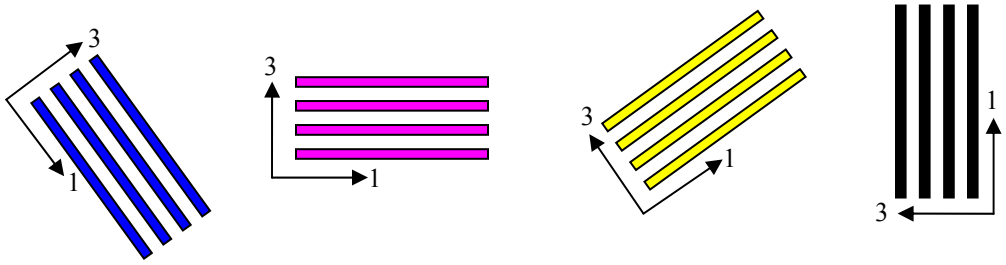

Figure 2.9. Relative orientations in polarized OM on carbon foam

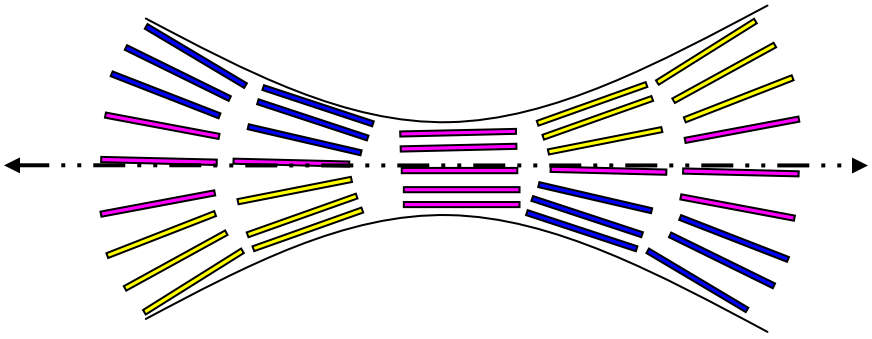

Figure 2.10. Dominate direction for graphene planes with respect to ligament axis

In addition to polarized OM information, additional information regarding the material anisotropy in a ligament is obtained through SEM images of the carbon foams. This allows for additional information regarding the structure of the underlying graphene planes to be identified. In some multi-functional carbon foams doped with additives, a specific zig-zag structure has been identified which resembles the microstructure of carbon fibers as shown in Figure 2.11.

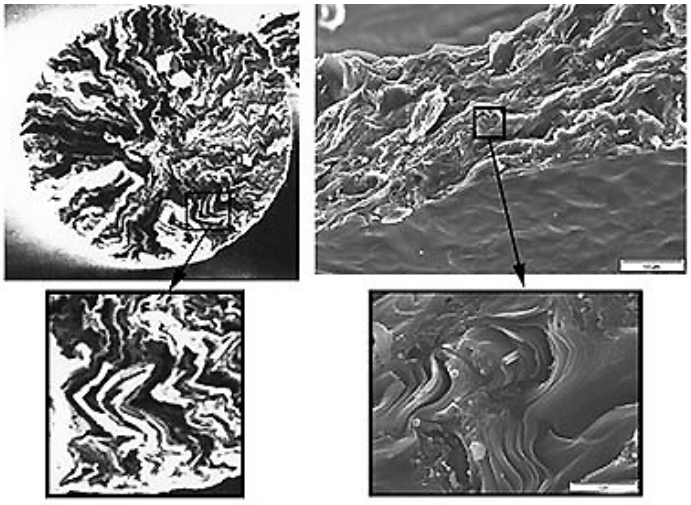

(a) (b)

Figure 2.11. Graphene zig-zag structure in (a) carbon fibers and (b) doped carbon foam [14]

2.2 Overview of Image to FEA Mesh Generation

2.2.1 Extraction of Isosurfaces

Recall that the micro-CT X-ray procedure described in Section 2.1.1 results in a series of reconstructed images, such as that in Figure 2.6, representing every cross section in the imaged sample. These reconstructed images are commonly used to visualize the overall shape and form of the imaged specimen using special rendering techniques, especially in the medical field. These rendering techniques focus on making the final geometric model visually appealing by applying textures, lighting schemes and shading. However, by extending the concepts of graphical visualization and enforcing additional finite element criteria—aspect ratio, angle and shape quality—the reconstructed images can also serve as the basis for a geometric mesh in numerical analyses.

The first step in creating finite element meshes is to segment the reconstructed images to create binary black and white images in a manner similar to thresholding, where pixels below the threshold are turned one color while those above a different color. This is accomplished using a flood filling algorithm, where contiguous regions of pixels are set to a user-specified color if the original pixel has some prescribed property. In this case, it is possible to identify a set of grayscale values for pixels in the pore space and a separate range of values for pixels representing carbon foam. Therefore, pixels representing the pores are set to white and ligament ones to black. From this binary volumetric image, an isosurface which represents the boundary between black and white areas can be generated for investigation in a digital environment.

A well known method for generating an isosurface is the Marching Cubes (MC) algorithm [69]. The algorithm can best be explained by considering a two-dimensional contour plot from which isolines, or lines of constant value, are desired. In this case, a user defined grid is superimposed over the segmented image representing the implicit

function for a circle, where red vertices are outside the circle and blue are inside. The objective of the algorithm is to generate a curve approximating the implicit function, thus a finer grid results in a closer approximation with the inherent pixel grid representing the highest possible resolution. For each cell in the user defined grid, a line is generated which delineates the boundary between values according to predefined weighting functions. This is visually depicted in Figure 2.12 for a single cell and for the entire example grid.

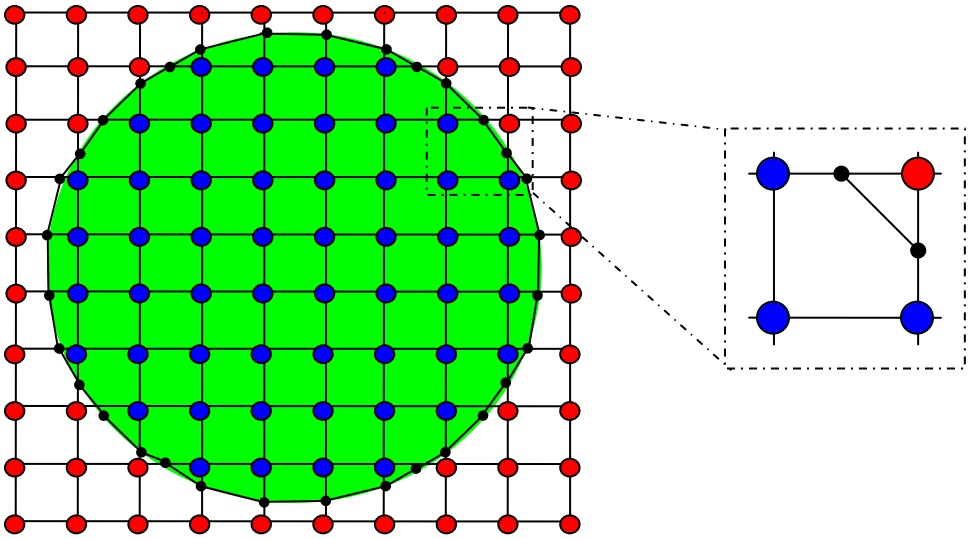

Figure 2.12. Isoline generation to approximate an implicit circle function

The concept of isolines can be extended into three dimensions where isosurfaces are generated for each cell in the grid. Continuing with the previous example, consider a sphere with an overlaid user defined three-dimensional grid. Vertices inside the sphere are blue and those outside red. The application of the Marching Cubes algorithm results in a set of polygons approximating the implicit function of a sphere. There are 14 possible polygons for each cell as determined by the eight corner values as shown in

Figure 2.13. In most cases, higher order polygons—rectangles, hexahedron, et cetera—are divided into triangular elements to unify the surface and ease graphical rendering procedures such as lighting or texture application.

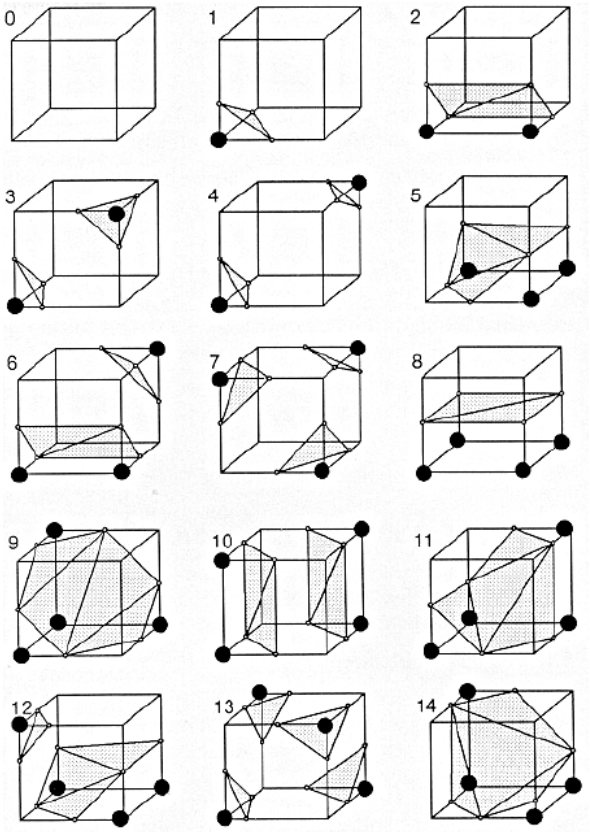

Figure 2.13. Possible isosurface configurations in MC for single cell [69]

2.2.2 Optimization of Extracted Isosurfaces

In practice, Marching Cubes provides a high resolution surface that precisely mimics the original data set but also generates high frequency artifacts such as those shown in Figure 2.14 since the surface conforms to the user defined grid. This surface noise is not

conducive to producing finite elements thus the isosurface must undergo several secondary operations before it can be used to form a solid FE mesh. These operations are designed to improve or modify the surface approximation of the original function, or dataset. In most visualization applications, this does not ensure that the triangular facets meet finite element quality guidelines, although restrictions can be imposed to meet these requirements.

Figure 2.14. Artifacts from MC algorithm [70]

The first category of isosurface modification is surface simplification whereby the surface is modified to include an optimal number of polygons. If the Marching Cubes algorithm is applied using the highest resolution grid, or the inherent image pixel gird, the resulting surface consists of a high number of triangular facets. Some of these are necessary to describe a rapidly changing surface such as near a sharp feature; however, in relatively planar areas, a smaller number of triangles are as effective in describing the surface. Decimation is used to reduce the number of triangles in these relatively flat areas according to a user defined tolerance. Decimation ensures that local topology is maintained while also preserving the approximation of the surface to the original dataset.

Decimation is an edge collapse procedure whereby two vertices are combined reducing the number of edges by one and the number of polygons by two [71]. This is visually depicted in Figure 2.15 for a simple two-dimensional triangular mesh case. The two blue vertices are combined to form a new green vertex, thus eliminating the blue edge and the two blue shaded triangles. The choice of what edge to collapse is determined through an optimization procedure such that the new surface is within a tolerance of the old, maintaining the approximation. A second optimization criterion is used to determine the position of the new vertex. In many cases, the new vertex is placed at the average position of its nearest neighbors creating approximately equal edges to the surrounding vertices.

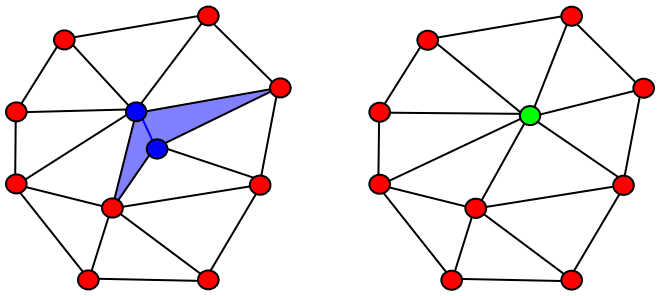

Figure 2.15. Edge collapse procedure used in decimation of triangular meshes

A second category of isosurface modification is smoothing to improve the accuracy of the approximation to the original geometry. Recall that the Marching Cubes algorithm creates a surface which conforms to the user grid resulting in a stair step surface. In order to smooth these high frequency artifacts, a Laplacian smoothing procedure is undertaken where the position of each vertex in the mesh is considered according to its neighbors. The objective of the algorithm is to place each vertex at the average position of the nearest vertices according to an optimization problem. Successive Laplacian

smoothing is not recommended as volume preservation is not enforced and at infinite applied smoothing steps, the surface shrinks to a single point [72].

2.2.3. Reducing Memory Requirements

Although the above procedures are applicable in many cases, each step is memory intensive and when considering large datasets, they often become infeasible. The largeness of a dataset is generally considered a function of the information contained in a single pixel and the size of the image. A common file type used in the X-ray CT reconstruction is 8-bit grayscale images, thus each pixel contains 8-bits of information. Over an image size of 1000 x 1000 pixels this equates to approximately 1 megabytes of information per slice. For a complete dataset of 1000 slices, the total memory required is 1 gigabyte. With the objective of speed and efficiency, most traditional algorithms strive to hold all information in memory, rather than write it out to a hard disk. Most modern day computers can hold only 1-2GB of information in memory at any given time including any memory requirements associated with underlying hardware or software. Therefore, the dataset size is approaching the limits of fast isosurface generation using traditional methods and alternative approaches are being developed.

To circumvent this problem, several new algorithms have been developed which take advantage of parallel processing approach to reduce the memory requirements producing fast and efficient algorithms for isosurface generation. For instance, the extraction of the isosurface and the subsequent decimation can be undertaken in a single algorithm that alternates between the two procedures [73]. In this case there are two fronts, a leading one for the extraction of the high resolution surface and a second one behind which simplification through decimation is undertaken; however, the fronts are separated to ensure that the simplification is undertaken only when complete information about the surface is available. The tandem algorithm produces a fine mesh near the leading front

with an optimal coarse mesh behind as in Figure 2.16. Consequently, it avoids holding the entire high resolution extracted surface in memory improving the overall speed of the algorithm and allowing application to large datasets.

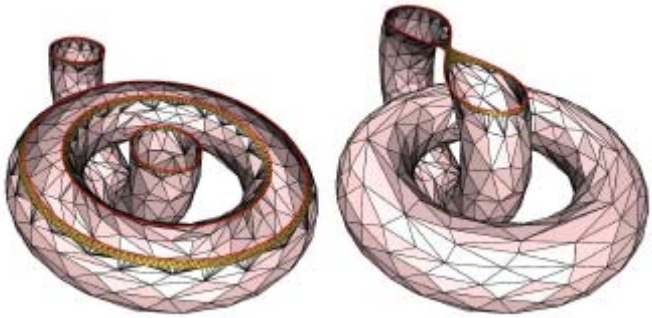

Figure 2.16. Tandem algorithm of isosurface extraction and simplification on link [73]

Another method to increase efficiency and generate isosurfaces for large datasets is to use a dual contouring extraction method [74]. This method has the benefit of generating a smoother initial extraction surface composed of higher quality elements, thus reducing the need for surface simplification and smoothing. In addition, this method can applied with octree grids eliminating the need for uniform grid sizes. An octree is a type of adaptive grid which becomes fine in areas of rapidly changing topology, while relatively flat areas are extracted with a coarse grid. This technique significantly reduces the number of triangles extracted initially, and combined with the smoother surface property is memory efficient when working with large datasets.

2.2.4. Isosurface Extension to Volumetric Solid Meshes

The procedures detailed above focus on isosurface meshes consisting of triangular elements delineating the boundary of an enclosed volume. In the case of solid

mechanics, the isosurface mesh is transformed by space filling the enclosed volume with tetrahedral elements creating a solid finite element mesh for analysis. These volumetric meshing algorithms are fundamentally harder than their two-dimensional counterparts especially in the areas of high quality element optimization and precise matching of the existing boundary shape.

Two main strategies for producing solid meshes of enclosed volumes are advancing fronts and Delaunay triangulations [75]. Advancing fronts start from the boundary of the volume and generate layers of tetrahedron by progressively adding vertices as it moves into the volume. Placement of the new vertices is determined by a local objective to ensure quality element generation, with periodic optimization to further improve quality. Delaunay triangulation schemes attempt to generalize two-dimensional Delaunay triangulation into three-dimensional space. This technique attempts to place vertices at optimal distances from their nearest neighbors thus generating high quality isotropic tetrahedron. Delaunay triangulation also results in an optimal number of elements needed to describe the enclosed volume. Both strategies can use an isosurface triangular mesh as input for generating a three-dimensional solid mesh, although the quality of the isosurface does not ensure the final tetrahedral mesh quality.

2.3. Fundamentals of Coupled Field Boundary Value Problems

The externally applied load conditions of interest are pure mechanical and thermal boundary value problems (BVP), sequentially coupled thermo-mechanical BVPs and fully coupled thermal-electrical analysis problems in order to investigate the material response of the multi-functional carbon foam system. The mechanical boundary conditions are limited to compressive modes due to the brittle nature of the carbon foam material system. Furthermore, the thermal and electric boundary conditions under

investigation include temperatures sources or sinks along with applied currents and voltages.

For the pure mechanical case, the boundary value problem is developed from an arbitrary body shown in Figure 2.17. In this case, the volume (V) is bounded by the surface (Ω) which may be divided into multiple regions (Ω_1, Ω_2, et cetera) based on the applied boundary condition.

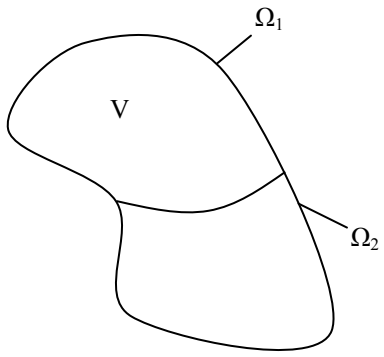

Figure 2.17. Arbitrary volume used in balance of equilibrium statement

Using the linearized theory of elasticity approach with a Lagrangian viewpoint, the statement of static equilibrium is represented as Equation 1, where t is a surface traction and f represents any considered body forces for the volume [76]. All equations in this section are presented in both vector form and in summation notation, where applicable, for the orthogonal Cartesian coordinate system.

$$\int_{\Omega} \vec{t}\, dS + \int_{V} \vec{f} dV = 0 \qquad \int_{\Omega} t_i dS + \int_{V} f_i dV = 0 \qquad [1]$$

Substituting the definition of Cauchy stress at a point as shown in Equation 2 and using Gauss's theorem presented in Equation 3, the equilibrium statement has the form shown in Equation 4.

$$\vec{t} = \hat{n} \cdot \vec{\vec{\sigma}} \qquad t_i = \hat{n}_j \cdot \sigma_{ji} \qquad [2]$$

$$\int_\Omega \hat{n} \cdot (\ ) dS = \int_V \left(\frac{\partial}{\partial \vec{x}} \right) \cdot (\ ) dV \qquad \int_{\Omega S} \hat{n}_i \cdot (\ ) dS = \int_V \left(\frac{\partial}{\partial x_i} \right) \cdot (\ ) dV \qquad [3]$$

$$\int_V \left[\nabla \cdot \vec{\vec{\sigma}} + \vec{f} \right] dV \qquad \int_V \left(\frac{\partial \sigma_{ji}}{\partial x_j} + f_i \right) dV \qquad [4]$$

This equation is valid at any point within the body thus resulting in the differential stress equilibrium equations as shown in Equation 5.

$$\nabla \cdot \vec{\vec{\sigma}} + \vec{f} = 0 \qquad \frac{\partial \sigma_{ji}}{\partial x_j} + f_i = 0 \qquad [5]$$

The stress and strain tensors are related using a constitutive material response equation. In this case, the constitutive behavior is defined according to a generalized Hooke's law containing 21 independent stiffness components representing a fully anisotropic material as shown in Equation 6. If material symmetries exist, the stiffness matrix C_{ijkl} reduces such as the case of isotropic materials where there are only two independent constants.

$$\vec{\vec{\sigma}} = \vec{\vec{C}} : \vec{\vec{\varepsilon}} \qquad \sigma_{ij} = C_{ijkl}\varepsilon_{kl} \qquad [6]$$

In addition, kinematic equations are used to relate the strain tensor to the displacement field. The assumptions of small displacements results in an infinitesimal strain relationship shown in Equation 7.

$$\vec{\vec{\varepsilon}} = \frac{1}{2}\left[\nabla\vec{u} + (\nabla\vec{u})^T\right] \qquad \varepsilon_{ij} = \frac{1}{2}\left(u_{i,j} + u_{j,i}\right) \qquad [7]$$

Substituting Equation 6 and 7 into the equilibrium equation, results in the final governing differential equations for a pure mechanical boundary value problem. Equation 8 is the three-dimensional Navier equation for an anisotropic body in static equilibrium [77].

$$\nabla \cdot \left[\vec{\vec{C}} : (\nabla\vec{u})\right] + \vec{f} = 0 \qquad C_{ijkl}\frac{\partial}{\partial x_j}\left(\frac{\partial u_k}{\partial x_l}\right) + f_i = 0 \qquad [8]$$

In addition to pure mechanical fields, additional material response is determined under a pure thermal field. In this case, a conservation of energy statement is developed for the closed system shown in Figure 2.18 [78]. In this case, there are two sources of energy—heat transferred through the boundary (Q) and heat generated within the body (Q_v).

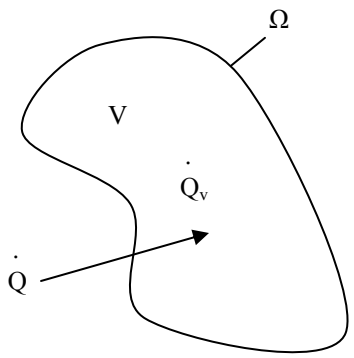

Figure 2.18. Arbitrary volume used in balance of energy statement

Conservation of energy in this case results in Equation 9, where U is the internal energy for the closed system.

$$\frac{dU}{dt} = \dot{Q} + \dot{Q}_v \qquad [9]$$

Through assumptions of constant mass and an incompressible solid, this reduces to Equation 10 where c is the specific heat and ρ is the density.

$$\rho V c \frac{dT}{dt} = \dot{Q} + \dot{Q}_v \qquad [10]$$

The heat flow through the boundary is a function of the heat flux (q) and area as shown in Equation 11. For the case of heat transfer via conduction only, Fourier's law is used to relate the heat flux to the temperature gradient in the material as in Equation 12.

$$\dot{Q} = \vec{q}A \qquad [11]$$

$$\vec{q} = -\vec{\vec{k}}\vec{\nabla}T \qquad q_i = -k_{ij}\left(\frac{\partial T}{\partial x_j}\right) \qquad [12]$$

For the case of pure conduction, the final governing equation for the temperature distribution inside a solid body is shown in Equation 13 [79]. This represents the transient case with internal volumetric heat generation.

$$\rho Vc\frac{dT}{dt} = \vec{\nabla}\cdot\left(\vec{\vec{k}}\vec{\nabla}T\right) + \dot{Q}_v \qquad \rho Vc\frac{dT}{dt} = \frac{\partial}{\partial x_i}\left(k_{ij}\frac{\partial T}{\partial x_j}\right) + \dot{Q}_v \qquad [13]$$

It is noted that for carbon foams, changes in temperature result in mechanical strain due to coefficient of thermal expansion (CTE) coupling; however, applied mechanical loads result in negligible temperature rises. Therefore, the thermo-mechanical coupled field boundary value problem was decoupled into two individual problems. Initially, the thermal boundary value problem is analyzed and the resultant temperature field obtained. These temperatures are then used as input into the subsequent mechanical boundary value problem analysis along with any mechanical loads of interest, hence the term sequential coupling. This approach requires the modification of the governing

equations above to consider any thermally induced strain contribution. The constitutive relationship in Equation 6 is modified to include thermally induced strains as shown in Equation 14. The thermal strains are represented as a function of the linear coefficients of expansion (α) as seen in Equation 15, where ΔT is the change in temperature from the initial condition.

$$\vec{\vec{\sigma}} = \vec{\vec{C}} : \left(\vec{\vec{\varepsilon}}^{mech} + \vec{\vec{\varepsilon}}^{thrm} \right) \qquad \sigma_{ij} = C_{ijkl} \left(\varepsilon_{kl}^{mech} + \varepsilon_{kl}^{thrm} \right) \qquad [14]$$

$$\vec{\vec{\varepsilon}}^{thrm} = \vec{\vec{\alpha}} \Delta T \qquad \varepsilon_{kl}^{thrm} = \alpha_{kl} \Delta T \qquad [15]$$

Substituting these relationships into the stress equilibrium equations as before, results in the governing equations for a thermo-mechanical boundary value problem in Equation 16. In this case the temperature field directly influences the stress and strain fields along with any mechanically induced effects.

$$\nabla \cdot \left[\vec{\vec{C}} : \left(\nabla \vec{u} + \vec{\vec{\alpha}} \Delta T \right) \right] + \vec{f} = 0 \qquad C_{ijkl} \frac{\partial}{\partial x_j} \left(\frac{\partial u_k}{\partial x_l} + \alpha_{kl} \Delta T \right) + f_i = 0 \qquad [16]$$

To complete the investigation of material response, the final coupled field applied to the carbon foam model is a thermal-electrical loading case. The formulation begins with Maxwell's equation for conservation of charge which governs the electric energy balance for an arbitrary body as represented in Equation 17 where J is the electrical current density (current per unit area) on the surface and r_c is the internal current source per unit volume [80].

$$\int_{\Omega}\left(\vec{J}\cdot\hat{n}\right)dS=\int_{V}r_c dV \qquad \int_{\Omega}J_i n_i dS=\int_{V}r_c dV \qquad [17]$$

Using Gauss's theorem in Equation 3, the surface integral is transformed into a volumetric form presented in Equation 18.

$$\int_{V}\left[\left(\frac{\partial}{\partial\vec{x}}\right)\cdot\vec{J}-r_c\right]dV \qquad \int_{V}\left(\frac{\partial J_i}{\partial x_i}-r_c\right)dV \qquad [18]$$

This equation is valid at any point within the body thus resulting in the pointwise differential form in Equation 19.

$$\left(\frac{\partial}{\partial\vec{x}}\right)\cdot\vec{J}-r_c=0 \qquad \frac{\partial J_i}{\partial x_i}-r_c=0 \qquad [19]$$

The electric current is described by Ohm's law in Equation 20 where E is the electric field and σ^e is the electric conductivity. In addition, the electric field can be related through an electric potential function as in Equation 21.

$$\vec{J}=\vec{\vec{\sigma}}^{e}\cdot\vec{E} \qquad J_i=\sigma_{ij}^{e}E_j \qquad [20]$$

$$\vec{E}=-\frac{\partial\varphi}{\partial\vec{x}} \qquad E_i=-\frac{\partial\varphi}{\partial x_i} \qquad [21]$$

Therefore, the final form of the electrical governing equation is shown in Equation 22. In this case, the influence of the thermal part of the coupled problem is not readily apparent; however, the electrical conductivity term is generally a function of temperature.

$$\left(\frac{\partial}{\partial \vec{x}}\right)\cdot\left(\vec{\vec{\sigma}}^{e}\cdot\frac{-\partial\varphi}{\partial \vec{x}}\right)-r_c=0 \qquad -\frac{\partial}{\partial x_i}\left(\sigma_{ij}^{e}\frac{\partial\varphi}{\partial x_j}\right)-r_c=0 \qquad [22]$$

Conversely, the influence of the electric problem on the coupled problem is more obvious. The internal volumetric heat generation term from Equation 13 is a function of the electric current flowing through the body. This energy, termed Joule heating, is defined by Equation 23, where η_v is an energy conversion factor for the efficiency of the energy transformation. If all the electric energy is converted to heat, this factor is unity [81].

$$\dot{Q}_v=\eta_v\left[\vec{E}\cdot\left(\vec{\vec{\sigma}}^{e}\cdot\vec{E}\right)\right] \qquad \dot{Q}_v=\eta_v\left(E_i\sigma_{ij}^{e}E_j\right) \qquad [23]$$

3. MULTI-SCALE ANALYSIS DEVELOPMENT FOR MULTI-FUNCTIONAL CARBON FOAMS

The multi-scale approach used herein is enabled through detailed information about the carbon foam morphology from high resolution micro-CT X-ray tomography. This detailed three-dimensional information is then manipulated using a unique approach to data visualization to achieve a high quality finite element mesh suitable for numerical analysis. After incorporating ligament anisotropy and coatings or infiltrations for multi-functionality, coupled field boundary conditions are introduced to identify material response in application design environments.

3.1. Finite Element Mesh Techniques

The basis for microstructure-based models presented herein is information generated from micro-CT X-ray tomography performed on a small 2.25 cm^3 specimen of 30 ppi carbon foam using the SkyScan 1172 system at the Beckman Institute located at the University of Illinois at Urbana-Champaign. The X-ray data is reconstructed to images of 2376 x 3484 pixels by 1983 slices at a resolution of 5.66 μm per pixel. This reconstructed image dataset is cropped to 1000 x 1000 pixels by 1017 slices to remove localized misalignment.

The reconstructed images are 8-bit grayscale indicating that each pixel in the image contains 8 bits of information resulting in a total image size of 1 megabyte. When considering the full dataset of 1017 images, memory requirements are approximately 1-2 gigabytes and modern computers are only capable of holding 2 gigabytes of information in memory at a time. Therefore, the image to FEA mesh technique developed for the carbon foam dataset incorporates a tandem algorithm and other techniques described in Section 2.2 to minimize memory requirements. Development of the isosurface

generation technique described below is a collaborative effort with visualization researchers interested in developing new algorithms applicable to large datasets [82].

3.1.1. Image to FEA Mesh Generation for the Carbon Foam

Initially, a few slices of reconstructed image data are read into the algorithm and segmented with a simple threshold procedure resulting in binary (black and white) images. In order to counteract the stair stepping artifacts of the surface extraction, a Gaussian blur is applied in all dimensions to the binary images to blur the boundary lines and produce a smoother final surface. Next, a Marching Tetrahedrals extraction procedure is utilized to generate the isosurface. This algorithm is similar to Marching Cubes, but with the grid composed of tetrahedrals not rectangular prisms, resulting in a finer grid capable of capturing fine details in the carbon foam microstructure. As the extraction front in the tandem algorithm advances through the dataset, additional image slices are read and processed to produce the triangulated isosurface.

In parallel with the extraction procedure, a second front is identified behind which a surface simplification algorithm is applied in the form of edge collapse. Two metrics are used during this simplification for the placement of the new vertices—geometric approximation and element quality. In order to ensure that the resulting isosurface accurately describes the original dataset, the first metric places the new vertices with a tolerance of the original plane of intersection of the old triangles. This metric also enforces a maximum number of triangles used in the approximation of the surface. The second metric is focused on producing high quality elements as determined by the maximum and minimum angles. This optimization places the new vertex at the average position of its nearest neighbors producing approximately equal edge lengths. At the conclusion of the tandem algorithm, the final section of the extracted surface is still

composed of a fine mesh since the extraction and simplification fronts were separated. Thus, a final surface simplification pass is undertaken for the entire surface.

The two simplification criteria used in the algorithm are at odds with each other thus the two metrics—geometric approximation and element quality—must be weighted in the tandem algorithm. A higher weight is placed on the high quality element objective, while a final surface smoothing pass is undertaken on the extracted and simplified surface to further improve the geometric approximation. The surface smoothing algorithm is based on the approach by Taubin to fair surface design [83]. This algorithm is an improvement over the Laplacian schemes and avoids shrinking the volume with successive smoothing passes. The resulting triangulated isosurface is then expressed in terms of vertex position and element connectivity for further pre-processing steps prior to finite element analysis.

In order to transform this high quality triangular mesh into a solid mesh of the carbon foam microstructure, PATRAN, a finite element analysis pre-processor, is used. After importing the triangular mesh into the software package as an ABAQUS input deck, a built in function is used to generate a solid tetrahedral mesh. Since the original surface is defined by linear triangular elements, the solid mesh is also linear, or four node tetrahedrals, by default. However, if the original surface mesh is modified to include midside nodes, a higher order mesh of quadratic elements can be generated by the built in function.

The built in function is based on an advancing front algorithm as described in Section 2.2.4 with the requirement that the original triangulated surface completely enclose a single volume. Each triangle is considered a face of a newly generated tetrahedral element. From this new layer of tetrahedral elements, the free surface is identified as a new set of triangular elements and the procedure is repeated until the entire enclosed volume is filled. A gradient option is invoked in the function to coarsen the mesh size as

the advancing front algorithm continues deeper into the enclosed volume, while maintaining a fine mesh at the exterior to capture any high frequency surface features for further study. The final result is a quality three-dimensional solid mesh composed of linear tetrahedral element and forms the basis of the developed finite element model. The complete developed image to FEA mesh algorithm is shown in Figure 3.1.

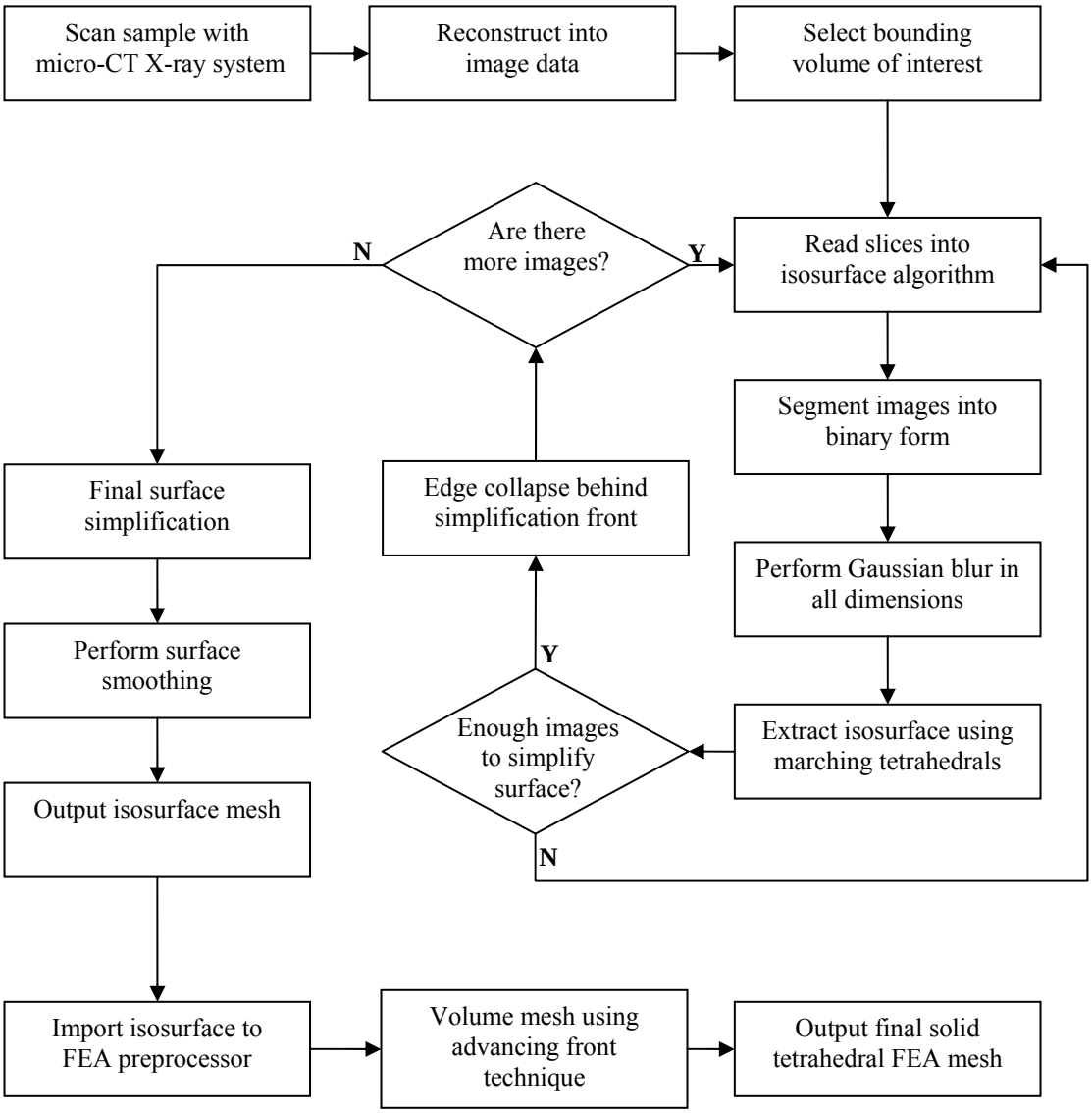

Figure 3.1. Developed micro-CT X-ray image to FEA mesh algorithm

3.1.2. Introducing Coating and Infiltration into the FEA Mesh

Thin coatings (< 5 μm) such as those shown in Figure 3.2 cannot be captured using micro-CT X-ray methods for incorporation into the computational model since their dimension falls below the minimum feature size detectable with a 5 μm resolution size. In addition, metallic coatings shield the X-rays preventing imaging of thicker coatings or full infiltrations. Therefore, in order to incorporate coating and infiltration for multi-functional studies, additional elements must be independently introduced into the finite element mesh.

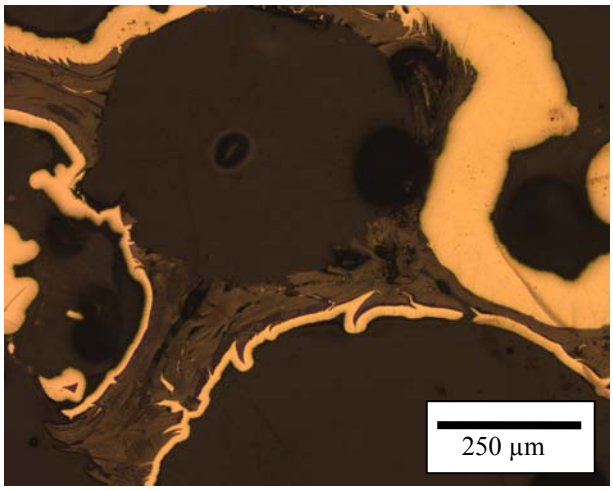

Figure 3.2. Optical microscopy image of a carbon foam with metallic coating

This procedure begins with the triangulated isosurface mesh generated from the micro-CT X-ray images. Initially, the normal vectors of these two-dimensional triangular elements are reversed to point outward from the foam ligament interiors into the pore spaces. Next, a solid wedge element is formed by extruding the triangular facet in the normal direction; however, since each triangle is surrounded by adjacent facets, the extruding direction for a single facet is modified to represent an average of the

neighboring facet normal vectors. This maintains continuity across the surface resulting in an idealized layer of coating elements on the ligament substrate that is uniform in thickness and perfectly bonded to the foam. Since the triangular meshes are composed of linear elements, the new coating is represented with linear, six node wedge elements. Figure 3.3 illustrates the sweep procedure where the original triangular elements are shown in blue and the new coating elements in red. This procedure can be repeated to generate more layers, either for a thicker coating or for a composite coating with two or more materials.

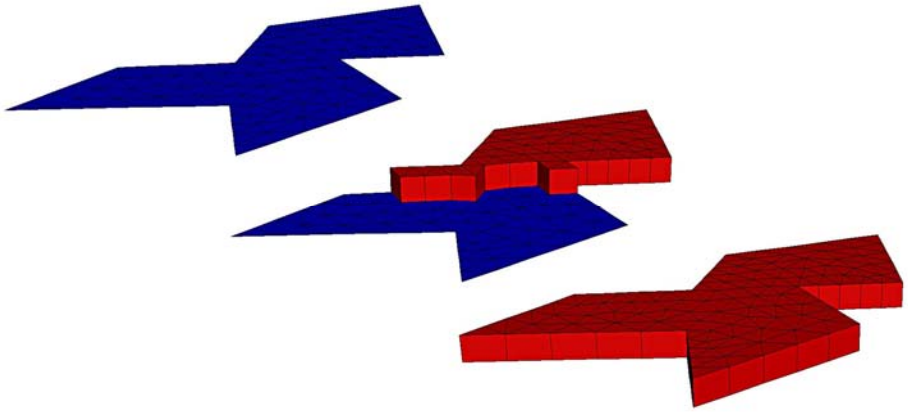

Figure 3.3. Sweeping an idealized coating layer from the triangulated surface mesh

A method for creating complete infiltration of the carbon foam morphology is also developed based on the advancing front algorithm used to mesh the carbon foam structure with tetrahedral elements. Initially, a bounding box is created to surround the carbon foam geometry and meshed with linear triangular elements. The two surfaces, bounding box and triangulated carbon foam surface, define a closed volume representing the pore space in the foam. By applying the advancing front tetrahedral meshing algorithm to the space between this bounding box surface and the carbon foam isosurface, the cavity space is filled with linear tetrahedral elements.

3.2. Multi-scale Models

The final finite element mesh accurately describes the overall morphology including the precise cross section of individual ligaments and any artifacts in the foam below the simplification threshold as discussed in Section 2.2.2. In addition, the approach to capturing the carbon foam microstructure from micro-CT X-ray images also enables the study of the carbon foam material system at multiple scales using a single scan. A volume of interest (VOI) such as a single ligament with its end nodes can be studied for the effects of ligament anisotropy material orientation, or for the effect of cracks on the overall material response. Larger scales such as a multiple pore VOI are used to study transport phenomenon where the connectivity of the ligaments plays an important role. By creating a general algorithm, many specific VOI finite element models, as shown in Figure 3.4, can be generated to meet specific research objectives. In this case, three main length scales are identified as a single ligament, a single enclosed cavity and several interconnected cavities.

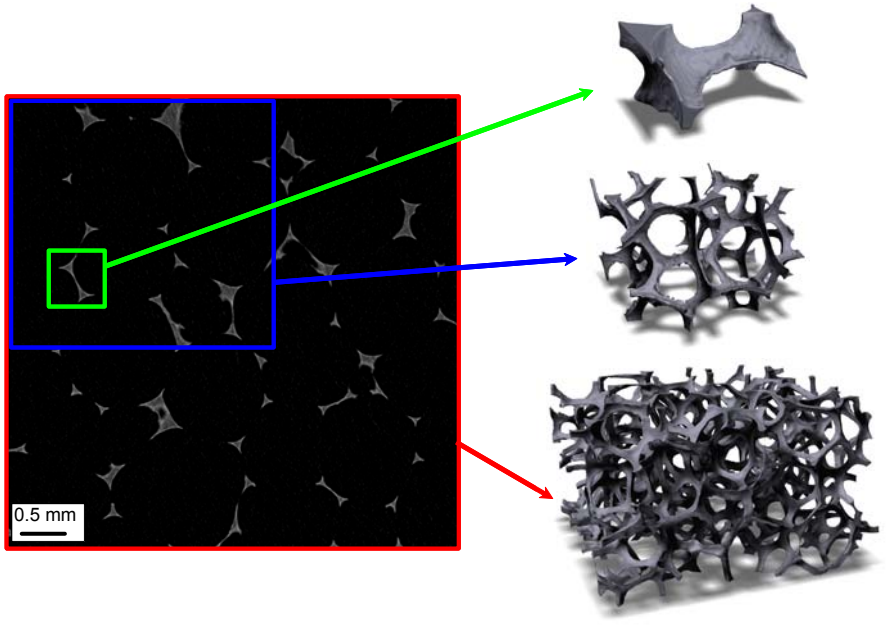

Figure 3.4. Various VOI models from single micro-CT X-ray scan

3.2.1. Single Ligament VOI

Recall that the carbon foam morphology is composed of individual ligaments connected at the nodes forming a truss like structure; therefore, a single ligament with its two end nodes is identified as the smallest volume of interest in this study. At this scale various features of the ligament are investigated for their impact on material response. For instance, recall that carbon foam ligaments have a triangular shaped cross section which tapers and bends along its length. In addition, the surface of the ligament is not smooth and has various ridges and bumps as shown in Figure 3.5.

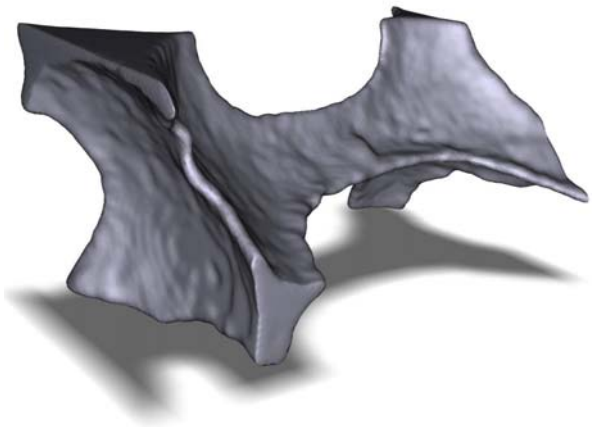

Figure 3.5. Single ligament VOI model from carbon foam image data

This ligament is identified by a bounding box in the 30 ppi image data set approximately 0.49 x 0.40 x 0.88 mm in dimension, or 0.173 mm^3. The ligament is approximately 0.5 mm long as measured between the centers of gravity of each nodal region. In addition, the ligament cross sectional area decreases over 80% as it tapers from the nodal regions to the center of the ligament span as shown in Figure 3.6.

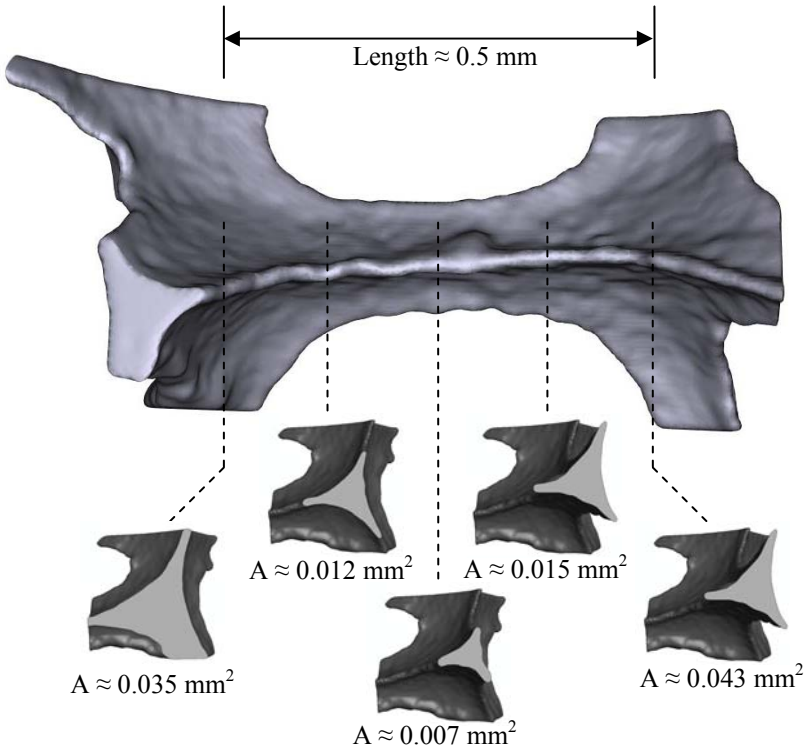

Figure 3.6. Single ligament VOI geometric measurements

The original triangulated isosurface for the single ligament VOI model is composed of 99,996 facets connecting 50,000 nodes, which is sufficient to capture the detail of the irregular surface. This represents a total surface area of 0.946 mm^2. The enclosed volume is 0.0188 mm^3 where the surface area to volume ratio is approximately 50.

The triangulated surface is translated to a solid mesh of the enclosed volume using 498,383 linear tetrahedral elements and 109,586 nodes. A uniform coating is swept from the triangulated surface to a thickness of 5 μm using 99,996 linear wedge elements connecting 100,000 nodes. The resulting coating comprises a volume of 0.0049 mm^3 representing a volume fraction of 0.260. The coating increases the exposed surface area 6.5% to 1.008 mm^2.

3.2.2. Single Enclosed Cavity VOI

The next geometric scale investigated is several ligaments connected to form a single enclosed cavity region as shown in Figure 3.7. This structure is used to identify ligament to ligament interactions and load transfer through the carbon foam nodes. In addition, infiltrations of the carbon foam morphology are possible at this geometric scale. Finally, investigation of processing defects such as small holes, filament bridges or surface imperfections is possible at this scale.

Figure 3.7. Single enclosed cavity VOI model from carbon foam image data

The enclosed cavity is identified by a 2.02 x 2.01 x 1.83 mm bounding box in the image dataset surrounding 7.45 mm^3. The single enclosed cavity is composed of 74 individual ligaments, where the ligament lengths follow a normal distribution with a mean value of 0.47 mm and standard deviation of 0.155 mm. The cross sectional areas as measured at

the ligament centers also follow a normal distribution with mean and standard deviation of 0.0078 mm^2 and 0.0029 mm^2 respectively.

The original triangulated isosurface for the single enclosed cavity VOI model is composed of 398,158 facets connecting 199,051 nodes. The total surface area is 13.77 mm^2, with an enclosed volume of 0.265 mm^3, resulting in a high surface area to volume ratio of 52. Using the relative density ρ^*/ρ_s, the overall porosity is 96.3% according to Equation 24 [30].

$$p = 1 - \frac{\rho^*}{\rho_s} \qquad [24]$$

The triangulated surface is used to generate a solid mesh of the enclosed volume using 1,667,690 linear tetrahedral elements and 182,646 nodes, with an average of 22,536 elements per ligament. A uniform coating is swept from the triangulated surface using two equal layers for a total thickness of 0.10 μm. Each coating layer is composed of 398,158 linear wedge elements connecting 398,102 nodes, for a total volume of 0.134 mm^3. For a single 5 μm thick layer of coating, the coating volume fraction is 0.25 and for the total coating thickness of 10 μm, the volume fraction increases to 0.50 relative to the solid material. The two layers of coating increase the exposed surface area 5.6% to 14.54 mm^2.

3.2.3. Several Interconnected Cavities VOI

At present, the largest geometric scale investigated is four interconnected enclosed cavities as shown in Figure 3.8. At this VOI scale, the model is likely to estimate the

bulk response of the carbon foam allowing for prediction of effective properties. In addition, the pore to pore interactions are investigated for transport phenomenon such as load transfer or heat dissipation.

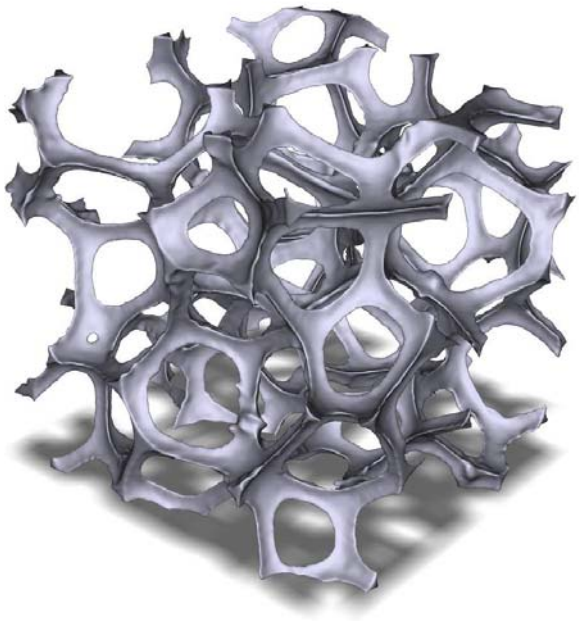

Figure 3.8. Several interconnected cavities VOI model from carbon foam image data

The four interconnected cavities are identified by a bounding box in the 30 ppi image dataset approximately 3.20 x 3.00 x 2.83 mm in dimension for a total bounding volume of 27.2 mm^3.

The several interconnected enclosed cavities VOI triangulated isosurface is created using 197,649 nodes connected by 395,558 linear tetrahedral elements. This accounts for a total surface area of 46.01 mm^2 and a total enclosed volume of 0.899 mm^3 for a surface area to volume ratio of 51. The relative density results in an overall porosity of 95.0% according to Equation 24.

Transformation of the isosurface to a FEA mesh, results in volumetric solid mesh composed of 1,191,294 linear tetrahedral elements connecting 104,323 nodes. In this case, the uniform coating is swept from the isosurface in two 5 μm layers for a total coating thickness of 10 μm. Each layer contains 395,558 elements and 395,298 nodes, resulting in the full coating thickness including 791,116 elements and 790,596 nodes. The total coating volume is 0.464 mm^3 resulting in a volume fraction of 0.51 with respect to the solid material. In addition, for the full coating thickness the exposed surface area increases 9.3% to 50.27 mm^2.

3.3. Effective Anisotropic Properties at a Material Point

Recall from Section 2.1.2 that observation with both polarized OM and SEM, reveals a zig-zag structure in multi-functional carbon foams doped with additives. This zig-zag pattern consists of orientation changes of the base material, graphene or graphite, and accounts for its improved mechanical strength characteristics. The graphene is formed during heat treatments when the carbon molecules develop more order as shown in Figure 1.3. In order to account for ligament anisotropy, a material unit cell is developed to evaluate the effective properties associated with this specific zig-zag structure.

The unit cell is divided into a double-cross pattern as seen in Figure 3.9 with each color representing a change in graphene orientation as shown previously in Figure 2.9. Table 3.1 presents the graphene properties used in material coordinates. The graphene orientation in the magenta region is assigned such that the material 1 direction aligns with the global 3^m and material 2 with global 1^m. The graphene orientations in the yellow and blue regions are 45° rotations of this magenta orientation about the global 3^m axis thus resulting in the required zig-zag structure. In addition, this material unit cell also creates a dominant direction for strength and conductivity since the graphene material 1 direction in each region is aligned with the global 3^m axis. This is useful in

recreating the graphene orientation and alignment seen under optical polarized light microscopy and depicted in Figure 2.10.

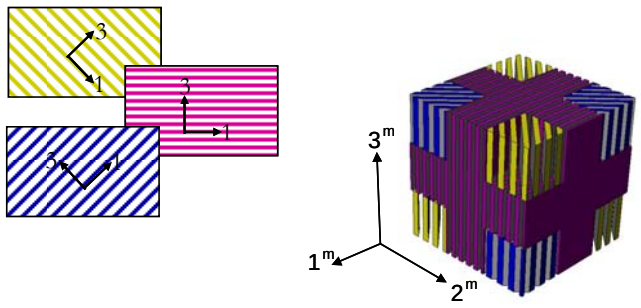

(a) (b)

Figure 3.9. Ligament material anisotropy utilizing (a) three graphene orientations and (b) a zig-zag material unit cell

Table 3.1. Graphene properties [67]

Elastic Stiffness	C_{11}	1060	***GPa***
	C_{33}	36.5	
	C_{44}	4.4	
Density		2.26	***g/cm3***
Specific Heat		0.17	***cal/(g-K)***
Thermal Conductivity	$k_{11}=k_{22}$	30	***W/(cm-K)***
	k_{33}	0.06	
Coefficent of Thermal Expansion	$\alpha_{11}=\alpha_{22}$	-1.00E-06	***1/K***
	α_{33}	2.90E-05	
Electric Conductivity	$\sigma_{11}=\sigma_{22}$	2000	***ohm-cm***
	σ_{33}	1	

After determining the material unit cell composition, a small finite element model is developed to determine effective elastic, thermal and electrical properties. The overall material unit cell geometry is a cube measuring 0.3 mm on each side. This is divided into the double-cross pattern using partitions thus ensuring that individual elements fall within a single graphene orientation—magenta, yellow or blue. Each sub-volume is

meshed in a uniform configuration for a total of 204,320 quadratic tetrahedral elements connecting 44,821 nodes.

To identify the effective elastic properties, finite element analysis is used to obtain stress and strain states for six different loading conditions (three normal and three shear) with symmetry conditions on the exterior boundaries as presented in Table 3.2.

Table 3.2. Boundary conditions used to obtain effective elastic properties

Case 1	+X Face u1=0.003 mm	**Case 2**	+X Face u1=0	**Case 3**	+X Face u1=0
Normal	-X Face u1=0	**Normal**	-X Face u1=0	**Normal**	-X Face u1=0
	+Y Face u2=0		+Y Face u2=0.003 mm		+Y Face u2=0
	-Y Face u2=0		-Y Face u2=0		-Y Face u2=0
	+Z Face u3=0		+Z Face u3=0		+Z Face u3=0.003 mm
	-Z Face u3=0		-Z Face u3=0		-Z Face u3=0
Case 4	+X Face u2=0.003 mm	**Case 5**	+X Face u3=0.003 mm	**Case 6**	+X Face u1=0
Shear	-X Face u2=0	**Shear**	-X Face u3=0	**Shear**	-X Face u1=0
	+Y Face u1=0		+Y Face u2=0		+Y Face u3=0.003 mm
	-Y Face u1=0		-Y Face u2=0		-Y Face u3=0
	+Z Face u3=0		+Z Face u1=0		+Z Face u2=0
	-Z Face u3=0		-Z Face u1=0		-Z Face u2=0

In order to determine the effective properties, each loading case is reduced to a volume averaged stress and strain value according to Equations 25 and 26, where V^{int} is the integration volume.

$$\overline{\varepsilon_{ij}} = \frac{\sum \varepsilon_{ij} V^{\text{int}}}{\sum V^{\text{int}}} \qquad [25]$$

$$\overline{\sigma_{ij}} = \frac{\sum \sigma_{ij} V^{\text{int}}}{\sum V^{\text{int}}} \qquad [26]$$

With the assumptions of linear elastic and small deformations, the constitutive equation becomes $\sigma_{ij}=C_{ijkl}\varepsilon_{kl}$ where C_{ijkl} is a 4^{th} order tensor of 81 constants [77]. With the assumption of symmetric stress ($\sigma_{ij}=\sigma_{ji}$) it follows that $C_{ijkl}=C_{jikl}$ thereby reducing the independent stiffness components to 54. Similarly the assumption of symmetric strain ($\varepsilon_{kl}=\varepsilon_{lk}$) implies $C_{ijkl}=C_{ijlk}$ and the independent components are further reduced to 36, which is referred to as generalized Hooke's law. Further reduction of the independent constants to 21, occurs when the stress strain relationship is developed from a strain energy density function resulting in the relationship of $C_{ijkl}=C_{klij}$. Although further reduction of the number of constants is possible through assumptions regarding the material symmetry, the approach to effective elastic properties presented here starts with the material stiffness tensor for infinitesimal deformation of a linear elastic anisotropic material as shown in Equation 27. If material symmetries do exist in the zig-zag material cell, the resulting effective C_{ij} matrix as calculated using the effective stress and strain tensors will display further simplification. Since the problem is over constrained (36 equations and 21 unknowns) a least squares solution technique is employed to the linear system Ax=b such that the solution (x) minimizes ||Ax-b||.

$$\begin{bmatrix}\sigma_{11}\\ \sigma_{22}\\ \sigma_{33}\\ \tau_{23}\\ \tau_{13}\\ \tau_{12}\end{bmatrix}=\begin{bmatrix}c_{11} & c_{12} & c_{13} & c_{14} & c_{15} & c_{16}\\ & c_{22} & c_{23} & c_{24} & c_{25} & c_{26}\\ & & c_{33} & c_{34} & c_{35} & c_{36}\\ & & & c_{44} & c_{45} & c_{46}\\ & sym & & & c_{55} & c_{56}\\ & & & & & c_{66}\end{bmatrix}\begin{bmatrix}\varepsilon_{11}\\ \varepsilon_{22}\\ \varepsilon_{33}\\ \gamma_{23}\\ \gamma_{13}\\ \gamma_{12}\end{bmatrix} \qquad [27]$$

Similar procedures are used to obtain effective thermal conductivity (k_{ij}), effective CTE (α_{ij}) and effective electrical conductivity (σ_{ij}) values using the boundary conditions in Table 3.3. The effective properties are calculated using Equations 28-30 and the respective volume averaged tensors for heat flux (q), electric current density (J) and

electric potential gradient (E). The final mechanical, thermal and electrical effective material properties are reported in Table 3.4 for the zig-zag material unit cell, representing ligament anisotropy at a material point in the carbon foam.

Table 3.3. Boundary conditions to obtain effective thermal and electrical properties

Thermal Conductivity	**Case 1**	+X Face T=600 °K -X Face T=100 °K +Y Face insulated -Y Face insulated +Z Face insulated -Z Face insulated	**Case 2**	+X Face insulated -X Face insulated +Y Face T=600 °K -Y Face T=100 °K +Z Face insulated -Z Face insulated	**Case 3**	+X Face insulated -X Face insulated +Y Face insulated -Y Face insulated +Z Face T=600 °K -Z Face T=100 °K
Electrical Conductivity	**Case 1**	+X Face V=100 V -X Face V=0 V +Y Face insulated -Y Face insulated +Z Face insulated -Z Face insulated	**Case 2**	+X Face insulated -X Face insulated +Y Face V=100 V -Y Face V=0 V +Z Face insulated -Z Face insulated	**Case 3**	+X Face insulated -X Face insulated +Y Face insulated -Y Face insulated +Z Face V=100 V -Z Face V=0 V
CTE	**Case 1**	Free expasion due to ΔT=1000 °K				

$$\begin{bmatrix} q_1 \\ q_2 \\ q_3 \end{bmatrix} = \begin{bmatrix} k_{11} & k_{12} & k_{13} \\ & k_{22} & k_{23} \\ sym & & k_{33} \end{bmatrix} \begin{bmatrix} dT/dx \\ dT/dy \\ dT/dz \end{bmatrix} \quad [28]$$

$$\begin{bmatrix} \sigma_{11} \\ \sigma_{22} \\ \sigma_{33} \\ \tau_{23} \\ \tau_{13} \\ \tau_{12} \end{bmatrix} = \begin{bmatrix} c_{11} & c_{12} & c_{13} & c_{14} & c_{15} & c_{16} \\ & c_{22} & c_{23} & c_{24} & c_{25} & c_{26} \\ & & c_{33} & c_{34} & c_{35} & c_{36} \\ & & & c_{44} & c_{45} & c_{46} \\ & sym & & & c_{55} & c_{56} \\ & & & & & c_{66} \end{bmatrix} \cdot \left(\begin{bmatrix} \varepsilon_{11} \\ \varepsilon_{22} \\ \varepsilon_{33} \\ \gamma_{23} \\ \gamma_{13} \\ \gamma_{12} \end{bmatrix} - \Delta T \begin{bmatrix} \alpha_{11} \\ \alpha_{22} \\ \alpha_{33} \\ 2\alpha_{23} \\ 2\alpha_{13} \\ 2\alpha_{12} \end{bmatrix} \right) \quad [29]$$

$$\begin{bmatrix} J_1 \\ J_2 \\ J_3 \end{bmatrix} = \begin{bmatrix} \sigma_{11} & \sigma_{12} & \sigma_{13} \\ & \sigma_{22} & \sigma_{23} \\ sym & & \sigma_{33} \end{bmatrix} \begin{bmatrix} E_1 \\ E_2 \\ E_3 \end{bmatrix} \quad [30]$$

Table 3.4. Effective material properties for zig-zag structure

Elastic Stiffness	$\overline{C_{ij}} = \begin{bmatrix} 626 & 29 & 112 & & & \\ & 41 & 18 & & & \\ & & 1050 & & & \\ & & & 0.57 & & \\ & & & & 199 & \\ sym & & & & & 0.57 \end{bmatrix}$	***GPa***
Density	2.26	***g/cm3***
Specific Heat	0.17	***cal/(g-K)***
Thermal Conductivity	$\overline{k_{ij}} = \begin{bmatrix} 18.6 & & \\ & 0.06 & \\ sym & & 30 \end{bmatrix}$	***W/(cm-K)***
Coefficent of Thermal Expansion	$\overline{\alpha_{ij}} = \begin{bmatrix} 0.14 & & \\ & 27 & \\ sym & & -1 \end{bmatrix}$	***10^{-6} 1/K***
Electric Conductivity	$\overline{\sigma_{ij}} = \begin{bmatrix} 1334 & & \\ & 6 & \\ sym & & 2000 \end{bmatrix}$	***ohm-cm***

In addition to identifying anisotropic ligament properties at a material point, maximum strength estimates for the zig-zag material are also calculated. The approach uses a widely accepted relationship of proportionality with Young's modulus as shown in Equation 31, where the proportionality constant ranges from 0.05 to 0.1 [84]. This relationship was used in fitting experimental data by Bacon on graphite whiskers resembling ideal graphene sheets. The value used, β=0.025, indicates the presence of defects in the whiskers. Using a range of values and the appropriate moduli from the calculated C_{ij} matrix, estimates of the strength of the zig-zag material are calculated in Table 3.5. Note that this estimate is for tensile strength, and compressive strengths are expected to be higher.

$$\sigma_T^{\max} = \beta E \qquad [31]$$

Table 3.5. Maximum tensile strength estimates for anisotropic zig-zag material

Zig-zag Moduli *GPa*	Proportionality Constant *β*	Estimated Strength *GPa*
C_{11}=626	0.025	15.65
	0.05	31.30
	0.1	62.60
C_{22}=41	0.025	1.03
	0.05	2.05
	0.1	4.10
C_{33}=1050	0.025	26.25
	0.05	52.50
	0.1	105.00

Although the above procedure for describing material anisotropy in a ligament is based on a zig-zag structure, the analytical model can accommodate a wide range of material properties and various degrees of anisotropy. Alternate properties based on additional experimental observation from carbon foams with various additives, or which underwent different processing procedures or heat treatments are possible. Furthermore, the anisotropic material properties can be identified based on a theoretical structure such as that derived from an optimization study.

3.4. Application of Boundary Conditions

In order to introduce load conditions into the various VOI models, the FEA mesh is surrounded by a homogenous medium represented by a thick walled box seen in Figure 3.10. The box slightly overlaps the exposed ligaments that were artificially cut by the selection of a bounding volume and acts to reestablish the connectivity that the VOI experiences in the bulk foam.

Figure 3.10. Single enclosed cavity VOI surrounded by homogeneous medium

The homogeneous medium is meshed uniformly with quadratic hexahedral elements. In the FEA package, ABAQUS, these elements are defined as host elements which constrain the response of any elements that lie inside of it. In this case, the carbon foam VOI elements and any applied coating or infiltration elements that overlap the box are defined as embedded elements. Based on the response of the host elements to any applied boundary conditions, ABAQUS interpolates the response of the embedded elements thus transferring the load to the VOI.

For the single ligament VOI, the homogenous medium is represented with two individual solid boxes on either end of the ligament that surrounds some of the nodal regions as shown in Figure 3.11. Each box is meshed with 4,000 quadratic hexahedral elements connected by 18,501 nodes for a total host volume of 0.220 mm^3. Since the majority of the ligament volume is contained in the nodal regions, approximately 72% of the ligament volume is considered embedded in the host elements and thus constrained to the response of the host geometry.

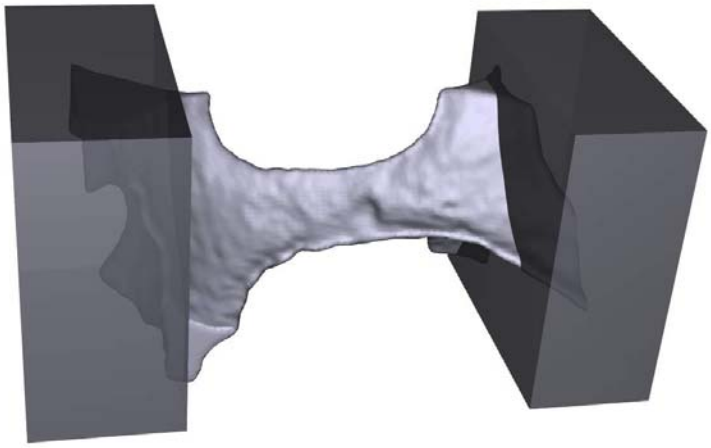

Figure 3.11. Single ligament VOI with host boxes surrounding nodal regions

The homogeneous host box surrounding the single enclosed cavity VOI has a wall thickness of approximately 0.1 mm. It is composed of 60,534 quadratic hexahedral elements and 302,816 nodes encompassing 2.242 mm^3. Of the 74 total ligaments in this VOI, 34 have some part embedded in the homogeneous host representing approximately 7% of the total carbon foam solid volume. Each face of the host element box is shown in Figure 3.12 along with the respective ligament segments considered embedded.

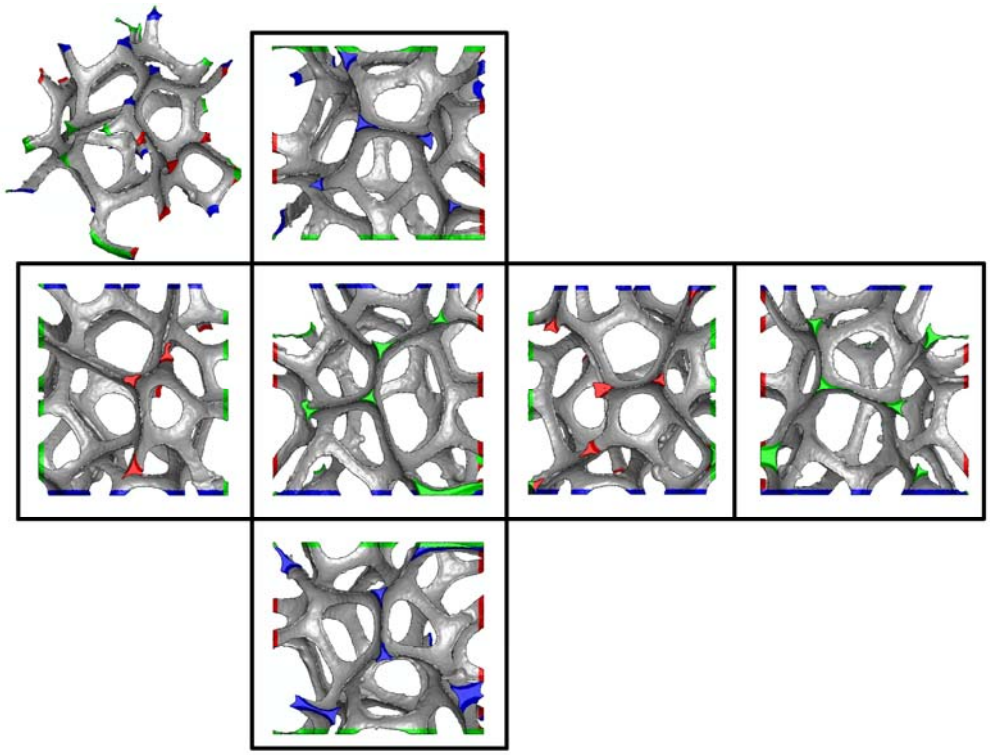

Figure 3.12. Homogeneous host box showing embedded elements for single cavity VOI

For the largest VOI considered, the host box is approximately 3.46 x 3.26 x 3.09 mm with a total volume of 14.2 mm^3. There are 50,912 elements and 242,074 nodes in the homogenous geometry. Approximately 15% of the several interconnected cavity VOI solid volume is considered embedded in the host, with 75 of the 240 total ligaments used to transfer the applied boundary loads into the carbon foam structure. These embedded ligaments are shown in Figure 3.13.

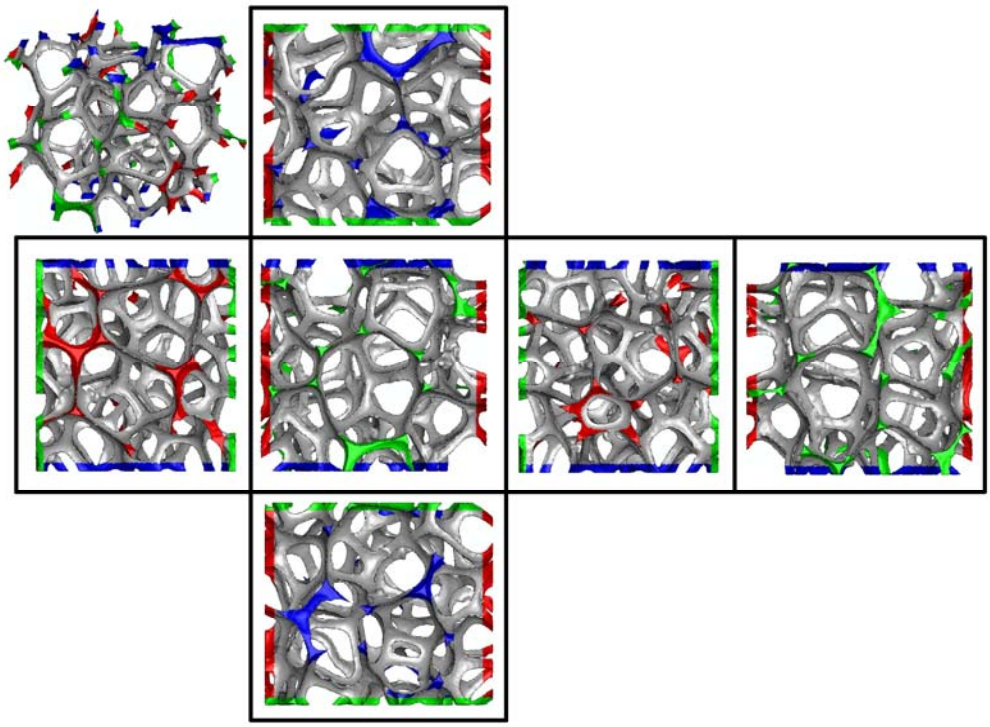

Figure 3.13. Homogeneous host box for several interconnected cavities VOI

3.4.1. Mechanical Field BVP

As a brittle, porous medium, experimental testing on the carbon foam system is primarily limited to compression. For comparison purposes, the applied loading conditions for the model focus on inducing compression to the various VOI models through displacement boundary conditions. Specifically, one side of the homogeneous host box is constrained while the opposite face is subjected to a compressive displacement. By applying the boundary conditions to the entire thickness of one side of the box, the face is considered a rigid body similar to the platens in an experimental compressive test. The pair of faces chosen reflects the direction in the VOI with the most consistent connectivity across the entire dimension as depicted in Figure 3.14, where some faces have been removed for visualization purposes. The specific

displacement boundary conditions are shown in Table 3.6 for each VOI model and represent a global displacement condition of approximately 1% along the chosen dimension.

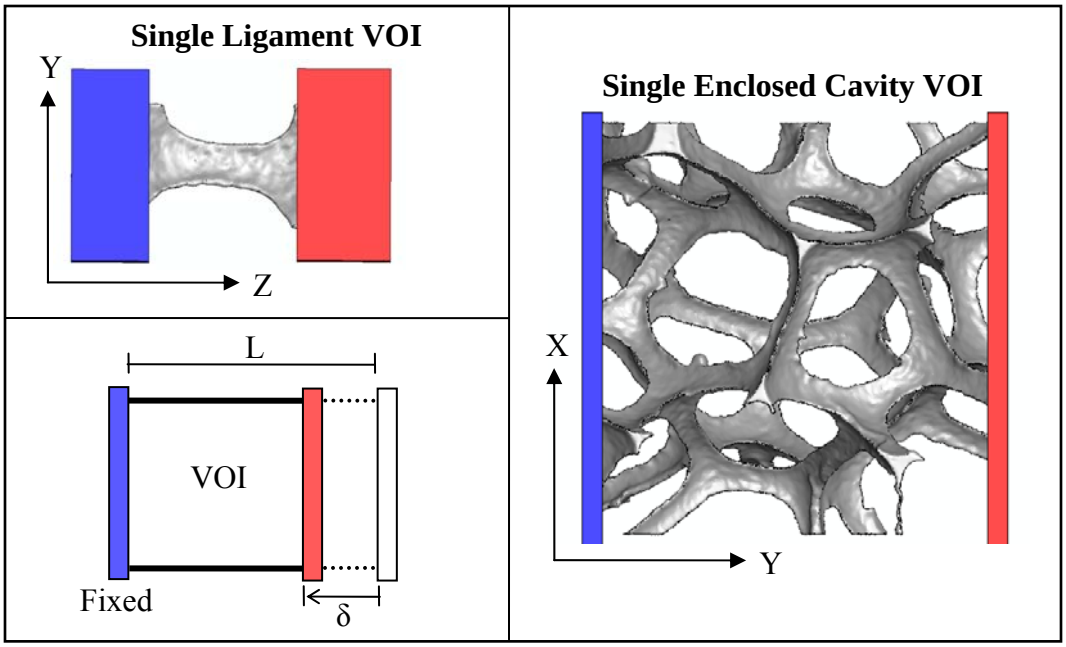

Figure 3.14. VOI faces chosen for application of boundary conditions

Table 3.6. Mechanical BVP applied boundary conditions

	Length (L) *mm*	Displacment (δ) *mm*	-X Face	+X Face	-Y Face	+Y Face	-Z Face	+Z Face
Single Ligament	0.4779	-0.004779	--	--	--	--	u=v=w=0	u=v=0 w=δ
Single Enclosed Cavity	1.9	-0.019	u=0	u=0	v=0	v=δ	w=0	w=0

3.4.2. Thermo-mechanical Field BVP

Although the concept of host and embedded element is convenient for applying boundary conditions to the carbon foam VOI, ABAQUS does not support this method for coupling the thermal degrees of freedom. However, for consistency with loading conditions as the various fields are examined, the identified embedded elements are still considered for load application in the thermal boundary value problem. In this case, the temperature sinks and sources are applied directly to the embedded element nodes. This condition mimics the steady state condition in this region as if the coupling between the host and embedded elements was possible. The specific boundary conditions used in the thermo-mechanical boundary value problems for each VOI are listed in Table 3.7. For the two larger VOI, the applied boundary conditions create a thermal gradient across the structure. The single ligament VOI is studied under a uniform temperature load since in the bulk material a large gradient across a single ligament is unlikely.

Table 3.7. Thermo-mechanical BVP applied boundary conditions

	Length (L) *mm*	Intial Condition *K*	-X Face	+X Face	-Y Face	+Y Face	-Z Face	+Z Face
Single Ligament	0.4779	300	--	--	--	--	1300 K	1300 K
			--	--	--	--	u=v=w=0	u=v=w=0
Single Enclosed Cavity	1.9	300	--	--	1300 K	300 K	--	--
			u=0	u=0	v=0	v=0	w=0	w=0

For the mechanical part of the thermo-mechanical boundary value problem, the coupling is considered sequential as described in Section 2.3. Recall that temperature fields induce mechanical strain from the coefficient of thermal expansion term, however, applied mechanical loads result in negligible temperature changes. Thus after analyzing the thermal part of the problem independently, the temperature field is outputted for

direction inclusion into the mechanical part of the coupled problem. In this case, the host element scheme is reintroduced and serves to constrain the thermal expansion of the VOI similar to what the surrounding bulk foam would do if the VOI had not been artificially removed from it.

There are four contributions to heat transfer in porous media—conduction through solid, conduction through the pore, convection in the pores and radiation across the voids. Studies indicate that conduction through the ligaments is the most significant, with conduction through the pore and convection playing negligible roles [30]. Furthermore, radiation may play a role in heat transfer based on the temperature and geometry of the porous media. In order to identify if radiation is important for the carbon foam VOI geometries identified, small scale studies are undertaken using ideal geometry and established closed form calculations for the net heat exchange (Q_{12}) between two bodies at varying temperature (T_1 and T_2) as shown in Equation 32 [78]. In this case, the heat exchange from body 1 to body 2 depends on the Stefan-Boltzmann constant (σ), the exposed area of body 1 (A_1) and the view factor (F_{12}) along with the surface emissivities (ε).

$$\dot{Q}_{12} = \frac{A_1 F_{12} \sigma \left(T_1^4 - T_2^4 \right)}{\varepsilon_1^{-1} + \varepsilon_2^{-1} - 1} \qquad [32]$$

The emissivity value determines how much energy is absorbed with black bodies ($\varepsilon = 1$) reflecting zero energy back into the atmosphere between the two bodies. Due to its black color, carbon and graphite are typically given emissivity values of 0.85, while copper ranges from 0.05 for a polished surface to 0.74 for a rough surface texture. In using the closed form solutions to determine if radiation should be studied in the carbon

foam VOI models, black bodies will be assumed providing a conservative estimate for radiative heat transfer.

The view factor (F_{12}) is a geometric concept based on the size, shape and orientation of the surfaces to each other [78]. Initially the net heat exchanged between two long adjacent cylinders of identical diameter (φ) is chosen to estimate the heat exchange between two ligaments on opposite sides of a cavity. The ligaments are sized according to the average geometric characteristics of the ligaments in the single enclosed cavity VOI. The view factor for this case is shown in Equation 33. The temperature of body 2 is held at 300 ºK while body one (T_1) takes a range of temperatures from 300 to 2000 ºK. Furthermore a range of distances (x) between the bodies is studied for its impact on heat transfer. Using this configuration, the maximum heat exchange between the two ligaments is on the order of 0.003 W which would produce a minimal temperature increase in body 1 of less than 0.01 ºK.

$$F_{12} = \frac{1}{\pi}\left\{\left[\left(1+\frac{x}{\phi}\right)^2 - 1\right]^{1/2} + \sin^{-1}\left[\frac{1}{1+\frac{x}{\phi}}\right] - \left[1+\frac{x}{\phi}\right]\right\} \qquad [33]$$

The second geometric configuration investigated is the net heat exchanged between two interior sections of a single sphere of radius (R). The areas are sized according to the visible surface of an averaged sized ligament when viewed in profile. The view factor for this case is shown in Equation 34. The temperature of body 2 is held at 300 ºK while body one (T_1) takes a range of temperatures from 300 to 2000 ºK. Furthermore a range of area ratios is studied for its impact on heat transfer. Using this configuration, the maximum heat exchange between the two ligaments is on the order of 0.01 W which would produce a temperature increase in body 1 of less than 0.1 ºK.

$$F_{12} = \frac{A_2}{4\pi R^2} \qquad [34]$$

Therefore using a conservative estimate with black bodies, both geometric configurations produced closed form solutions with negligible temperature increases for the range of temperatures considered in this research. Based on these calculations and previous findings in literature, both radiation and convection are neglected in the thermo-mechanical BVP and conduction through the ligaments is the sole means of heat transfer studied for the carbon foam VOI models.

3.4.3. Thermal-electrical Field BVP

As in the case of thermal loading, electrical degrees of freedom are also not coupled between host and embedded elements and the applied boundary conditions are applied directly to the embedded element nodes. For the electrical part of this coupled field, the boundary conditions are chosen to mimic a small electric circuit where the carbon foam ligament acts to complete the circuit. Using the same faces as previously identified, a voltage potential is applied across the structure inducing a current flow. The specific boundary conditions for the thermal-electrical boundary value problem are given in Table 3.8.

Table 3.8. Thermal-electrical BVP applied boundary conditions

	Length (L) *mm*	Intial Condition *K*	-X Face	+X Face	-Y Face	+Y Face	-Z Face	+Z Face
Single Enclosed Cavity	1.9	300	--	--	1 V	0 V	--	--
			--	--	--	300 K	--	--
Several Interconnected Cavities	2.83	300	--	--	1 V	0 V	--	--
			--	--	--	300 K	--	--
			u=0	u=0	v=0	v=0	w=0	w=0

The typical method of coupling the thermal problem to the electrical is in defining electrical properties based on the current temperature, however the properties in Table 3.4 are not included as a function of temperature in the models. Therefore, the electric problem is decoupled from the thermal analysis problem. This is not the case when considering the influence of the electrical problem on the final temperature field during the thermal part. The internal heat generation term, also referred to as Joule heating and discussed in Section 2.3, is a direct function of the electric current flowing through the carbon foam medium thus influencing the temperature profile. A temperature sink is applied to the same face where the electric ground is applied as shown in Table 3.8.

3.5. Multi-functional Investigations

Recall from Section 1.1 that one focus of multi-functionality in the carbon foam system is tailoring its mechanical stiffness and strength. Current carbon foams do not meet critical structural performance requirements and tend to have a brittle failure. In order to address this limitation and demonstrate tailoring of the bulk stiffness, various coating and infiltration along with changes in material anisotropy are considered. Tailoring of thermal and electrical conductivity response is also addressed by introducing metal coatings to the carbon foam ligament structure.

3.5.1. Impact of Orientation

In order to understand the impact of material anisotropy and orientation, the identified anisotropic effective properties from Section 3.3 are incorporated into the analytical models by identifying a local material coordinate for each ligament in the carbon foam mesh developed in Section 3.1. Note that polarized OM and SEM images indicate that the zig-zag structure also occurs in the foam nodes; therefore, the nodes are treated as an extension of the individual ligaments with the transition in material orientation buried in the carbon foam nodes. This is depicted in Figure 3.15 for an arbitrary VOI where each color represents a unique material coordinate system for the orientation of the zig-zag material.

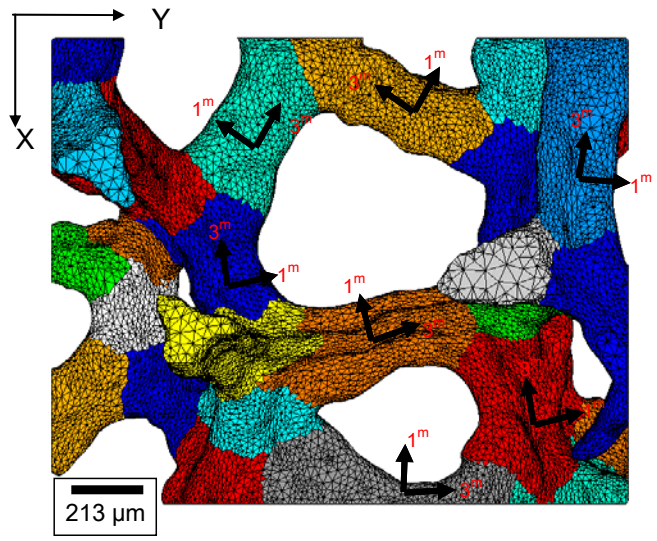

Figure 3.15. Individual anisotropic material orientations for an arbitrary VOI

Although the choice of material coordinate orientation for each ligament is arbitrary, polarized OM images suggest that each ligament has a dominant orientation along its length. Therefore, the zig-zag material 3^m axis is aligned with the ligament axis creating the stiffest, most thermally and electrically conductive ligaments possible. Additional orientations are considered as simple rotations using the same effective zig-zag anisotropic material properties.

3.5.2. Impact of Coatings and Infiltration

Several material systems are used for both the coating and the infiltration phases in the carbon foam models in order to meet the multi-functionality objectives of tailored mechanical stiffness and bulk conductivities—thermal and electrical. The first coating and infiltration considered is copper, shown in Table 3.9, to improve both the mechanical stiffness and bulk conductivities. Initial experimental tests on carbon foams with thin (2-3 μm) copper coatings show overall improved stiffness as well as alteration of the damage mode from brittle to gradual crushing at the loading surfaces. In addition, thin coatings on non-graphitized carbon foams improve the bulk thermal conductivity up to 2-3 orders of magnitude, with similar results expected for electrical conductivity [85]. For comparison to experimental testing, alternate isotropic carbon foam material properties, shown in Table 3.9, are considered when coating and infiltrating with copper.

Table 3.9. Coating, infiltration and alternate carbon foam material properties

	Density	Specific Heat	Modulus	Coefficient of Thermal Expansion	Bulk Thermal Conductivity	Electric Resistivity
	g/cm^3	*J/(kg-K)*	*GPa*	*10^{-6} 1/°K*	*W/m-K*	*ohm-m*
Copper [23]	8.94	386	110	17	398	1.67E-08
PLLA [86,87,88]	1.24	1200	1.15	--	0.13	4.90E-17
Graphite Foam [1,20-21]	0.59	691	0.18	2	134	1.00E-05
RVC Carbon Foam [17-18]	0.042	1.26	0.045	2	0.085	7.50E-03

The second material considered for coating and infiltration is a bioresorbable polymer poly(l-lactic acid), or PLLA. The selection of this material supports ongoing research attempts to find alternative material systems for biomedical devices such as orthopedic bone plates. The objective of current research is tailoring the mechanical stiffness of the orthopedic device to mimic that of natural bone to prevent stress shielding as the bone heals [32]. In this particular instance, the carbon foam, a potentially biocompatible material, acts as a reinforcing structure for the bioresorbable polymer.

In addition to material composition, it is also of interest to understand the impact of imperfect coatings and infiltrations in the carbon foam material system. Recall that the idealized coating layers are uniform in thickness and perfectly bonded with the carbon foam; however, if desired, these conditions can be relaxed. To model uneven coatings such as that which appears in Figure 3.2, initially several layers of coating elements are generated with the above procedure to mimic the thickest coating dimension. In the areas where the coating is thinned, a few of these layers are removed thus providing an uneven coating thickness as the surface is traversed.

In addition to evaluating inconsistent coating thicknesses, complete regions of coatings can be removed to study the impact of missing coatings. Furthermore, by disconnecting the swept elements from the underlying carbon foam ligaments through node duplication, areas of coating debond are assessed for impact on material response. As with the coating element generation, the resulting infiltration also has a perfect interfacial bond with the carbon foam substrate, which can be relaxed to study debond areas. Moreover, regions of infiltration elements can be removed to investigate incomplete infiltrations such as that shown in Figure 3.16, where the infiltration failed to penetrate into the porous interior.

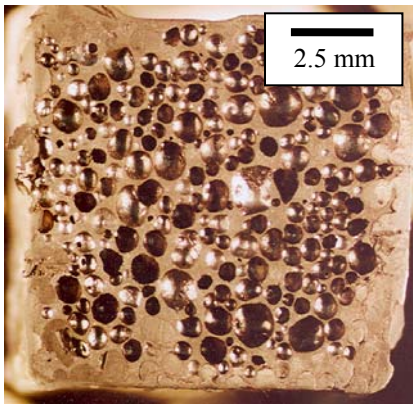

Figure 3.16. Incomplete infiltration of carbon foam with polycaprolactone (PCL)

The next sections describe specific examples to illustrate the developed models. Observations regarding the effect of potential multi-functional changes—anisotropy and coatings—are based on qualitative discussion of the material response to the applied fields with an emphasis on load path identification. Also of interest is the interface between the ligaments and any coatings or infiltrations to identify potential stress concentrations or other perturbations.

4. SINGLE LIGAMENT VOI STUDY

The single ligament VOI in Figure 4.1 is the lowest geometric scale and incorporates various features of the ligament including cross sectional taper, curvature and other imperfections. The impact of ligament anisotropy and coating in creating multi-functional carbon foam are evaluated through the mechanical, thermal and electric response.

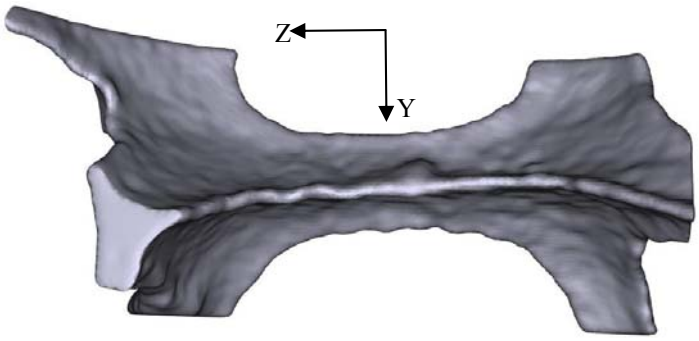

Figure 4.1. Single ligament VOI with adjacent nodal regions

4.1. Effect of Coating on Improving Response of Cracked Ligaments

4.1.1. Problem Description

Herein the focus is on typical cracks whose axes are parallel to the ligament axis to illustrate the influence of coatings on the mechanical response of the ligament. The objective is to understand how cracks impact the overall effective ligament properties as a function of crack depth.

Cracks such as these are a direct consequence of processing conditions when creating carbon foams and occur during the heat treatment process when molecular weight changes cause shrinkage. Furthermore, investigation of processed carbon foams with metallic coating suggest that in addition to coating the structure, any cracks on the surface are filled as shown in Figure 4.2. Therefore, this illustration is extended to investigate the impact of coatings on tailoring the mechanical response when cracks are filled with the coating.

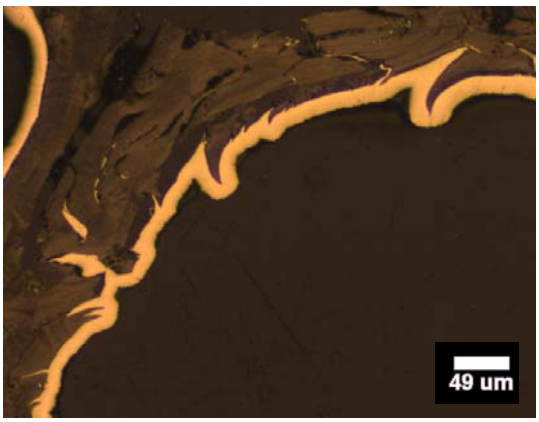

Figure 4.2. Optical microscopy image of metallic coated carbon foam with cracks

The set of anisotropic properties calculated for a zig-zag structure in Section 3.3 are utilized here where the highest modulus in the C_{ij} matrix is oriented along the ligament axis. Since there is a single material orientation, the problem coordinate is identical to the material coordinate and is centered between the nodal regions at the cross section center. The coating thickness is 5 μm and is composed of copper with the relevant properties shown in Table 3.9. The crack, shown in blue, is located on one face of the ligament's triangular cross section and is centered in an area of interest colored red in Figure 4.3.

The crack has a square cross sectional profile with a length of 0.12 mm and a constant width of 0.025 mm. Three crack depths—shallow, medium and deep—are considered as with respective volume fractions of 0.02, 0.04 and 0.06 with respect to the area of interest volume. The view in Figure 4.4 represents a cut plane taken at the ligament center span, or $Z=Z^{L}=3^{m}=0$.

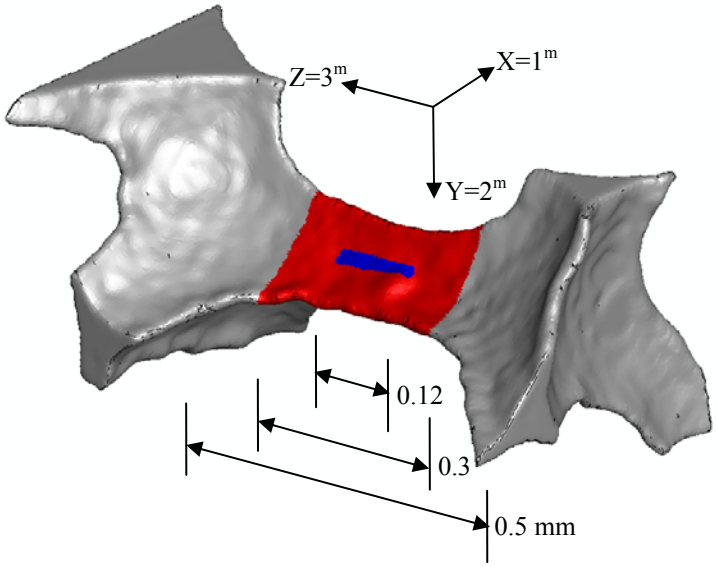

Figure 4.3. Single ligament VOI with a crack

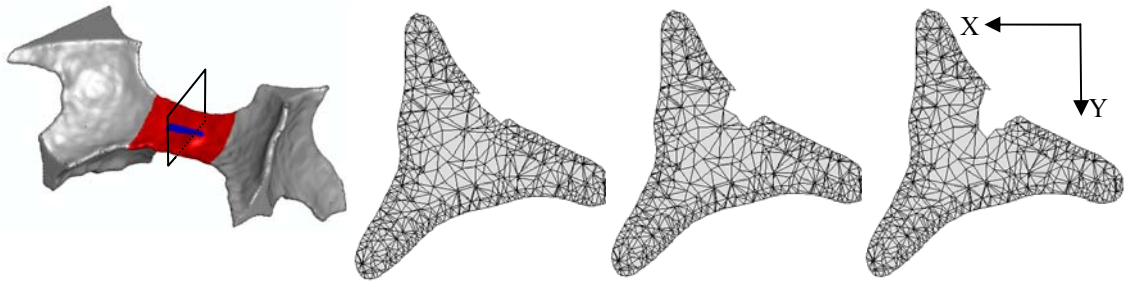

(a) (b) (c)

Figure 4.4. Ligament cross section showing a (a) shallow, (b) medium and (c) deep crack

In addition to representing different volume fractions, the three cracks are also identified by the number and size of the elements composing them. Recall from Section 3.1, that to optimize computational resources, the advancing front scheme used to mesh the ligament structure is invoked with a gradient option. This results in a fine mesh at the surface and a coarse mesh at the ligament centers as shown in Figure 4.5. Consequently, the shallow crack is composed of many elements and is approximately one layer of elements thick. The medium crack consists of this layer of elements plus a second coarser layer. This trend continues with the deepest crack, where the added elements are approximately an order of magnitude larger in volume than the shallow crack elements.

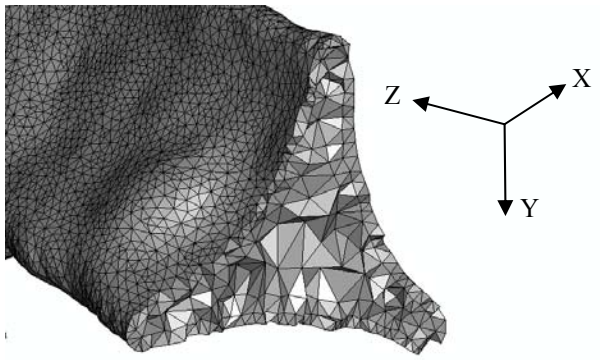

Figure 4.5. Cross section with mesh coarsening between the surface and interior

4.1.2. Results

In order to quantitatively compare the three depths of cracks, an effective modulus for the ligament in the loading direction is evaluated utilizing strain energy density. Details of this procedure are outlined in Appendix C. This calculation is performed on the area of interest to avoid any boundary effects near the loading surfaces with the volume representative of an uncracked ligament.

As expected, the presence of a crack lowers the bulk effective modulus for the ligament as listed in Table 4.1 when subjected to a compressive load along the ligament axis. For a shallow crack on the ligament surface, the effective modulus decreases by 25 GPa, or 2%, from its original 1050 GPa. In addition, the depth of the crack also influences the effective modulus with a 5 GPa decrease for an additional 0.02 crack volume fraction. At this VOI scale, these changes are fairly small; however, as the VOI size is increased these small changes are expected to have a large influence on the overall bulk behavior of the carbon foam.

Table 4.1. Effective modulus and volume fractions for three crack depth geometries

		Shallow	Medium	Deep	
Crack Volume Fraction	v_f	0.0157	0.0365	0.0565	
Effective Modulus	E_z	1024.9	1020.3	1015.7	***GPa***

Recall that the boundary conditions placed on the host elements is consistent among the three crack depth cases as listed in Table 3.6. As such, the compressive displacement (u_z) is similar among the three cases. However, some changes are detected among the other two displacement components. Both of these displacements are characteristic of a twisting deformation around the ligament axis as shown in Figure 4.6 for the shallow crack case. The black wire frame represents the original positions while the green shaded region is the deformed position of the ligament. This deformation plot also suggests localized deformation in the area of the ligament ridges as shown in Figure 4.7.

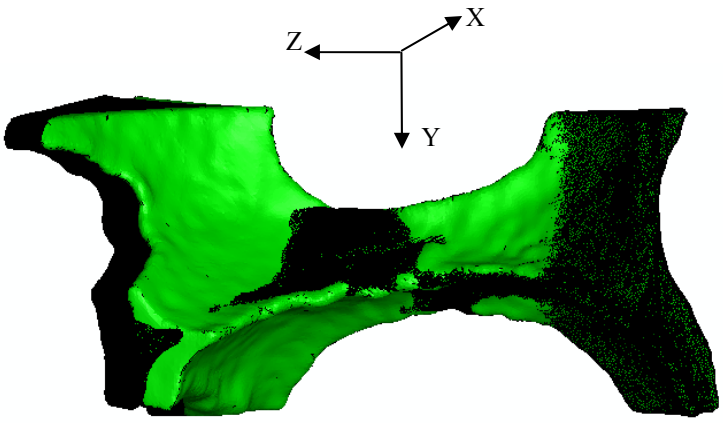

Figure 4.6. Single ligament VOI deformation (10× scale) for shallow crack geometry

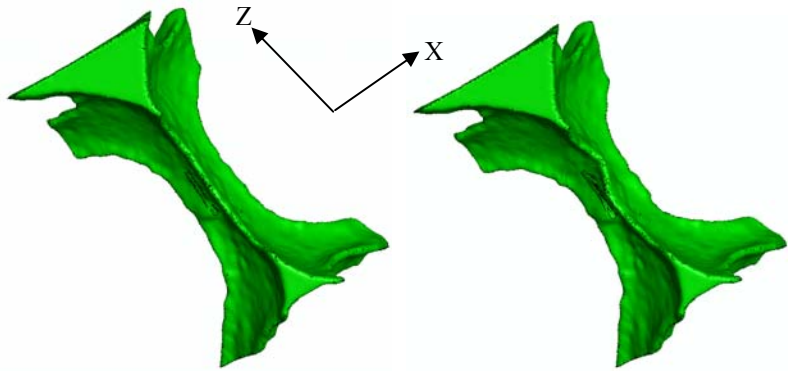

(a) (b)

Figure 4.7. Ridge position at (a) reference and (b) deformed configuration (10× scale) for shallow crack geometry

Additional information about the impact of cracks and crack depth on mechanical response is obtained by closer investigation of the displacement contours. In this case, a direct relationship between crack depth and torsional rotation about the ligament axis is notable. As the crack depth increases, the torsional rigidity appears to decrease allowing for more rotation about this axis.

In addition to identifying the effect of cracks on overall deformation, individual stress contour plots are also studied for potential changes as a function of crack depth. Initially the surface of the ligament is examined to identify features other than the crack which may act as stress concentration points. Although the surface of the ligament appears to be smooth from a macroscopic perspective, when the surface is examined closely it has an uneven topology with low frequency changes. However, on one end of the crack region there is a noticeably large surface feature as shown in Figure 4.8 that is expected to influence the stress contours. This feature is included in all three crack depth cases and equally influences all cases so that comparison among the cases can be made.

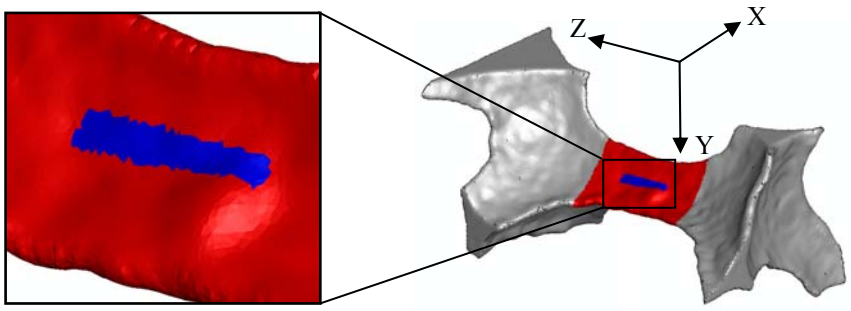

Figure 4.8. Surface feature near crack in single ligament VOI model

The stress state in the single ligament VOI is dominated by the normal stress along the ligament axis which is 2-4 orders of magnitude higher than the other components. This normal stress component is examined to identify the impact of crack depth on the stress state. In the area of interest, some changes in the stress contours adjacent to the crack are found, such that deeper cracks result in larger stress magnitudes as in Figure 4.9. Furthermore, when considering cross section at $Z=Z^{L}=3^{m}=0$, additional impact on this stress component is evident. Note that the mesh in this model is not fine enough to fully investigate stress concentrations near the crack geometry as a damage initiation point; therefore the crack depth impact is limited to relative comparisons between the cases.

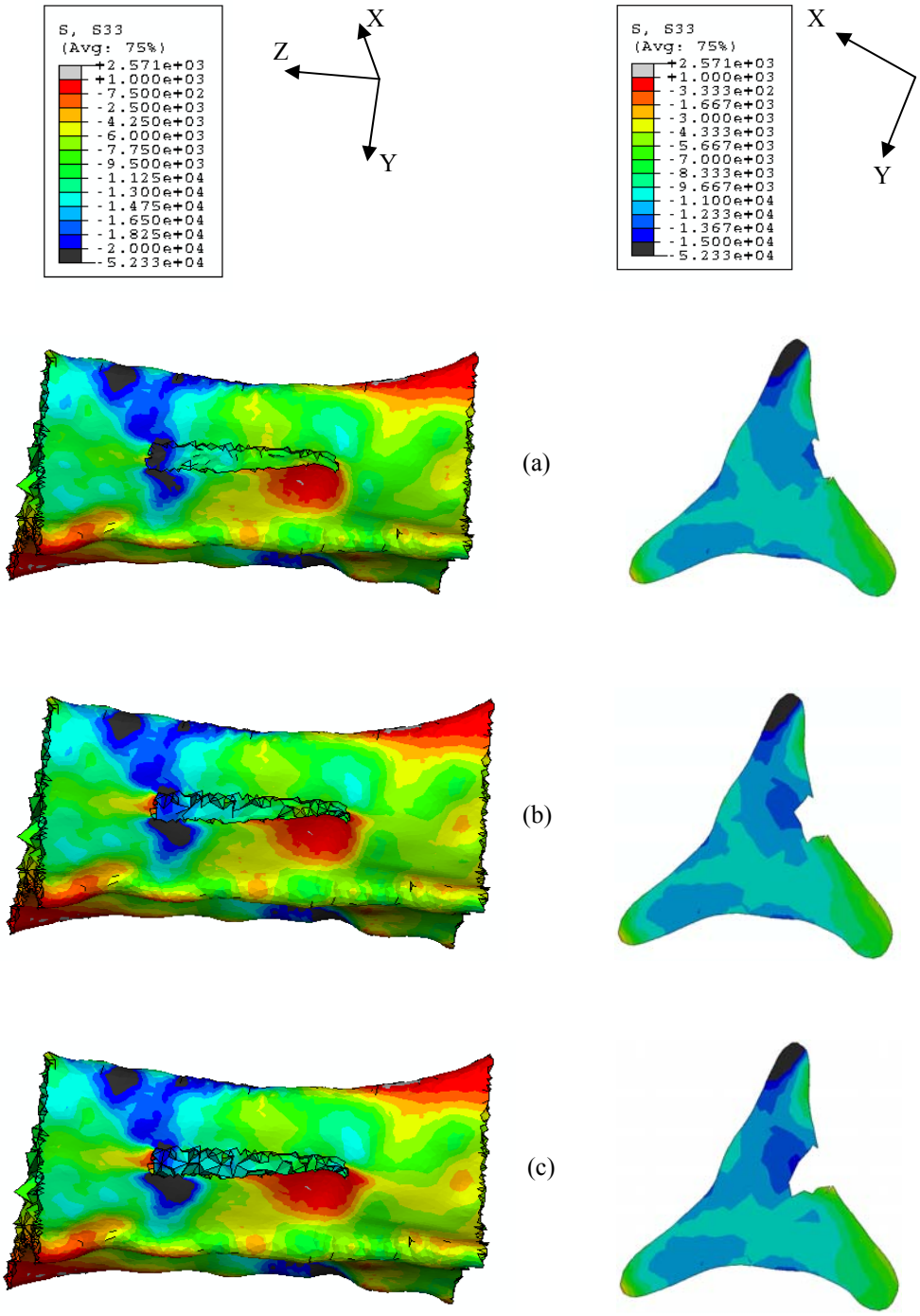

Figure 4.9. Normal stress (σ_{zz}) in area of interest and ligament cross section for (a) shallow, (b) medium and (c) deep crack depths

After confirming the impact of crack depth on ligament deformation and stress states, a second set of analyses is undertaken to identify the impact of thin copper coatings. The copper coating is uniformly applied to the ligament surface and is modeled to also fill the crack, with a perfect interfacial bond.

Following the procedure previously identified, an effective modulus is calculated for each depth of copper filled cracks. As expected from a rule of mixture calculation, the 0.24 volume fraction of copper significantly impacts the overall effective modulus since the modulus of copper is an order of magnitude smaller than the anisotropic zig-zag material. This result is listed in Table 4.2 along with the previously calculated effective moduli for uncoated ligaments with various crack depths.

Table 4.2. Effective modulus for three crack depths with and without Cu coatings

		Shallow	Medium	Deep	
Crack Volume Fraction	v_f	0.0157	0.0365	0.0565	
Effective Modulus, uncoated	E_z	1024.9	1020.3	1015.7	***GPa***
Effective Modulus, w/ Cu	E_z	837.2	835.1	833.3	***GPa***

In addition to decreasing the effective modulus of the carbon foam ligament, the copper coating also alters the deformation state under the same boundary conditions. Recall that the twisting deformation about the ligament axis is a function of the crack depth. When the ligaments are thinly coated with copper, this deformation (u_x) is noticeably

reduced as shown in Figure 4.10, where the uncoated ligaments are plotted for comparison at the same scale. Furthermore, the coated cases appear more uniform than the uncoated cases, indicating that by filling the cracks their impact is reduced and the overall deformation is driven more by the surface topology and ligament geometry.

As in the case of uncoated carbon foam ligaments, the normal stress along the ligament axis dominates the stress state by 2-4 orders of magnitude. Examination of this stress component in the foam elements indicates that inclusion of a copper coating diminishes this stress component in the area of interest. Furthermore, stress concentrations in areas adjacent to the filled crack decrease as shown in Figure 4.11, where the coating is removed for visualization purposes, compared to the previous uncoated cases shown in Figure 4.9.

In the coating layer, the stress magnitudes are up to 2 orders of magnitude less than in the foam as illustrated in Figure 4.12. The coating undergoes compressive stress in the loading direction in the range of -400 to 100 MPa, with a few stress concentration areas undergoing stress up to ±1000 MPa. These stress concentrations are driven by the geometry of the carbon foam ligament such as the edge ridges or surface irregularities.

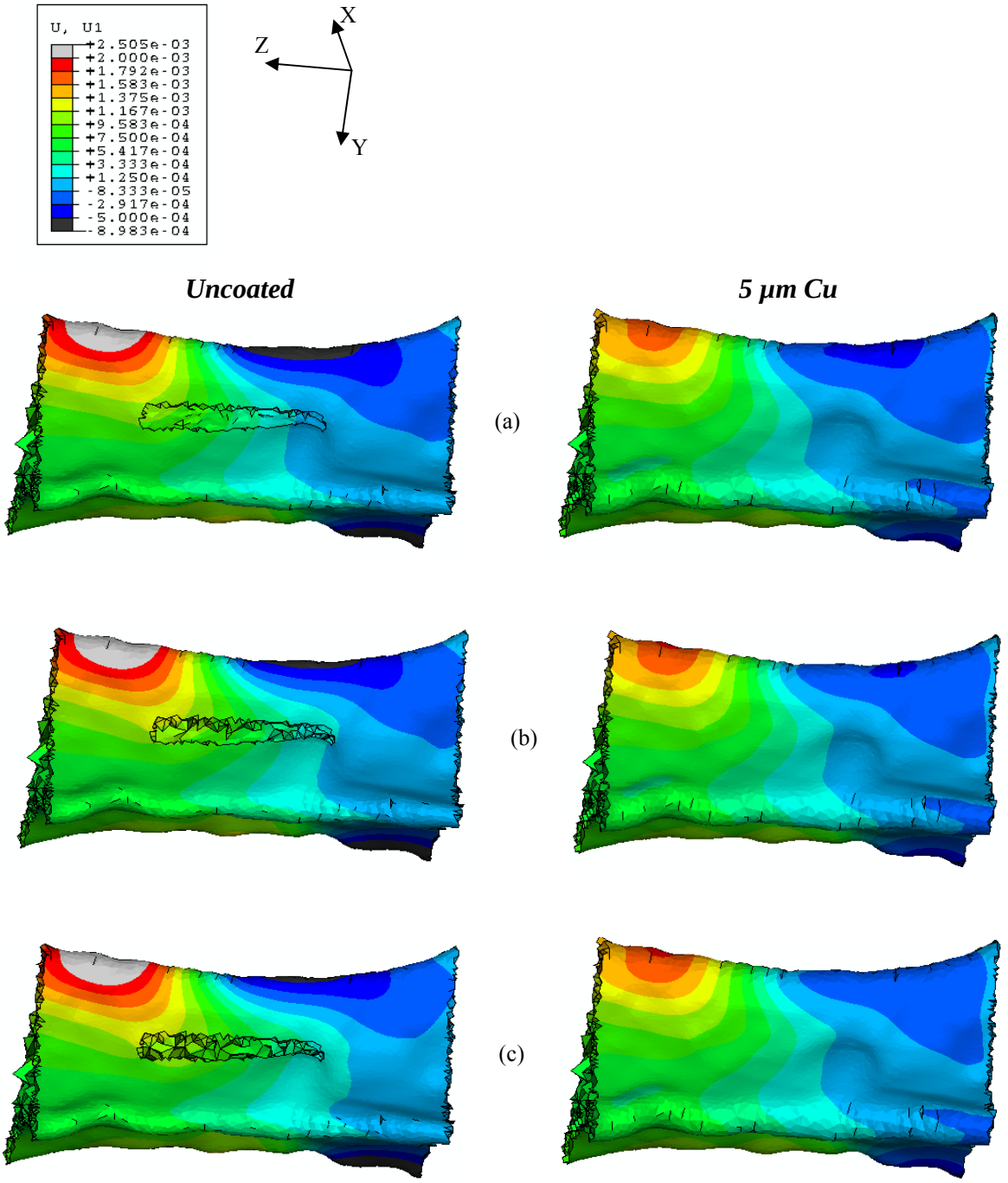

Figure 4.10. Twisting displacement (u_x) for (a) shallow, (b) medium and (c) deep crack depths for both uncoated and coated ligaments

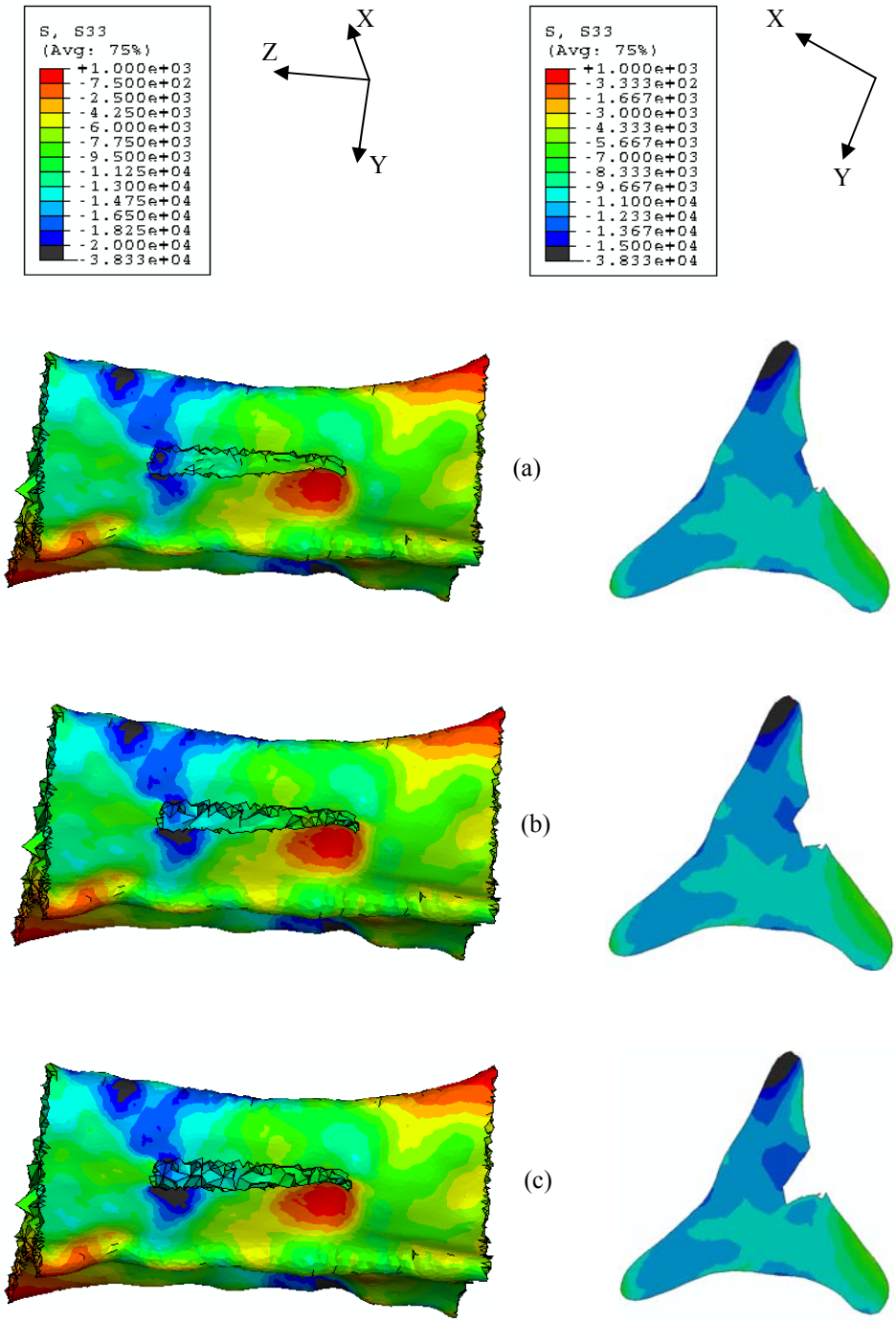

Figure 4.11. Normal stress (σ_{zz}) in area of interest and cross section of foam elements for (a) shallow, (b) medium and (c) deep crack depths for 5 μm Cu coatings

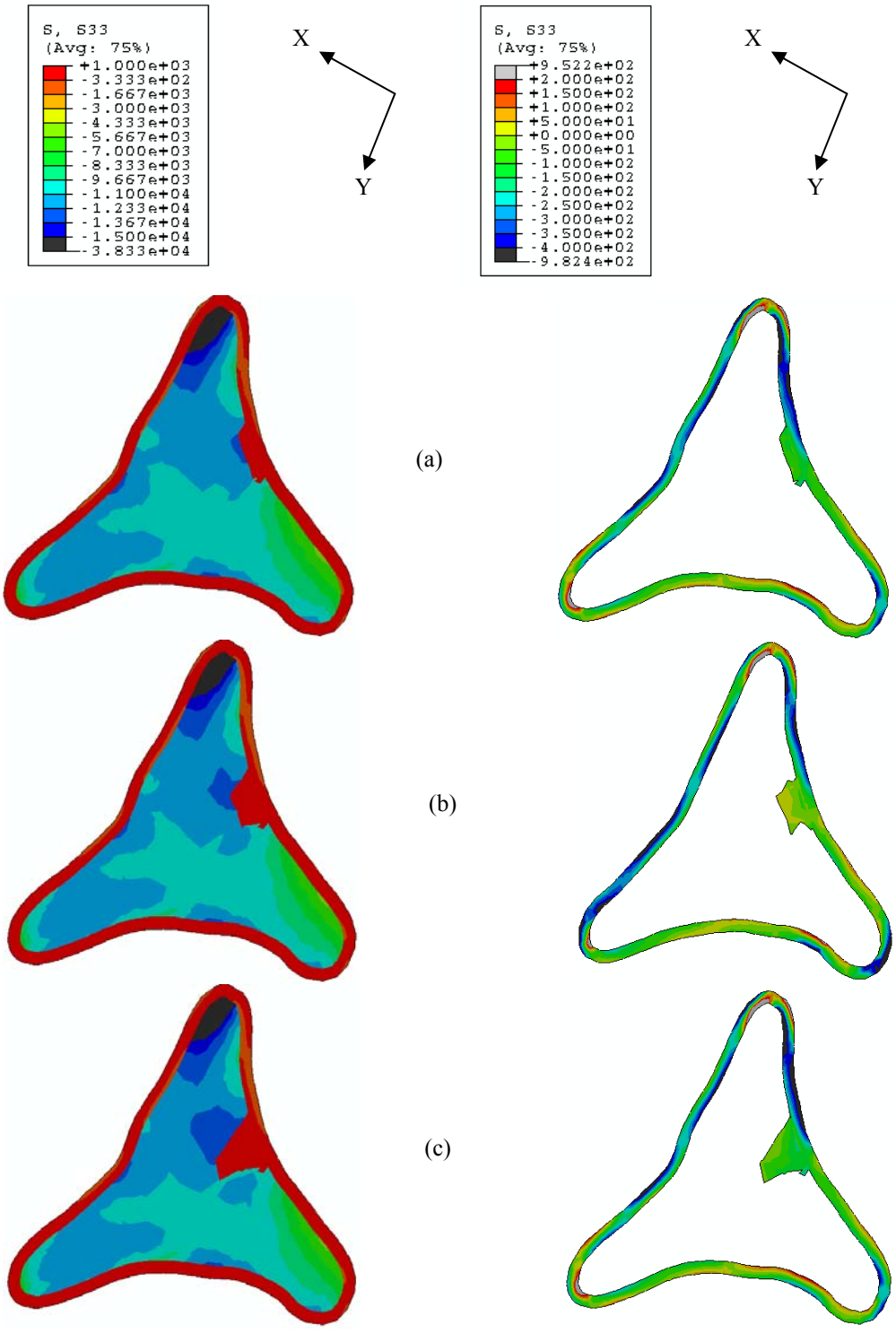

Figure 4.12. Normal stress (σ_{zz}) in composite cross section and coating layers for (a) shallow, (b) medium and (c) deep crack depth with 5 µm Cu coatings

4.1.3. Observations

In this illustration, the impact of cracks on mechanical response is investigated using the single ligament VOI model. Initial studies on uncoated foams suggest a direct relationship between crack depth and effective modulus. A single, shallow crack reduces the overall ligament effective modulus 25 GPa, while the deeper cracks reduces this an addition 5-10 GPa. Although this reduction is 2-3% of the original ligament modulus, studies at larger scales indicate that this small change can have significant impact on the bulk behavior of a large sample of carbon foam.

The crack depth also changes the deformation and stress state of the ligament undergoing compressive loading. The deformation of each crack configuration is characterized by a twisting mode about the ligament axis. Deeper cracks have larger displacements indicating reduced torsional stiffness. Furthermore, as the crack depth increases, the normal stress along the ligament axis increases especially in areas of stress concentration near the crack and other surface irregularities. Consequently, processing researchers should focus on eliminating cracks arising from processing procedures in order to improve stiffness of bulk carbon foams and reduce stress concentration points.
When the ligament is coated filling the crack, the twisting deformation and the compressive stress along the ligament axis is reduced. However, this comes at the cost of a large reduction in effective modulus of up to 20%.

Filling the cracks with the coating also impacts the stress concentrations near the crack and acts to diminish their magnitude. The coating layer itself undergoes a much lower stress state than the foam as expected from its order of magnitude lower modulus, but its magnitude is high for a standard copper alloy. However, processing researchers studying RVC carbon foams coated with thin 2-3 μm copper coatings have identified a strong copper property [85]. This high strength copper is likely due to the electro-chemistry procedure used to coat the carbon foams which deposits multiple layers of

copper to achieve the full thickness value. By depositing the copper in many thin layers, a fine, uniform grain structure is developed reducing potential slip planes and resulting in enhanced strength properties.

4.2. Effect of Coating on Interface Conditions

4.2.1. Problem Description

In order to support ongoing research in this area, two coatings are identified and applied to the single ligament VOI. The metallic coating is copper which is used in many thermal management applications to improve conductivity. The second material is a bioresorbable polymer, PLLA, used in bio-medical devices. The objective of this study is to understand how the coating impacts thermal expansion deformation under a wide range of temperature values.

A uniform, 5 μm coating is swept from the ligament surface as previously described in Section 3.1.2, with perfect bonding to the substrate. Next, a uniform temperature field is applied to the ligament and coating to generate thermal expansion through CTE coupling. This deformation is limited by constraining the host boxes from displacing according to Table 3.7, similar to what the adjacent carbon foam structure imparts on this ligament in the bulk body. By applying the temperature incrementally from ambient to a maximum value, the effect of temperature on thermal stresses is identified for an uncoated, copper coated and PLLA coated single ligament VOI. The applied temperature profile is taken as a linear function from the initial condition of 300 ºK to the final temperature in steps of 10 ºK. The maximum temperature for the polymer coating is limited to 400 ºK in order to stay below its glass transition temperature, while the uncoated and copper coated ligaments have a maximum temperature of 1300 ºK.

4.2.2. Results

Initially, the thermo-mechanical response of an uncoated carbon foam ligament is investigated to understand the free expansion of the ligament prior to introducing the coating. Recall that the constraint placed on the single ligament VOI by the host boxes restricts the deformation of the ligament along its axis. By placing this constraint on the ligament, the ligament is forced into a bending deformation mode about the ligament axis as shown in Figure 4.13 for the uncoated case at its final temperature of 1300 ºK. Notice that the top of the ligament is moving left while the bottom displaces in the opposite direction. The other two displacement components are characterized by dilation with a twisting motion; however, the value of these two displacements is an order of magnitude less than the expansion along the ligament axis.

When a thin (5 μm) copper coating is applied to the ligament, the deformation of the carbon foam is similar to the uncoated ligament at the maximum temperature considered of 1300 ºK. The magnitudes of the three components are comparable, with the notable exception that in the area of the ligament ridges the deformation is slightly decreased. In the area of the ridges, the foam volume is thinned and represents an equal volume with the copper coating. Therefore the copper coating is likely influencing the expansion of the carbon foam in these areas. Furthermore, when the outermost surface is considered in both the uncoated and copper coated cases, the influence of the copper is more notable with larger displacements occurring in each component. Recall that the copper has a larger CTE value compared to the zig-zag material system indicating that under the same temperature load it experiences higher thermal strains.

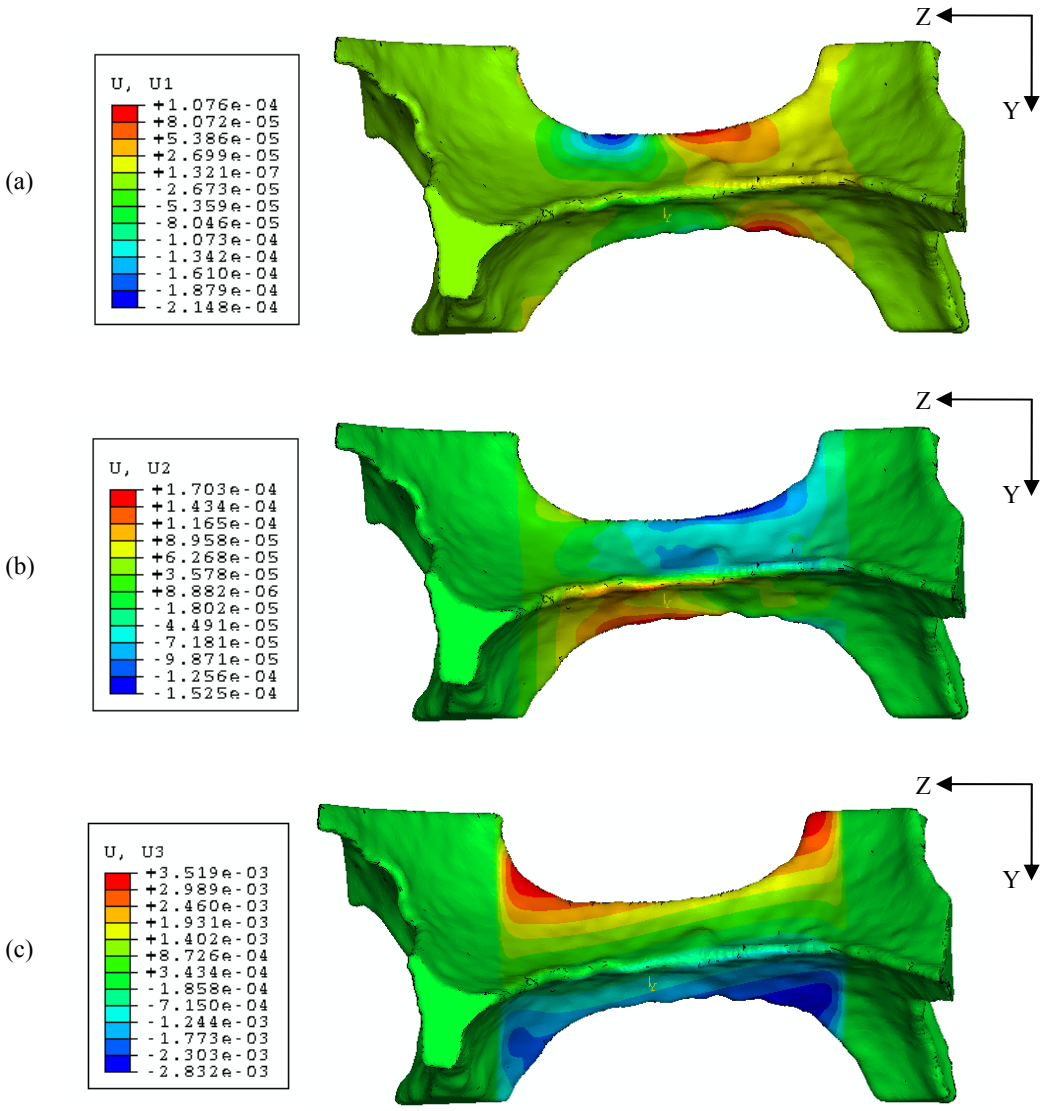

Figure 4.13. Deformation characterized by displacements (a) u_x (b) u_y and (c) u_z for uncoated ligament at 1300 ºK

To further investigate the impact of coating on thermal strain and stresses, a cross section at the ligament center is identified to quantify changes as temperature is increased. Figure 4.14 depicts each of the normal strains at this cross section in both the uncoated and copper coated cases, where the coating elements have been removed for

visualization purposes. The largest normal strain is the ε_{yy} component which corresponds to the largest CTE value in the anisotropic α_{ij} matrix for the zig-zag material shown in Table 3.4. In all three components, the ligament coated with copper is undergoing higher strains than the uncoated case. Recall that the copper coating has a high CTE value compared to the carbon foam indicating that for a similar temperature load a higher thermal strain is produced. At any given temperature, the copper is undergoing one order of magnitude higher thermal strains as shown in Figure 4.15 for the normal strain components.

The higher CTE expansion of the copper coating also appears to impact the shear strain components in the carbon foam elements as shown in Figure 4.16. The magnitude of these shear strains are the same order as the normal strain components with any differences attributed to the anisotropic nature of the carbon foam material system. These strains indicate a twisting of the carbon foam ligament in the various planes, similar to the result found investigating the displacement components. The shear strains for the copper layer are plotted in Figure 4.17 for comparison purposes.

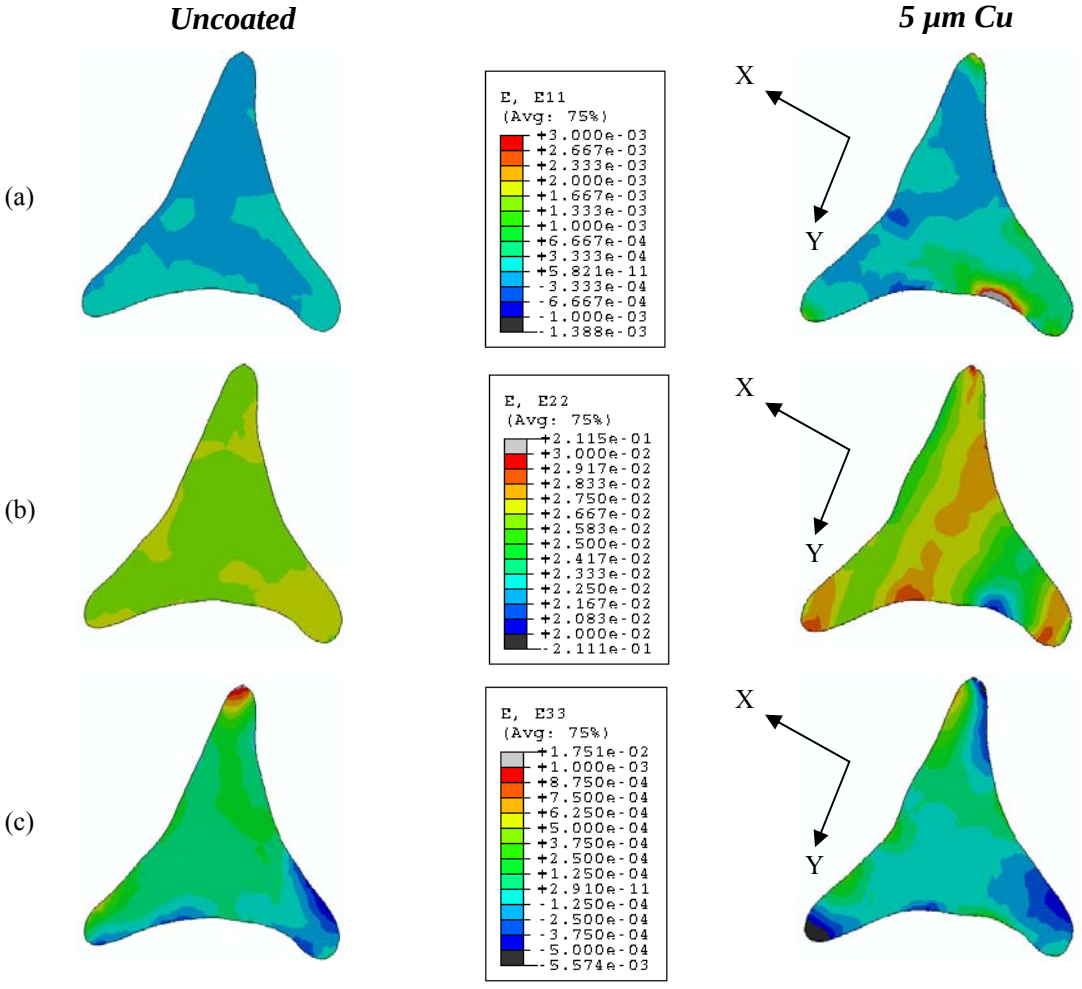

Figure 4.14. Thermal strain components (a) ε_{xx} (b) ε_{yy} and (c) ε_{zz} for both uncoated and Cu coated ligaments at 1300 ºK

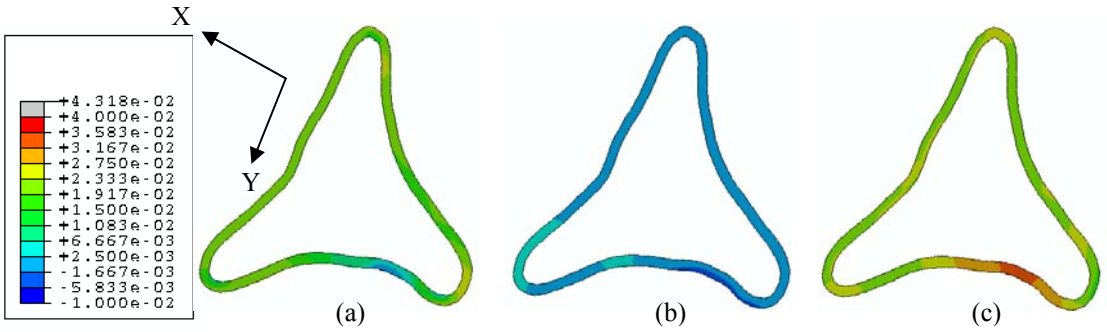

Figure 4.15. Thermal strain components (a) ε_{xx} (b) ε_{yy} and (c) ε_{zz} for coating layer in Cu coated ligament at 1300 ºK

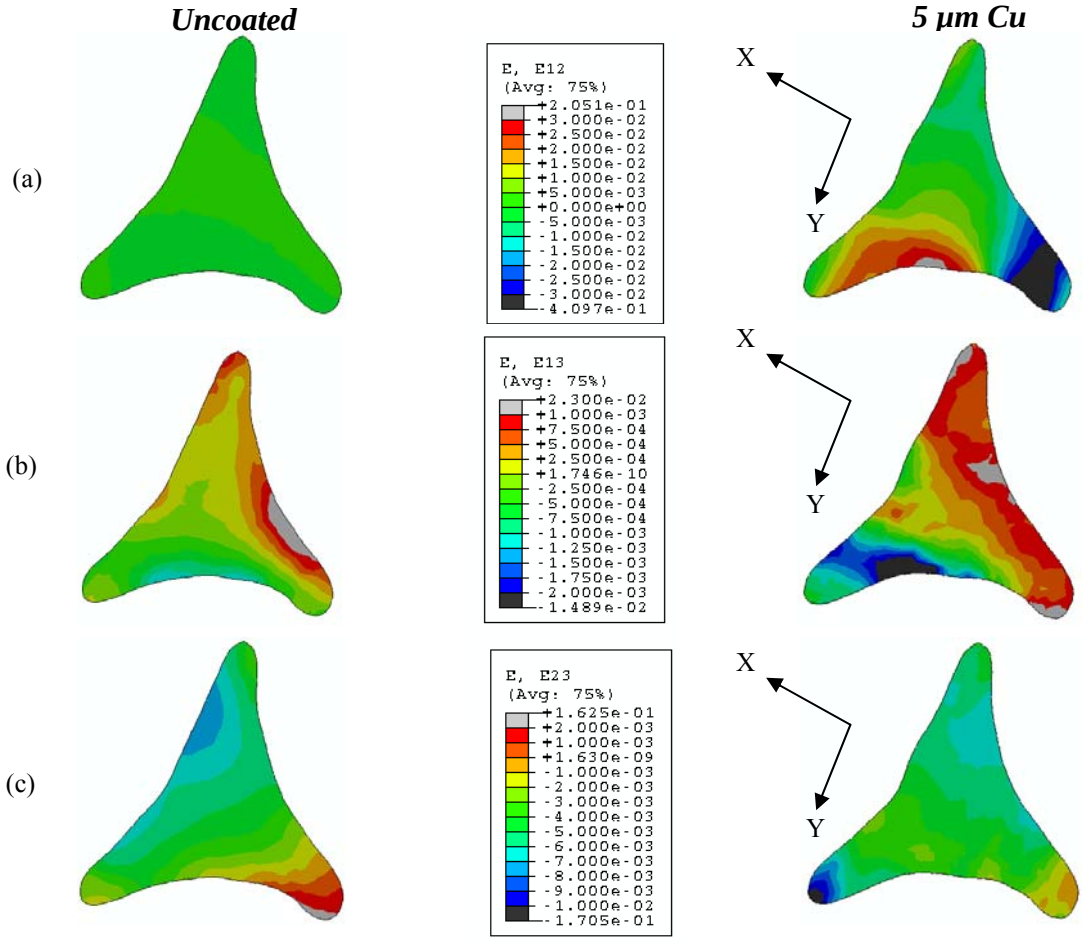

Figure 4.16. Thermal strain components (a) γ_{xy} (b) γ_{xz} and (c) γ_{yz} for both uncoated and Cu coated ligaments at 1300 ºK

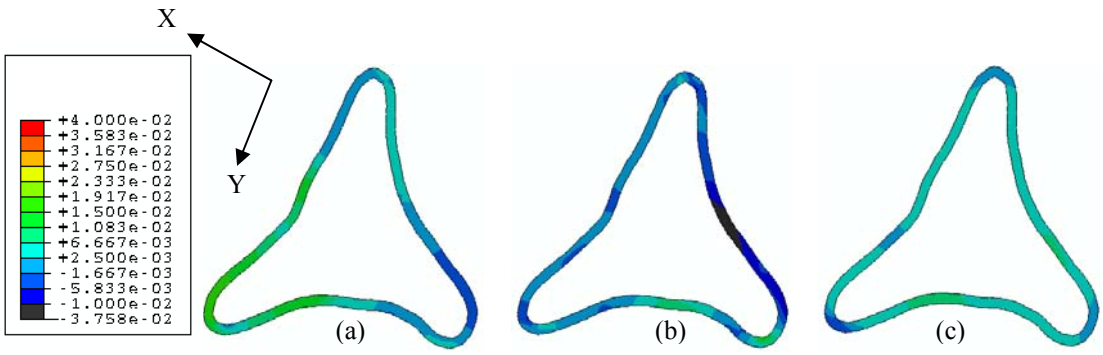

Figure 4.17. Thermal strain components (a) γ_{xy} (b) γ_{xz} and (c) γ_{yz} for coating layer in Cu coated ligament at 1300 ºK

The impact of the polymer, PLLA, coating is not expected to be as influential on the thermal strain and stresses since the temperature range under consideration is an order less than that of copper coatings. Furthermore, the discrepancy in CTE value between the polymer and carbon foam is less resulting in less thermal strain. This is confirmed by the normal strain plots shown in Figure 4.18, where the coating layer is removed for visualization. In the contour plots, two of the components are similar indicating that the influence of the coating on the carbon foam strain values is minimal. The exception is normal strain ε_{yy} which represents the largest CTE value in the anisotropic carbon foam ligament property. Furthermore, the normal strains in the coating layers are a similar order of magnitude compared to the foam as shown in Figure 4.19.

The impact of the PLLA coating on the shear strains is also reduced from the case with copper coating as shown in Figure 4.20. The magnitude of the shear strains closely resembles that of the normal strain components. As in the case of copper coatings, these shear strains indicate a twisting of the carbon foam ligament and further support the displacement plots findings. Furthermore, the PLLA coating is undergoing less thermal shear strains than the copper coating case as shown in Figure 4.21 due to its lower CTE property.

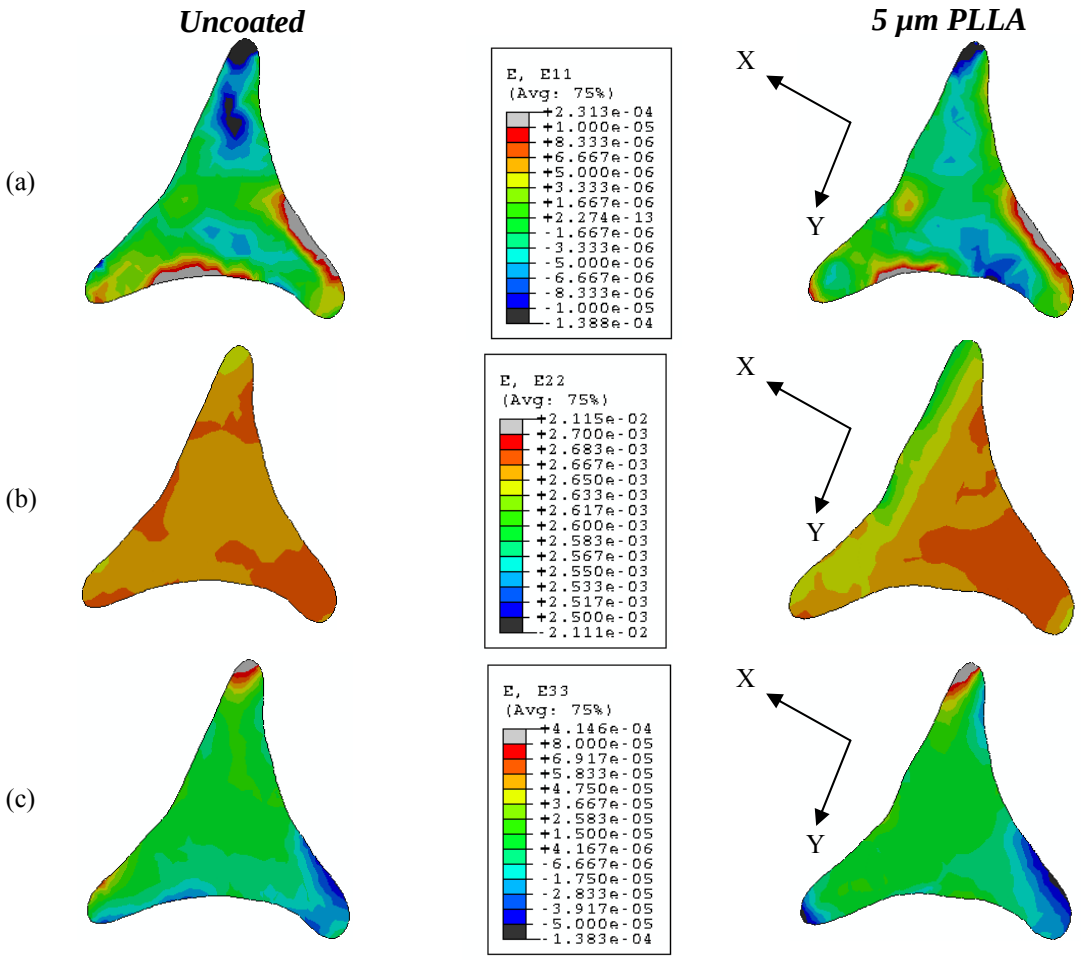

Figure 4.18. Thermal strain components (a) ε_{xx} (b) ε_{yy} and (c) ε_{zz} for both uncoated and PLLA coated ligaments at 400 ºK

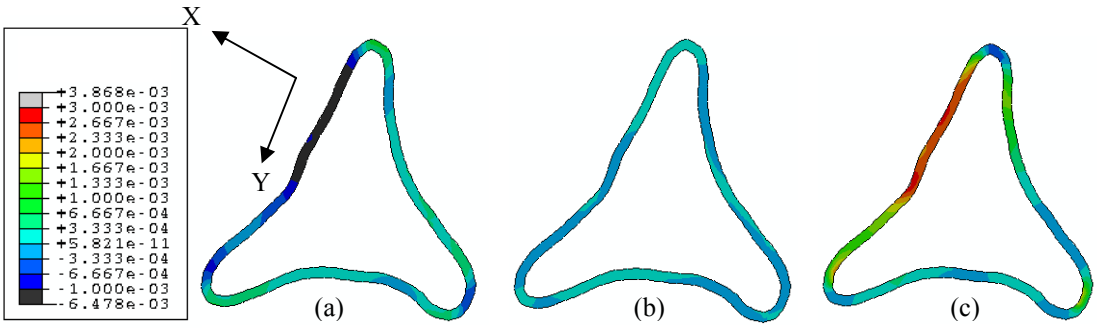

Figure 4.19. Thermal strain components (a) ε_{xx} (b) ε_{yy} and (c) ε_{zz} for coating layer in PLLA coated ligament at 400 ºK

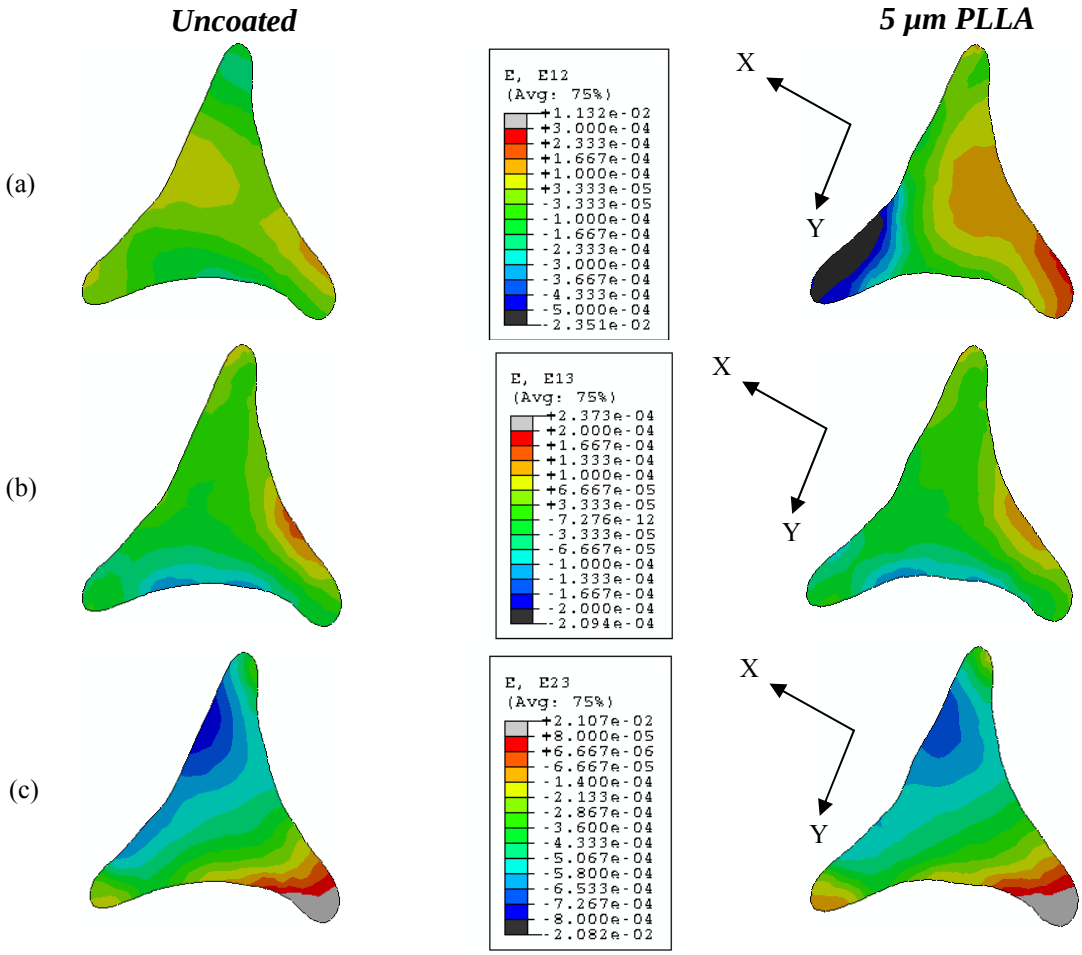

Figure 4.20. Thermal strain components (a) γ_{xy} (b) γ_{xz} and (c) γ_{yz} for both uncoated and PLLA coated ligaments at 400 ºK

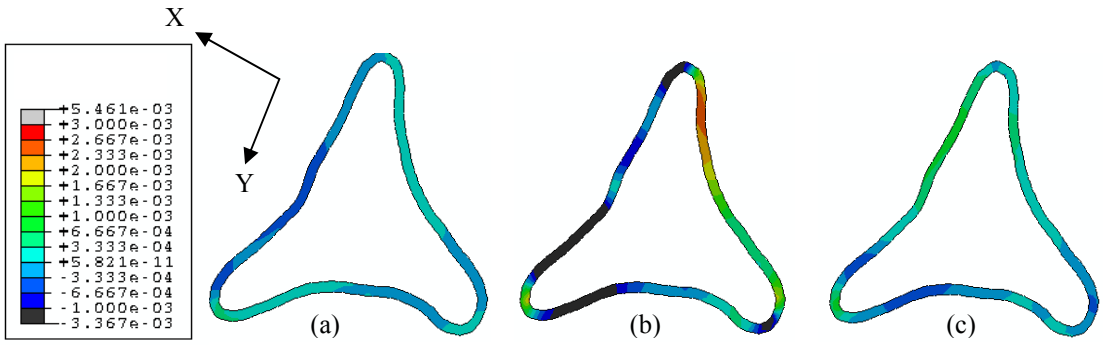

Figure 4.21. Thermal strain components (a) γ_{xy} (b) γ_{xz} and (c) γ_{yz} for coating layer in PLLA coated ligament at 400 ºK

After identifying the impact of the coatings on thermal strain components, a final study is undertaken to determine the influence of temperature and coating composition on the interfacial stresses. In order to eliminate boundary effects near the host boxes, the area of interest identified in Figure 4.3 is used to calculate statistical parameters for the three cases. Initially, all cases—uncoated, copper coated and PLLA coated—are compared at the maximum temperature considered for the polymer coating case of 400 ºK. The average von Mises stress is plotted as a function of temperature in Figure 4.22 for the interface nodes in identified area of interest. The polymer interface region is nearly identical to the uncoated carbon foam ligament case. This indicates that the PLLA coating has negligible effects on the interface region as a result of a decreased CTE mismatch. Conversely, when the ligament is coated with copper, the mismatch in CTE is larger as the interface undergoes a higher stress level.

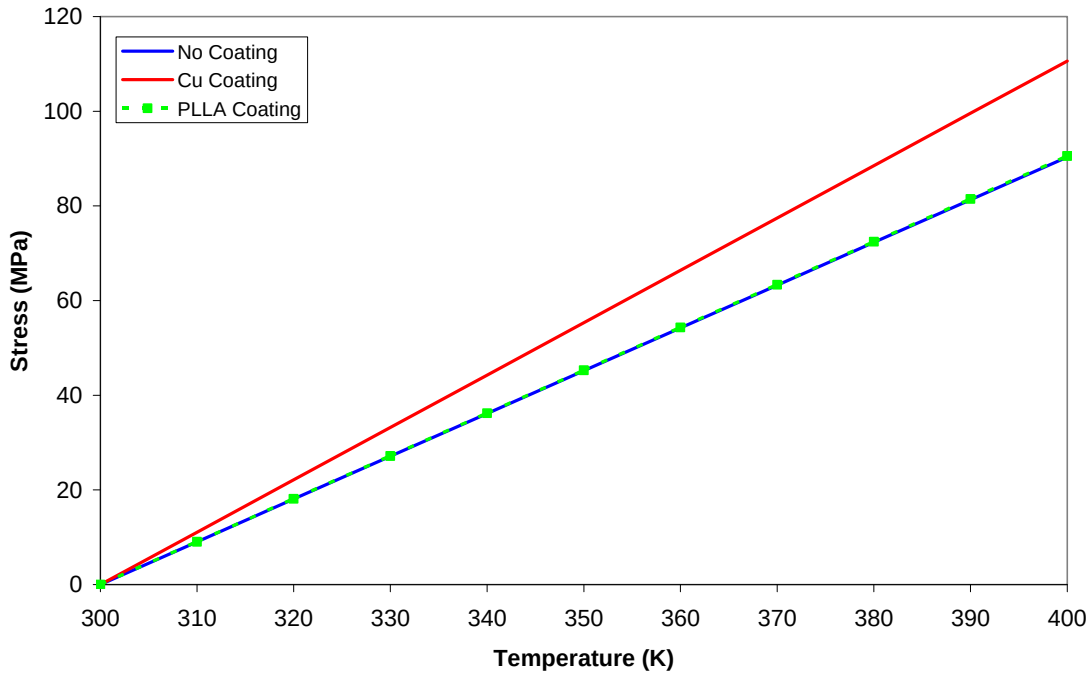

Figure 4.22. Mean stress (von Mises) as a function of temperature for the interface region up to 400 ºK

The impact of the copper coating continues to increase in influence as the temperature is increased to the maximum considered temperature of 1300 ºK. In addition to altering the average interfacial stress, the copper coating also affects the maximum von Mises stress in this identified region as shown in Figure 4.23. Notice that although copper coatings increase the average stress at the interface, they also decrease the overall maximum stress at the carbon foam ligament surface and act to reduce stress concentrations from surface irregularities.

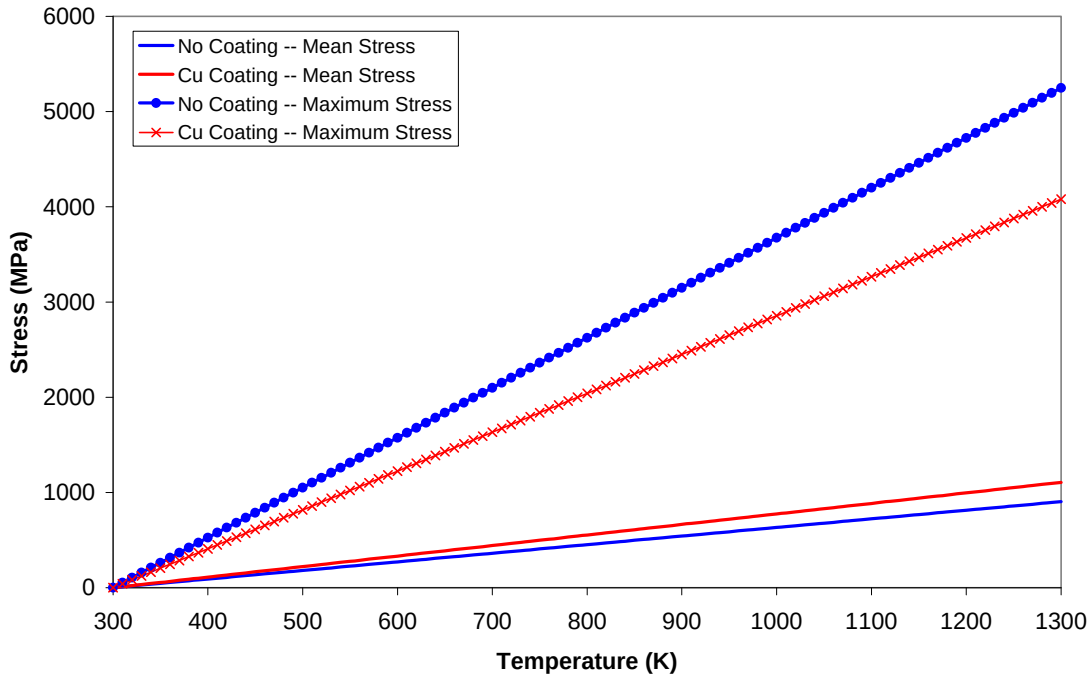

Figure 4.23. Stress (von Mises) as a function of temperature for the interface region up to 1300 ºK for the uncoated and copper coated ligaments

4.2.3. Observations

Two coatings, copper and PLLA, are identified and applied to the single ligament VOI to support ongoing research efforts with the objective of understanding how coatings impact the thermal deformation under a uniform temperature.

In the case of copper coatings, the deformation mode is similar to that of the uncoated ligament; however, when comparing the thermal strains notable differences are established. Due to a large CTE relative to the carbon foam, the copper layer is expanding and deforming more than the carbon foam, thus influencing the response of the ligament. Furthermore, when considering the interface region between the foam substrate and copper coating, the thermal expansion of the copper layer induces large strains at the interface. Although copper coatings increase the average stress at the interface, it is noted that the maximum stress in this region decreases when coatings are applied suggesting a reduction in stress concentrations due to irregular surface geometry.

In the case of the polymer coating, the influence on strains and stresses is reduced indicating that the carbon foam is driving the thermo-mechanical response of the coated ligament. This result is expected due to the similar nature of the CTE values between the PLLA and carbon foam ligament.

The CTE value of any applied coating with respect to the ligament property is important in applications with thermal loading. For small CTE mismatch, the stiff carbon foam ligament drives the overall deformation of the system as in the case of the polymer coating. However, for the larger CTE mismatch, the coating influences the stress and strain states inside the carbon foam ligaments, as well as at the interface region. Furthermore, if copper is used as a coating for high temperature applications, processing researchers should work to ensure a quality bond at the interface in order to withstand large interfacial stress levels.

5. SINGLE ENCLOSED CAVITY VOI STUDY

The single enclosed cavity is selected as the intermediate geometric scale VOI as shown in Figure 5.1 with each individual ligament identified with a different color. At this scale, the connectivity of 74 ligaments is studied to assess load transfer within the structure. In addition, further examination of the processing defects such as globules and irregular surface features is conducted. As with the previous scale, the objective is to evaluate the impact of ligament anisotropy and coatings or infiltration on the mechanical, thermal and electric response of multi-functional carbon foams.

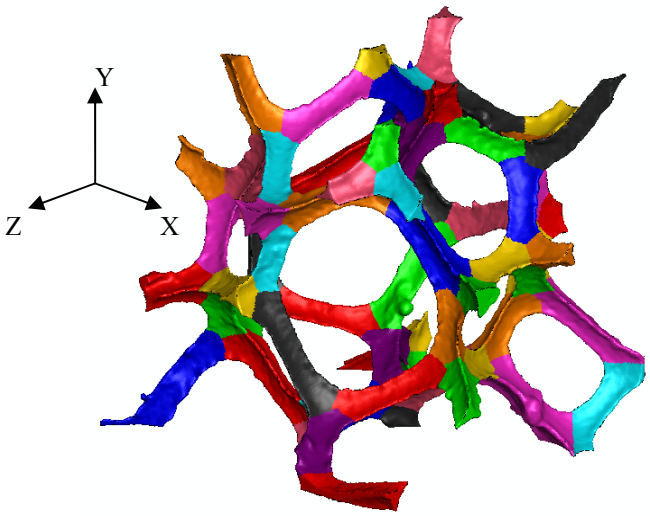

Figure 5.1. Single enclosed cavity VOI with individual ligaments identified

5.1. Effect of Ligament Anisotropy on Mechanical Deformation

5.1.1. Problem Description

In this study, the orientation of the anisotropic properties is altered to determine the impact on overall effective stiffness of the structure. The objective is to understand how the various moduli contribute to the overall deformation of the single enclosed cavity VOI when subjected to compressive loads. The three orientation cases considered are depicted in Figure 5.2 for an idealized ligament and represent a longitudinally stiff, medium stiff and compliant ligament. Changes to the longitudinal stiffness value impact the stiffness values transverse to the ligament axis, thus influencing the bending deflection of individual ligaments.

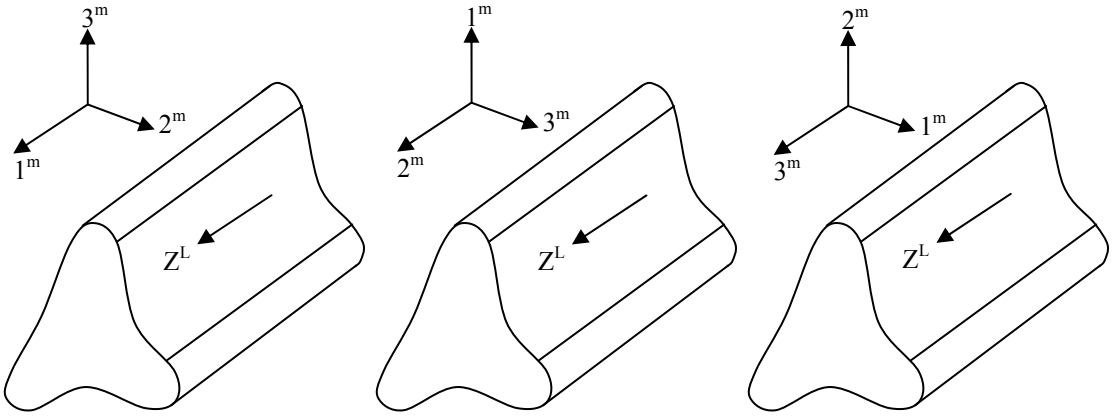

(a) (b) (c)

Figure 5.2. Orientations of anisotropic material properties on idealized ligament for longitudinally (a) medium (b) compliant and (c) stiff ligaments

The single enclosed cavity VOI contains 74 individual ligaments and consequently there are 74 material orientation coordinates contained in the model; the systems are consistent in aligning the specified material coordinate (1^m, 2^m or 3^m) with the ligament axis (Z^L) for the anisotropic C_{ij} matrix for a zig-zag material structure. When considering the entire volume, there are approximately 25 ligaments reasonably aligned with the identified loading direction (global Y) as previously described. These aligned ligaments, as identified in Figure 5.3, represent approximately 36% of the solid volume in the single enclosed cavity structure.

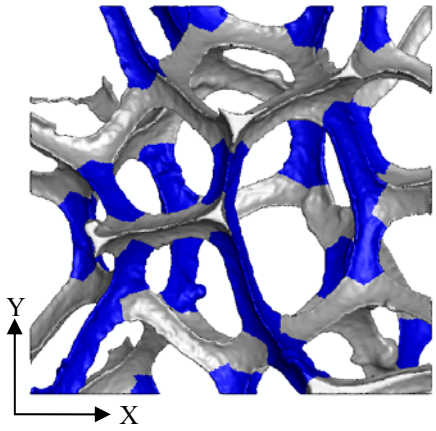

Figure 5.3. Ligaments aligned with the compressive loading direction

5.1.2. Results

The first orientation considered aligns the material 3^m direction with the ligament axis Z^L representing the highest longitudinal stiffness possible for the anisotropic zig-zag properties. The second orientation has a 40% smaller longitudinal stiffness for each ligament representing a medium stiff ligament. The final orientation describes the most compliant ligaments from a longitudinal standpoint and is 96% less stiff than the first

case. However, in this orientation the transverse stiffness relative to the ligament axis is the largest among the three cases thus influencing bending and rotational deformation.

In order to quantitatively compare these three cases, an effective modulus in the loading direction is identified by considering the stress and strain components, and the resulting strain energy density. Details of this procedure are outlined in Appendix C. Since a single loading direction is considered due to consistency in ligament connectivity in this model, only a single effective modulus for the VOI is calculated and information regarding bulk stiffness in other directions must be identified through separate analyses.

As expected, the stiffest longitudinal ligaments—orientation case $3^m \equiv Z^L$—results in the stiffest bulk modulus in the loading direction as shown in Table 5.1. In addition, the second stiffest orientation case, $1^m \equiv Z^L$, is slightly more compliant, while the most compliant ligaments in the longitudinal direction, $2^m \equiv Z^L$, result in the lowest bulk effective modulus in the Y direction.

Table 5.1. Effective modulus in the loading direction for the three orientation cases

		$1^m \equiv Z^L$	$2^m \equiv Z^L$	$3^m \equiv Z^L$	
Effective Modulus	E_y	265	*99*	290	***MPa***
Ligament Longitudinal Stiffness	C_{ij}	626	*41*	1050	***GPa***

Since the displacement condition applied on the top surface through a set of host elements is consistent among the three orientation cases, the deformation plots are examined to qualitatively identify changes in deformation in the plane normal to the loading direction. Observations reveal that the spherical cavity expands in the radial direction perpendicular to the loading direction similar to the illustration in Figure 5.4. This is further examined through inspection of the displacement component contours.

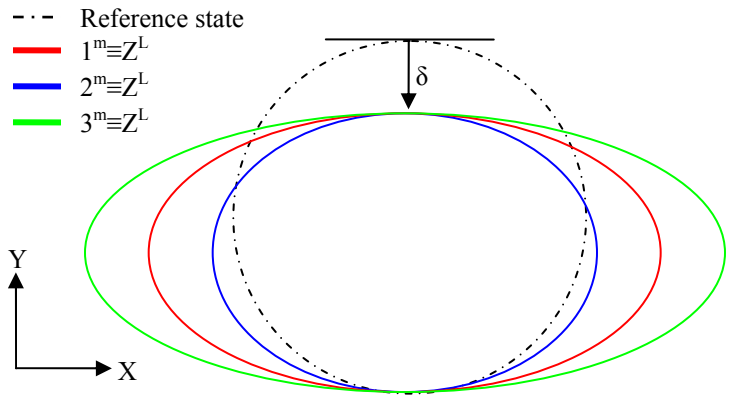

Figure 5.4. Deformation of the single enclosed cavity from compressive loading for the three orientations of anisotropic properties

The compressive boundary condition is consistent among the three cases, thus the displacement component in this direction (u_y) shows negligible changes as the orientation is altered; however, the other two components show more significant differences in deformation with orientation changes. In both the Y and Z displacement components, the stiffest longitudinal ligament deforms most, followed closely by the medium stiff orientation. It is noted that the most compliant ligament longitudinally results in the highest bulk stiffness in this transverse direction. This behavior is attributed to the stiff transverse moduli in this case which inhibit bending and rotation about the ligament axis.

In addition to identifying the effect of orientation on overall deformation of the structure, this geometric scale is also used to identify the impact of processing defects on the stress and strain results. Focusing on a single orientation case ($3^m \equiv Z^L$), several ligaments displaying characteristic defects are identified for further examination.

The first surface defect examined is a large globular feature located along the ridges of various ligaments as illustrated in Figure 5.5. In some cases, during the thermodynamic

foaming process a bubble starts to grow but only partially forms leaving an artifact in the final foam morphology. Two ligaments in the single enclosed cavity VOI are identified as having this characteristic defect and both are investigated for stress concentrations.

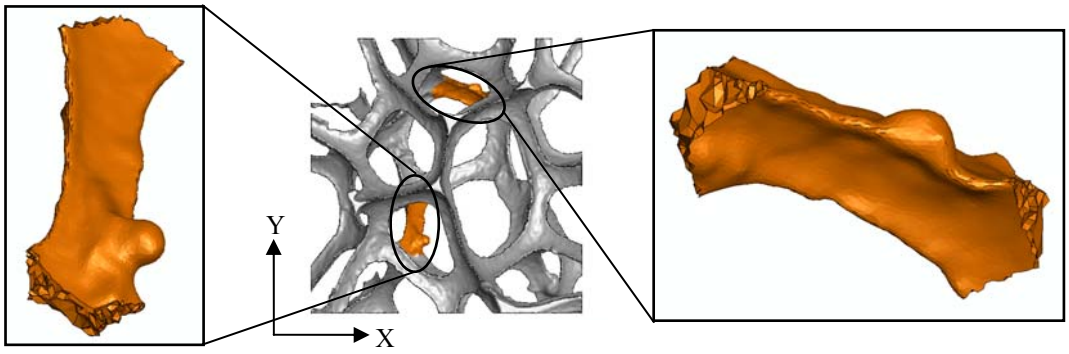

(a) (b)

Figure 5.5. Single enclosed cavity (a) Ligament 37 and (b) Ligament 73 with characteristic globular feature

Ligament 37 is oriented parallel with the loading direction (global Y) and is dominated by a compressive stress along its ligament axis is two orders of magnitude higher than the other stress components. The globular feature on this ligament is located near the end of the ligament and is centered on an edge ridge as shown in Figure 5.5. A progressive illustration of how the ligament cross section changes along its length is depicted in Figure 5.6. The feature is characterized by a smooth transition to the surrounding area and serves to elongate that region of the cross section reducing the triangular symmetry. Examination of the other stress components shows little impact of this feature on overall stress magnitudes when compared with similarly oriented ligaments without a globular irregularity. Furthermore, this feature does not appear to act as a stress riser, but more mesh refinement is needed to confirm this finding. It is of note that a large tensile stress appears on the ligament face opposite the feature;

however, it is not conclusively traced to the feature but rather is likely driven by the transition of this ligament into the thicker nodal region, a phenomenon seen for ligaments containing no defects.

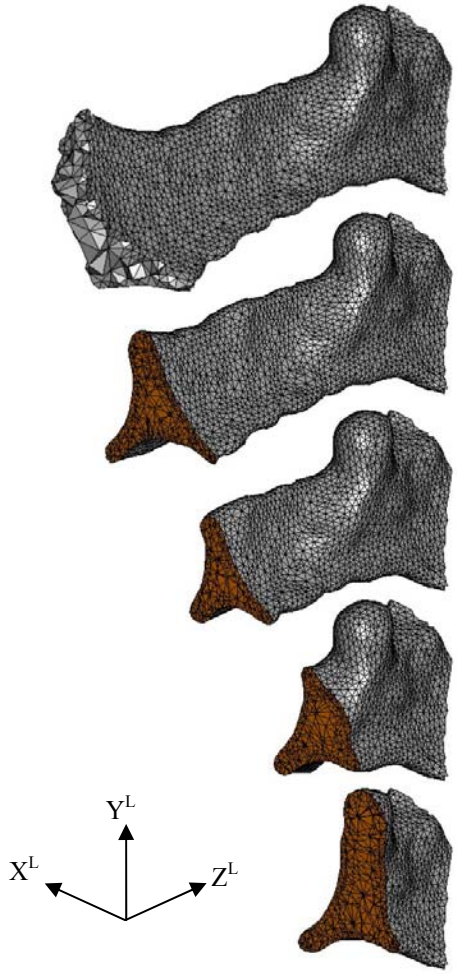

Figure 5.6. Cross sectional profiles at various locations along Ligament 37

The second ligament exhibiting a globular feature is Ligament 73 in Figure 5.5. This ligament is oriented perpendicular to the loading direction and undergoes a bending deformation mode. This is evidenced by a typical bending stress contour with the top of

the ligament undergoing tension while the opposite side is under compression as shown in Figure 5.7. The cross sectional changes approaching the globular features are similar to that of the preceding ligament with asymmetry in the area of the defect. However, in this ligament the resulting stress contours in the area are influenced by this feature. Investigation of the normal stress along the ligament axis shows that the globular feature disrupts the tensile/compressive pattern preceding and following the defect. The globular defect itself undergoes a complex stress state with parts in tension while others are in compression. However the stress magnitudes in this region are an order of magnitude less than in other regions of the same ligament indicating that such features do no act as stress concentration points.

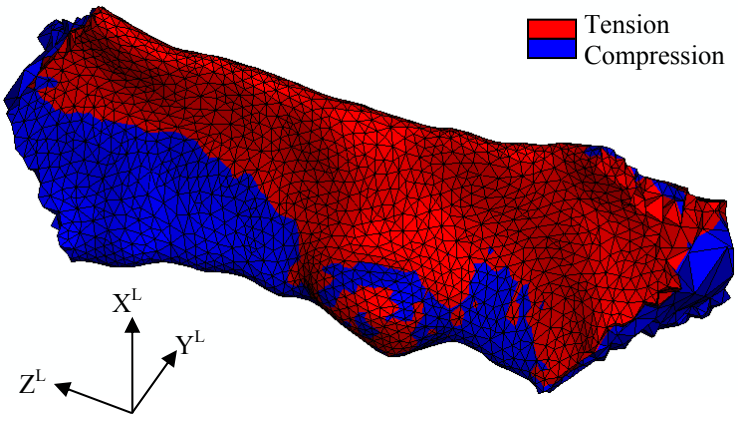

Figure 5.7. Bending stresses (σ_{zz}) for Ligament 73 in material coordinates

In addition to globular features along the ridges of the ligaments, other irregular bumps appear along the faces of the ligament as shown in Figure 5.8. These features are characterized by a surface disturbance and are caused by undeveloped bubble formation similar to the larger globular features discussed previously. Ligament 65 is identified as having several of these surface projections. The stress state in this ligament is

dominated by the normal stress in the direction of the ligament axis. Inspection of this stress component contour shows that the surface features are characterized as lower stress areas, up to one order of magnitude. In addition, these features appear to influence the overall stress contour patterns when compared to similarly oriented ligaments elsewhere in the single enclosed cavity VOI model.

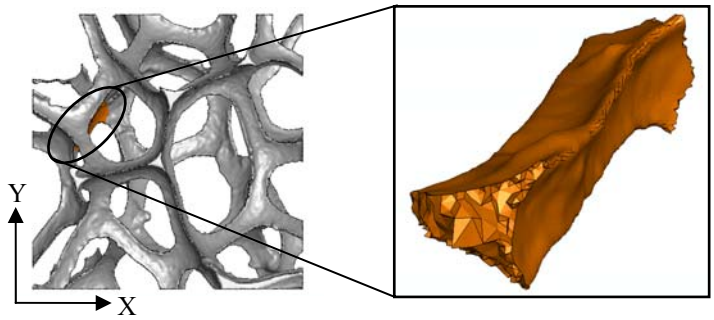

Figure 5.8. Single enclosed cavity Ligament 65 with characteristic surface projections

The final defect investigated is a saw tooth pattern shown in Figure 5.9. The origin of this type of defect is molecular weight changes during heat treatment procedures. As the structure cools, the foam volume constricts and shrinks causing small cracks including these saw tooth artifacts. In Ligament 66, the largest stress component is the bending stress component along the ligament axis. In addition, examination of the regions directly below the saw tooth area show a significant stress concentration developing up to two orders of magnitude higher than in areas removed from the defect. Recall that the smoothing algorithms used in meshing procedures are not designed to preserve sharp features; therefore this defect is likely more jagged in actual carbon foams and could have even more impact on stress concentrations.

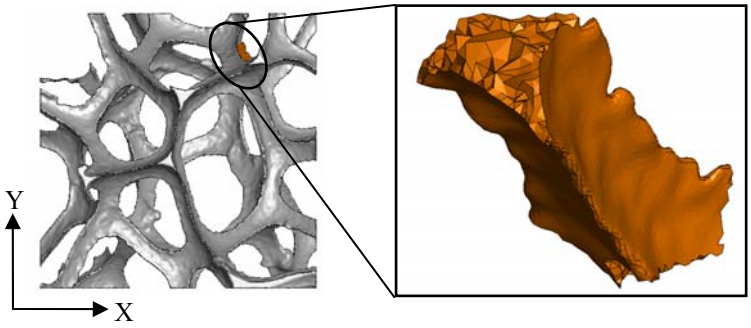

Figure 5.9. Single enclosed cavity Ligament 66 with characteristic saw tooth feature

5.1.3. Observations

In order to tailor carbon foam to attain high stiffness in a single loading direction, it is beneficial for processing researchers to increase the longitudinal modulus of individual ligaments as in the case of the $3^m \equiv Z^L$ orientation. This orientation reflects a structure in which the graphene planes are aligned with the ligament axis. However, if the application loading conditions are complex, additional effort is needed to ensure that the transverse ligament properties are sufficiently stiff to limit bending deformation. In addition to controlling ligament anisotropic properties and orientations, further improvement in effective stiffness is obtained by aligning more ligaments with the direction of loading. This is achievable through processing variable selection (pressure, temperature, blowing agent, et cetera) to produce a specific morphology based on pore growth during the liquid foaming process.

Furthermore, three classifications of defects are studied including globular features along ligament edges, surface projections along ligament faces and saw tooth patterns also along ligament edges. For each feature, changes to the overall stress contour patterns are identified in the area near the imperfection. Moreover, the smoother defects (globules and surface projections) appear to reduce stress levels in these areas compared with

similar locations on other ligaments not impacted by defects. Conversely, the sharper saw tooth defect appears to increase stress directly below the feature and could act as crack initiation points in the carbon foams. Processing research should strive to use high quality precursor materials and avoid introducing impurities during the foaming process in order to produce strong carbon foams. In addition, more processing research is required to identify and minimize the impact of volume shrinkage after heat treatment procedures to prevent cracking and other artifacts.

5.2. Effect of Polymer Infiltration on Mechanical Stiffness

5.2.1. Problem Description

Additional studies are undertaken to understand the influence of complete infiltration on the mechanical stiffness of anisotropic carbon foams. In order to support recent research into orthopedic biomedical devices incorporating carbon foam, this investigation uses a bioresorbable polymer, poly(l-lactic acid), or PLLA to infiltrate the carbon foam structure [32]. Current orthopedic device materials such as titanium are several orders of magnitude stiffer that natural bone material. This mismatch has consequences on the healing of the fracture resulting in a weaker region of bone after healing. Furthermore, doctors often surgically remove these devices after the fracture has healed partially in order to prevent the stress shielding effect. Therefore, the objective of this illustration is to obtain an effective modulus close to that of natural bone (12-18 GPa) through infiltration of the carbon foam with the bioresorbable polymer.

Initial research into biomedical devices indicates that although longitudinal stiffness in the direction of the bone is important, bending stiffness is also critical for supporting the bone's fracture zone [32]. At this VOI scale, it is difficult to identify bending stiffness therefore the focus of this study is on obtaining the highest stiffness in the loading

direction. As such, the ligament anisotropy orientation $3^m \equiv Z^L$ is chosen for application to this problem with relevant properties shown in Table 3.4. The bioresorbable polymer, PLLA, properties can be found in Section 3.5.2 and Table 3.9.

The single enclosed cavity pore space is meshed according to the procedure described in Section 3.1.2 using an advancing front scheme. This procedure results in the pore space mesh consisting of 7,441,849 linear tetrahedral elements. The polymer phase is perfectly bonded to the carbon foam substrate. Recall that the porosity of this VOI is 96% thus the carbon foam acts as a reinforcing agent for the polymer similar to the role of carbon fibers in a composite laminate. The infiltrated and carbon foam substrate is shown through various cross sections along the global Z dimension in Figure 5.10.

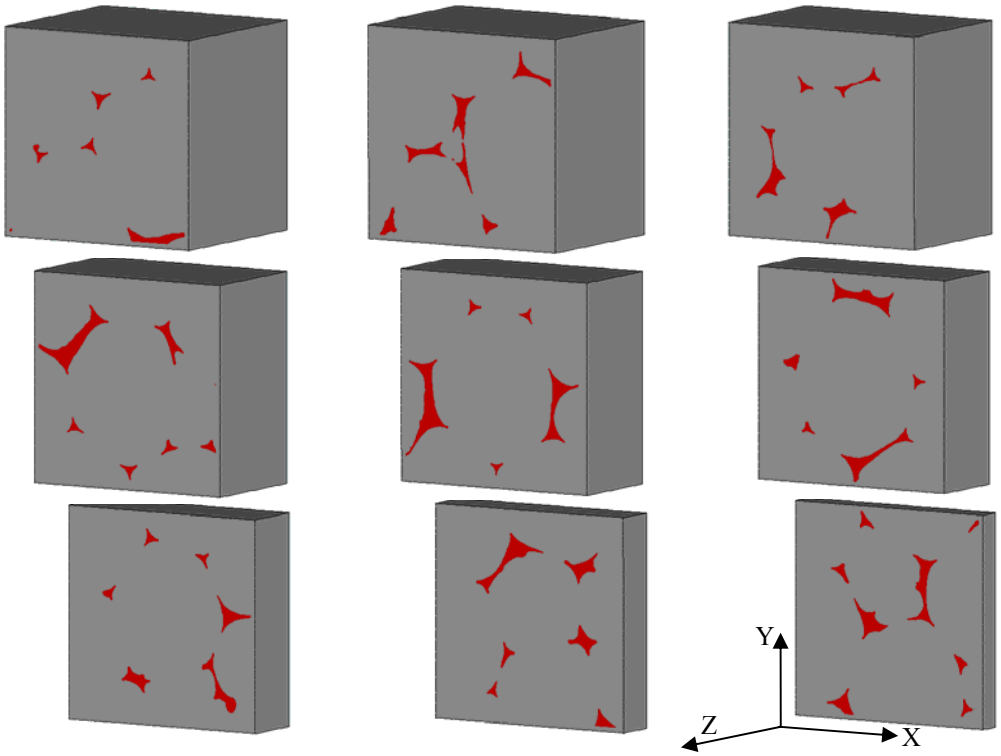

Figure 5.10. Cross section profiles at Z locations in PLLA infiltrated carbon foam VOI

5.2.2. Results

Since the carbon foam represents a very small part of the total volume in this VOI, it is expected that the infiltration will significantly impact the overall effective property. Using the procedure outlined in Appendix C based on strain energy density, the effective property for the infiltrated VOI is calculated as 2,609 MPa in the loading direction. This represents a 125% increase over the modulus of the infiltration polymer PLLA of 1,150 MPa suggesting that the carbon foam structure is reinforcing the polymer as in traditional fiber composites.

In addition to identifying effective bulk stiffness for an infiltrated carbon foam, further investigation is undertaken to characterize the impact of the infiltration on stress, strain and displacement behavior. Individual ligaments in the carbon foam structure displace less than their counterparts in uninfiltrated carbon foam from the previous illustration. This effect is especially prevalent in the bending deformation suggesting that the polymer constrains the ligaments contributing to the increased bulk effective stiffness in direction other than the loading direction.

Confirmation of this constraint effect is evident in the stress and strain plots for the infiltrated carbon foam system. In the case of strain components, the foam elements have a reduced magnitude compared to the respective elements in the uninfiltrated carbon foam. In addition, the polymer appears to undergo higher strains than the adjacent ligament as expected due to its lower modulus enabling more deformation.

Additional information regarding the interaction of the carbon foam ligaments and the surrounding polymer are evident in the stress contour plots. Some example stress plots are shown in Figure 5.11 and Figure 5.12 for a VOI cross section taken at the center of the Z dimension. In each image, the carbon foam ligaments have been removed for visualization purposes and are shown separately in the global coordinate system. At this

cross section, along with other regions of the VOI, stress concentrations develop in the polymer in areas near the ligament ridges. Examination of the stress components in the ligament indicate that these stress concentrations are not directly driven by areas of high stress in the ligament and in some cases correlate with areas of lower stress in the carbon foam.

5.2.3. Observations

Studies at this VOI scale indicate that at small volume fractions, the carbon foam reinforces the polymer; however, it does not meet the stiffness requirements for use as an orthopedic device to stabilize a bone fracture. Furthermore, this illustration focuses on a perfect bond of the infiltration with the carbon foam structure and represents an upper limit on effective stiffness.

Since the carbon foam is significantly stiffer than the polymer infiltration, processing researchers should focus on altering the large volume fraction of PLLA in order to meet design requirements. Methods to increase the constituent stiffness of PLLA are currently being investigated, with hydroxyapatite (HA) additives showing promise in increasing the stiffness of the polymer. If a suitable polymer can not be identified, additional stiffness can be achieved by reducing the porosity of the carbon foam structure; however, complete infiltration may be problematic as the porosity decreases and the structure develops a closed cell nature.

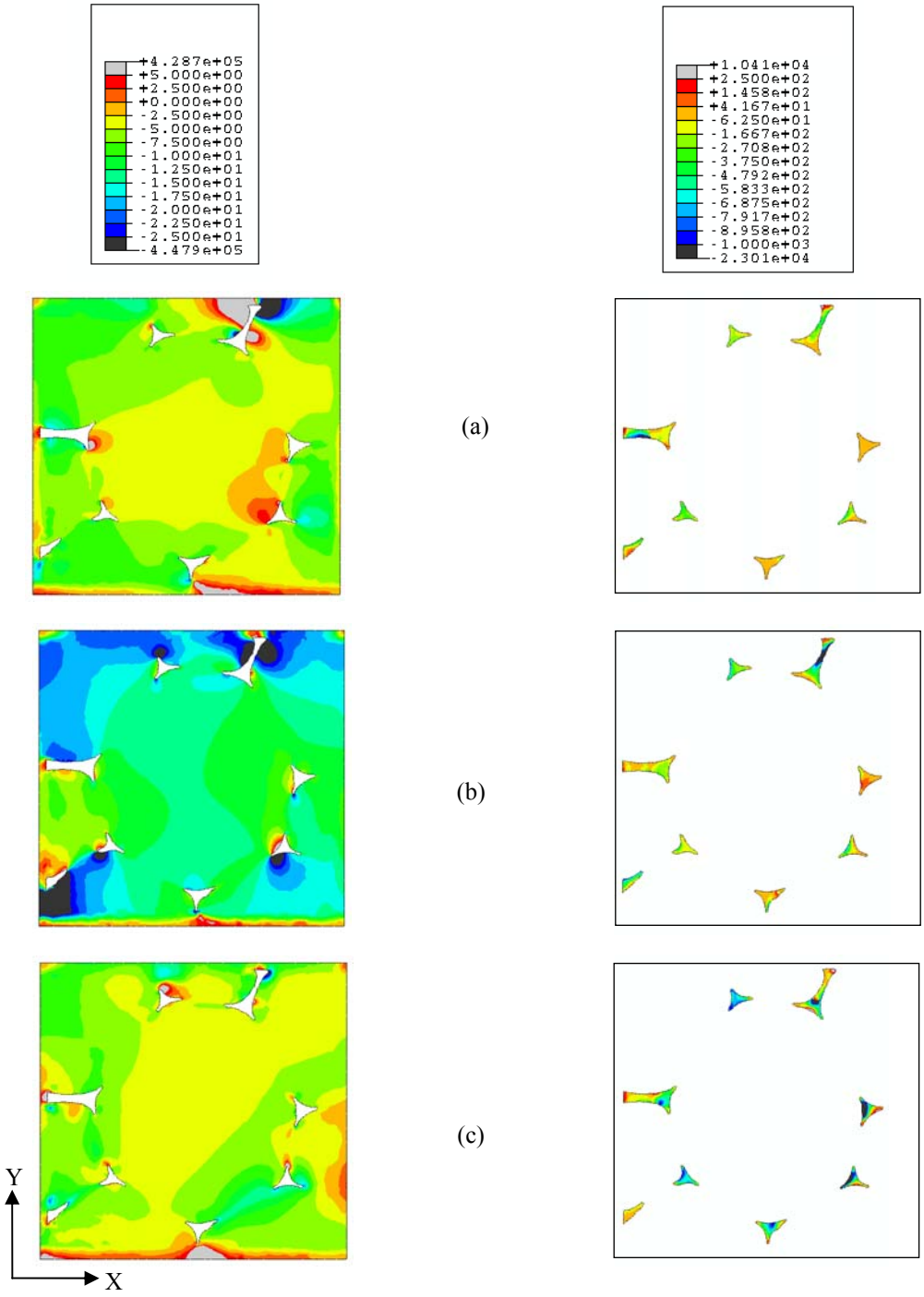

Figure 5.11. Normal stress components (a) σ_{xx} (b) σ_{yy} and (c) σ_{zz} for the PLLA infiltration and carbon foam ligaments in a representative cross section

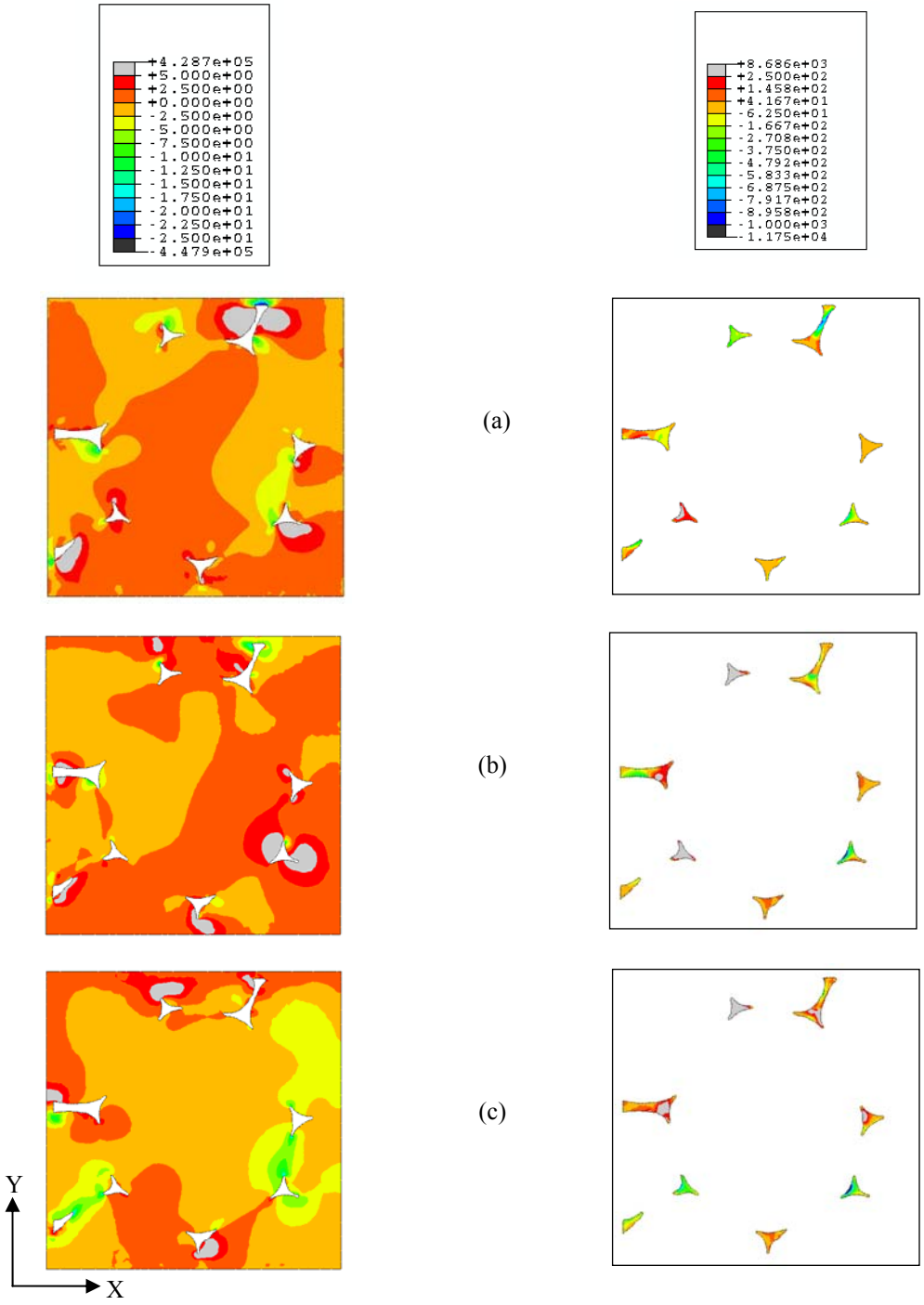

Figure 5.12. Shear stress components (a) τ_{xy} (b) τ_{xz} and (c) τ_{yz} for the PLLA infiltration and carbon foam ligaments in a representative cross section

5.3. Effect of Imperfect Coating on Thermal Conductivity

5.3.1. Problem Description

In carbon foams produced from mesophase pitch precursors, high thermal conductivities are achieved by subjecting the foams to post-foaming heat treatments for graphitization. However, in foams generated from alternate precursors, including coal or polymers, graphitization is not possible and these foams remain insulative in nature. Although for applications requiring thermal conductivity performance the graphitized carbon foams are preferred, some applications may demand insulating foams for economical, manufacturing or other characteristics. In order to tailor the thermal properties of these foams for multi-functional applications, thin metallic coatings are applied to insulative carbon foam to demonstrate improved thermal conductivity. The relevant thermal properties used in this analysis are stated in Table 3.9 for the insulating RVC type carbon foam and the copper coating.

Initial studies focus on assessing experimental reports indicating that thin (2-3 μm) copper coatings improve bulk thermal conductivities up to 2 or 3 orders of magnitude [85]. On the single enclosed cavity VOI, a coating is swept from the foam surface as described in Section 3.1.2. The coating is composed of two layers for a total uniform thickness of 10 μm perfectly bonded to the foam surface and represents a volume fraction of 0.02. This model is then expanded to study the impact of imperfect coatings on thermal performance. The coating defects are isolated to an area of interest, shown in Figure 5.13, which represents one of several thermal paths between the hot and cold temperature sinks.

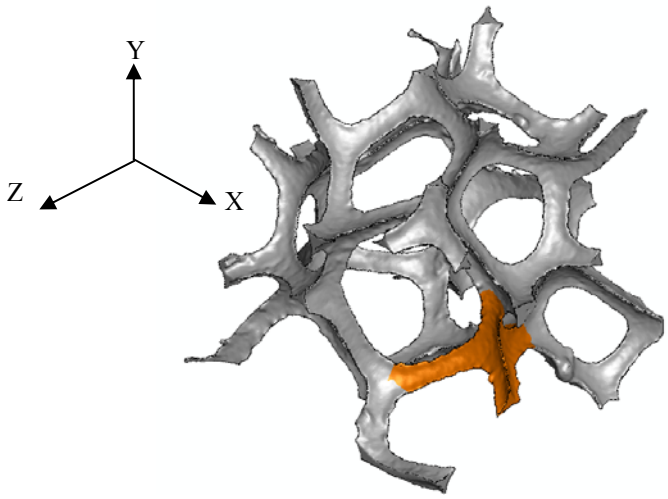

Figure 5.13. Area of interest used to investigate imperfect coating classifications

The first coating imperfection case investigated is a small scale defect around the circumference of a ligament. On one ligament, a 20 µm wide ring of missing coating is modeled by removing both layers of coating. On an adjacent ligament a 20 µm wide ring is debonded from the carbon foam substrate as shown in Figure 5.14, by disconnecting the first layer of coating through duplication of nodes, while the top layer of coating remains fully bonded to the coating before and after the defect. Furthermore, both defects occur on a single thermal dissipation path through the structure.

The second coating imperfection case identified is the case where a large section of coating is missing from a nodal region where four ligaments join as in Figure 5.15. This type of defect has been identified in processed carbon foams where complete coating is difficult if the average cavity dimension falls below 50 µm.

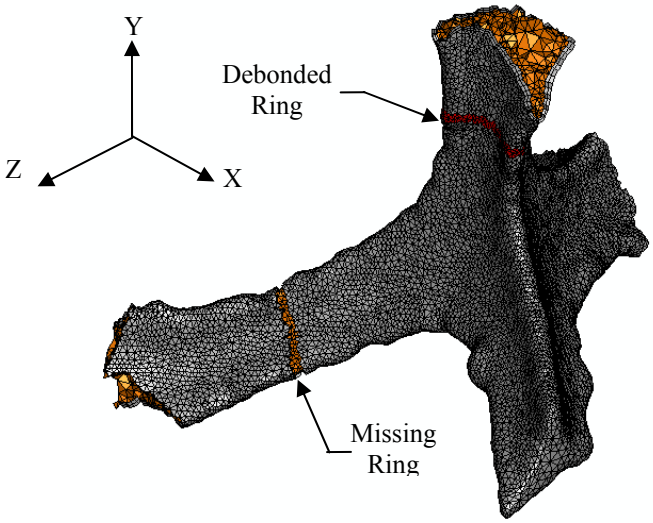

Figure 5.14. Small scale defects including missing and debonded rings of coating

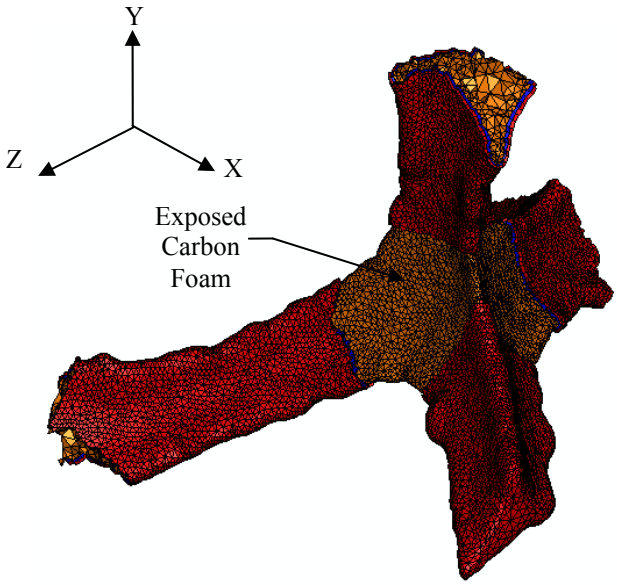

Figure 5.15. Large scale defect consisting of a large area of missing coating

5.3.2. Results

The effective thermal conductivity of insulative carbon foam with a uniform layer of copper is obtained as described in Appendix C. This method is based on the one dimensional form of Fourier's law and results in an effective property characteristic of the thermal gradient in the loading direction.

Since the copper is roughly four orders of magnitude more conductive than the base carbon foam ligament, it is expected to improve thermal conductivity considerably as shown by a rule of mixture estimation using the relative volume fraction of the constituents, 0.03 for foam and 0.02 for copper with the remaining fraction reserved for the empty pore space. The detailed single enclosed cavity VOI model further confirms that thin (10 μm) copper coatings can significantly improve the thermal conductivity of the carbon foam up to 3 orders of magnitude and corroborates experimental findings.

Additional insight into the mechanisms which lead to improved effective thermal conductivity is determined through examination of the heat flux contour plots. In foams with perfectly bonded 10 μm copper coatings applied, the majority of the heat flux is carried through the coating layers with a four order of magnitude increase in magnitude over uncoated foam as show in Figure 5.16. In addition, the thermal dissipation paths in Figure 5.17 are identified for this VOI scale with the preferred path composed of the aligned ligaments from Figure 5.3 for both uncoated and copper coated carbon foams.

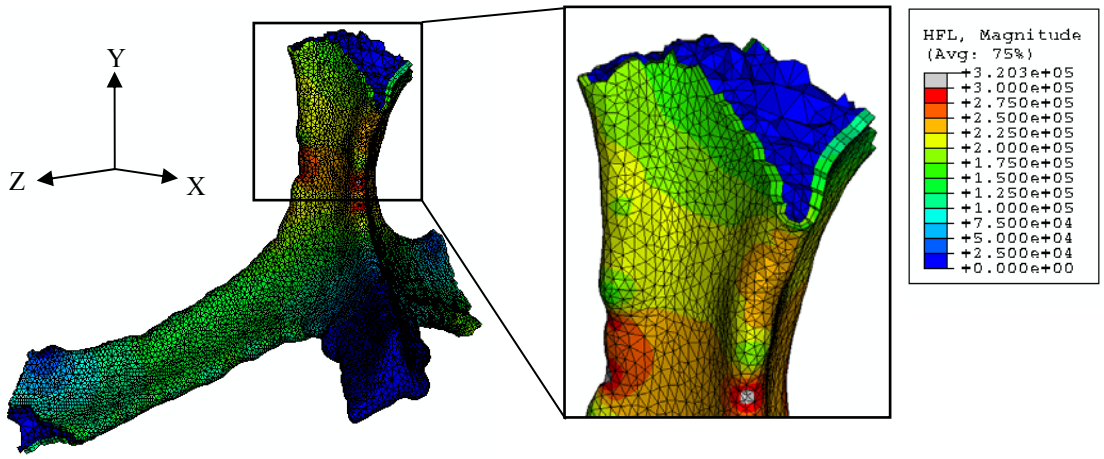

Figure 5.16. Heat flux vector magnitude ($\times 10^{-3}$ W/mm^2) for perfectly bonded Cu coating

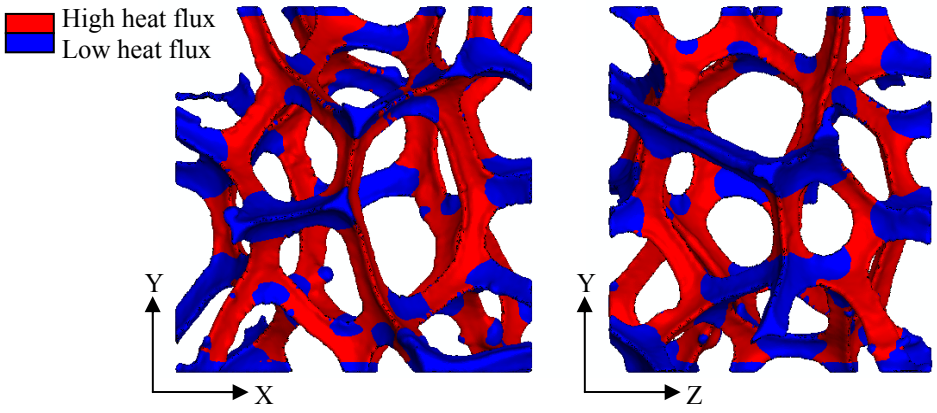

Figure 5.17. Preferred thermal dissipation paths in RVC carbon foams

When the resultant temperature distribution is coupled with the mechanical analysis as described in Section 3.4.2., the uncoated RVC carbon foam undergoes minimal stresses of less than 0.5 MPa. However, when the thin 10 μm copper coating is applied, the resulting deformation due to thermal expansion is more significant as shown in Figure 5.18 at a 10× scale with the nodal temperature (ºK) contours. In Figure 5.18, the front and rear host box faces have been removed for visualization purposes. The largest ligament deformation is confined to the areas of highest temperature while the cooler

areas undergo less movement. Recall that the mechanical boundary conditions for this case stipulate that expansion of the host box faces in the normal direction is fixed.

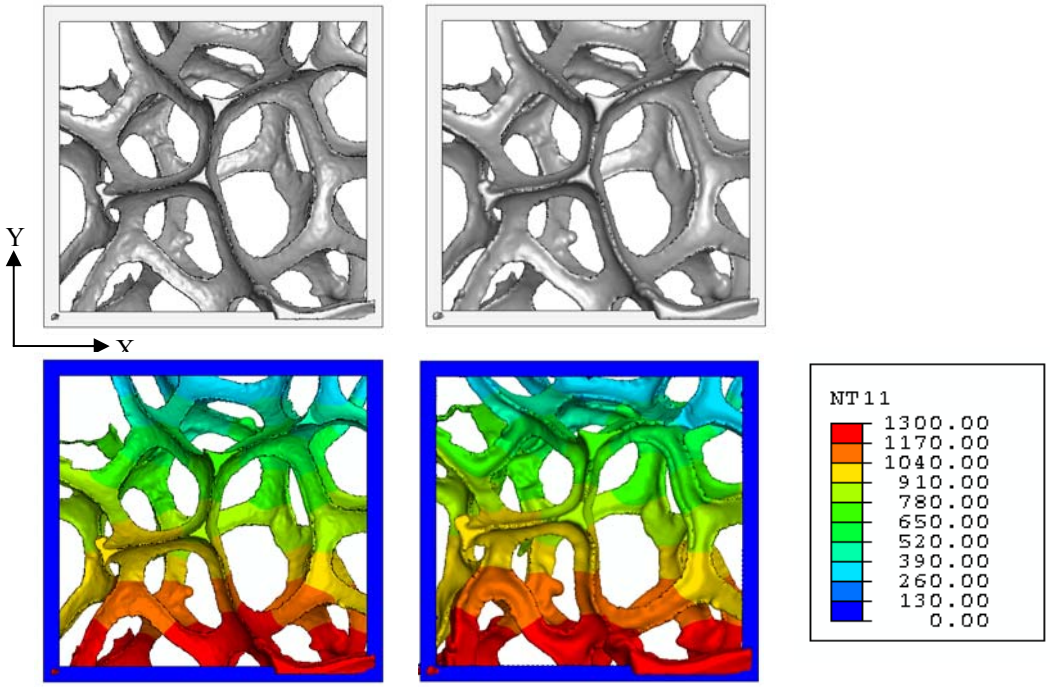

(a) (b)

Figure 5.18. Deformation (10× scale) and reference states for (a) uncoated and (b) perfect Cu coating undergoing thermal expansion

Furthermore, the von Mises stress in carbon foam increases slightly to 10 MPa, while the copper coating stress ranges from 10 to 5,000 MPa. However, the maximum stress values are in areas near stress concentrations such as the transition to a nodal region or localized processing defects, with 90% of the coating undergoing smaller stress levels under 1,000 MPa. Additionally, the von Mises stress at the interface between copper and carbon foam increases an order of magnitude compared to the same area in uncoated carbon foam with a maximum value of 12 MPa.

After successfully confirming experimental findings supporting that thin copper coatings improve thermal conductivity up to 3 orders of magnitude, the impact of common coating imperfections is undertaken. In order to coat the carbon foam with copper, processing researchers deposit a uniform layer of metal using electro-chemistry techniques. Investigation under optical microscopy and SEM show that coatings are fairly uniform in thickness and coverage is near complete for small samples of foam [85]. In large bulk samples, techniques for coating are less refined and defects are more common.

For the small scale defect consisting of a ring of missing coating, heat flux contour plots show that the insulative ligament carries the thermal load across the defect. This effect is shown in Figure 5.19 where the coating layers have been removed for visualization purposes. Although the carbon foam is able to carry some load across the gap in coating, it is not able to fully compensate for the imperfection and the heat flux magnitude is 2 orders of magnitude less in the area following this defect than for the perfect coating case.

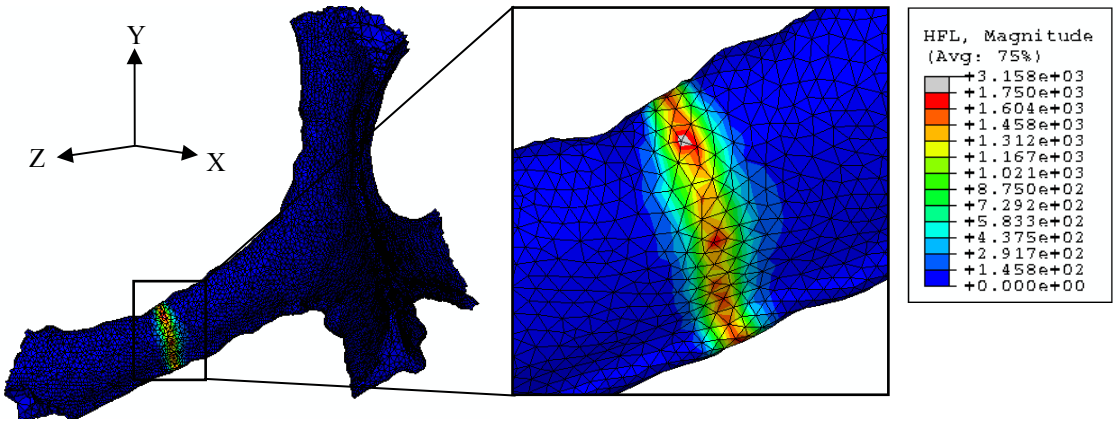

Figure 5.19. Heat flux vector magnitude in foam ($\times 10^{-3}$ W/mm^2) where a ring of coating is missing

Initial examination of the heat flux contours, show little change in magnitude across the debond imperfection. Recall, however, that the two small scale defects are located in close proximity to each other and the first missing ring defect has significantly reduced the heat flux along this thermal dissipation path. Therefore, subtle changes in dissipation are more difficult to identify. Using the method in Appendix C to calculate an effective thermal conductivity, the combined impact of the two small scale coating defects is a 2.5% reduction in effective thermal conductivity in the loading direction compared to the perfect coating case.

In addition to investigating the impact of these small scale defects on the thermal response, additional analyses are performed to identify the resulting thermal expansion stresses. In the area of the missing ring of coating, the changes in the stress counters from the perfect coating case are negligible with the small changes attributed to the lower temperatures following the defect. Examination of the area around the small debonded ring also shows small changes with the area before and after the defect undergoing small decreases in stress. The debonded ring itself appears to have a reduced stress level overall in comparison to the same area in the perfect coating case; however, since the temperature is not uniform between these two cases it is difficult to attribute this change directly to the debond defect.

When a large section of coating is missing around a nodal region, the insulative carbon foam cannot compensate in carrying the heat flux along the thermal dissipation path. Therefore, a large impact on overall temperature distribution is noted as shown in Figure 5.20. This temperature change is attributed to elimination of a thermal dissipation path as evidenced by the heat flux component plots showing that intact paths with perfect coatings carry the extra load. This finding is confirmed by a decreased effective thermal conductivity in the loading direction as shown in Table 5.2 along with the other configurations considered in this illustration.

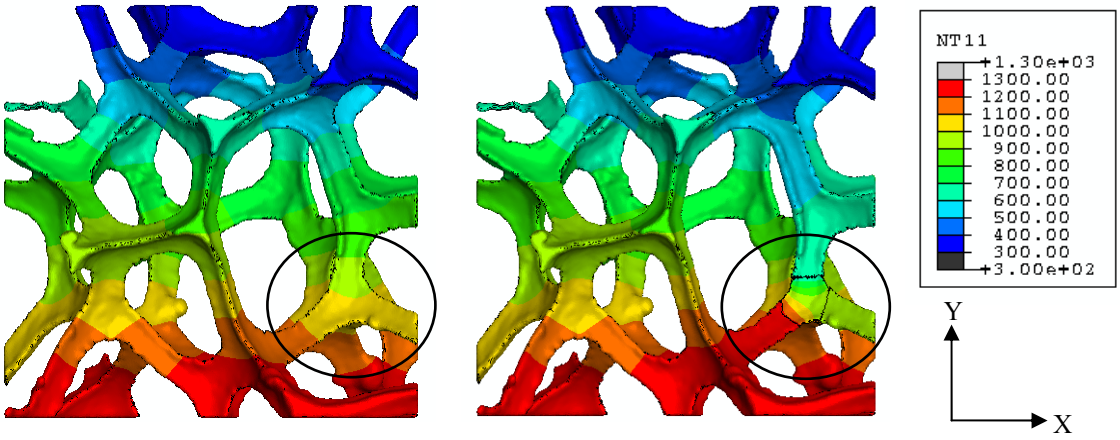

(a) (b)

Figure 5.20. Nodal temperature (ºK) distribution for (a) perfect and (b) missing Cu coating in nodal region

Table 5.2. Effective thermal conductivity in the loading direction for various coating configurations

		Effective Thermal Conductivity ***W/m-K***
Uncoated RVC Carbon Foam	k_y	0.00120
Perfectly Bonded Cu Coating	k_y	3.036
Missing and Debonded Rings of Cu Coating	k_y	2.961
Missing Nodal Region of Cu Coating	k_y	2.745

5.3.3. Observations

In this illustration, the impact on copper coatings on the overall effective thermal conductivity is identified. Initially, uniform perfectly bonded thin 10 μm copper coatings are investigated and this study corroborates experimental findings that thin coatings can improve bulk conductivities up to 3 orders of magnitude. Impact of uniformity of coating thickness was not investigated directly; however, the current

studies suggest a small impact on overall thermal conductivity for non-uniform coatings assuming a minimum thickness is achieved.

The role of missing coating appears to have a large impact on overall effective conductivity for thin copper coated carbon foams. For the small scale defects of missing or debonded rings of coating, the decrease in conductivity was less than 3%. However, for larger defects directly impacting a thermal dissipation path, the overall conductivity decreases up to 10% from a perfect case. This is especially true if the imperfection eliminates a thermal dissipation path as intact paths are not able to fully compensate for the defect. These findings indicate that processing researchers should focus on achieving complete coverage of the insulative carbon foams in order to maximize the effective thermal conductivity.

Additional findings suggest that stresses arising from thermal expansion are significant in the case of copper coated carbon foams. The copper undergoes stress levels up to 3 orders of magnitude higher than the insulative carbon foam with large stress concentrations noted in areas such as the transition to the nodal region or other processing defects. Furthermore, these stress concentrations drive the overall stress contours with the imperfect coating defects playing negligible roles. These findings suggest that processing research should focus on using high quality copper alloys characterized by high yield strengths to maintain mechanical integrity in thermo-mechanical loading applications. Recall that experimental studies of RVC carbon foams coated with thin 2-3 μm copper coatings found a strong copper property [85]. This high strength copper is likely due to the electro-chemistry procedure used to coat the carbon foams which deposits multiple layers of copper to achieve the full thickness value. By depositing the copper in many thin layers, the grain structure is fine and uniform reducing potential slip planes and resulting in a copper with enhanced strength properties.

5.4. Effect of Coating on Improving Electrical Conductivity of Insulating Foams

5.4.1. Problem Description

In order to complement the tailoring of thermal conductivity in insulative carbon foams, this investigation aims to demonstrate similar improvement in electrical conductivity through thin metallic coatings. In this case, the carbon foam ligaments are the same as in the previous section with the relevant properties shown in Table 3.9 as RVC foam along with the copper coating. This analysis couples the electrical response to the thermal analysis problem and the effects of Joule heating are evaluated along with the effective electrical properties.

A perfectly bonded, 5 μm thick uniform coating is used in this case to enable electrical conductivity in initially insulating foams. The boundary conditions used in this coupled thermal-electrical analysis problem are as described in Table 3.8. Material response on a more local scale is evaluated by investigating the same area of interest in Figure 5.13, which is located near the applied current boundary condition. In addition, a second coating case is considered where the thickness is increased to 10 μm to identify the impact of coating thickness on thermal-electrical response and corresponding Joule heating.

5.4.2. Results

To understand the impact of a perfect, uniform coating on reducing the bulk electrical resistivity of the insulative carbon foam, a method for calculating the effective resistivity is identified as described in Appendix C. This method is based on the one dimensional form of Ohm's law and results in an effective property characteristic of the applied electric potential. The insulative RVC carbon foam is roughly 5 orders of magnitude

higher in resistivity than the copper. The detailed single enclosed cavity VOI model confirms that thin (5 μm) copper coatings can significantly reduce the electrical resistivity of the carbon foam resulting in a 4 order of magnitude increase in bulk effective electrical conductivity over uncoated foams.

Further investigation of this improved electrical conductivity is evidenced by the electric current density magnitude plots presented in Figure 5.21. In this case, the electrical current density is 5 orders of magnitude higher at the outermost surface in carbon foams coated with 5 μm of copper. The uncoated RVC carbon foam has a current density magnitude of less than 0.3 A/mm^2 over the majority of the structure. These plots are also used to identify the electric energy dissipation paths from the voltage source to the ground sink and are found to be similar to the previously identified thermal dissipation paths consisting of aligned ligaments.

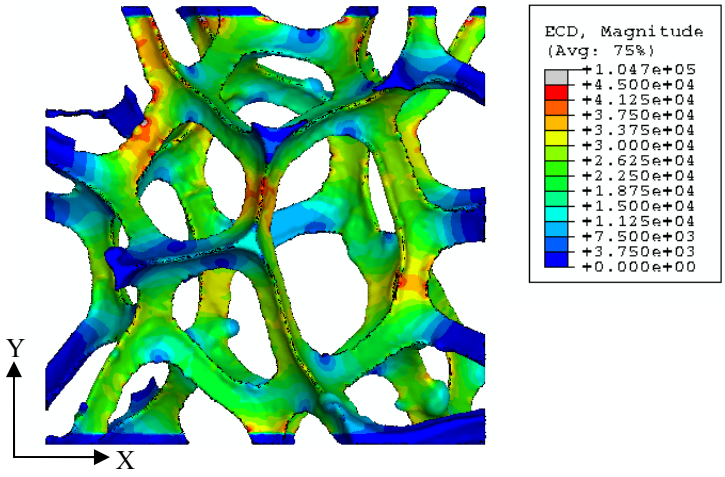

Figure 5.21. Electric current density magnitude (A/mm^2) for 5 μm Cu coated foam

In addition to tailoring the electrical conductivity of the carbon foams, thin copper coatings also impact the Joule heating. In uncoated RVC carbon foams the temperature increase over the majority of the VOI is less than 10 ºK due to the boundary conditions. However, in foams with thin copper coatings this temperature rise increases to 75 ºK as shown in Figure 5.22, with near uniform temperatures across the thickness of the coating in any given area. This change is a direct effect of the constitutive equation for Joule heating which indicates that the higher electrical conductivity of copper will lead to increased volumetric heat generation. Furthermore, at the steady state condition the carbon foam ligaments experience higher uniform temperature distribution across the composite cross section.

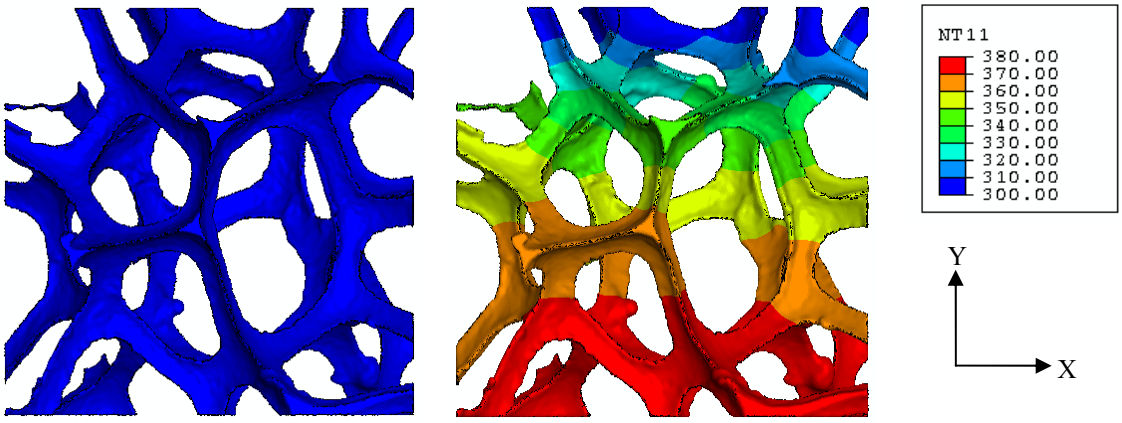

(a) (b)

Figure 5.22. Nodal temperature (ºK) distribution for (a) uncoated and (b) 5 µm Cu coated RVC carbon foams due to Joule heating

The final thermal-electrical investigation at this geometric VOI focuses on a thicker copper coating of 10 µm to address the influence of coating thickness. Nodal temperature plots indicate that the increased copper coating thickness has negligible effects on overall Joule heating. The rise in temperature due to the applied current is

maintained at 75 ºK because the constitutive relationship for heat generation does not include geometric effects. In a manner similar to the 5 μm coating case, the heat flux for this thicker coating is several orders of magnitude higher in the coating compared to the carbon foam; however, when comparing the magnitude of heat flux in the coating layers for both thickness values, minimal changes are detected.

The impact of thicker copper coatings on electrical response also appears to be small. The electric current density plots are very similar between the two cases and further demonstrate that copper coatings improve electric conductivity of insulative carbon foams. However, the effective electric conductivity, shown in Table 5.3, does appear to be a function of coating thickness such that doubling the coating thickness increases the conductivity by an order of magnitude. In addition, at this coating thickness (10 μm), the effective electrical conductivity of the coated carbon foam reaches that of pure copper as shown in Table 3.9.

Table 5.3. Effective electrical conductivity and resistivity in the loading direction as function of coating thickness

		Effective Electric Conductivity *1/Ω-m*		**Effective Electric Resistivity** *Ω-m*
Pristine RVC Carbon Foam	σ_y	1.33E+02	ρ_y	7.50E-03
Perfectly Bonded 5 μm Cu Coating	σ_y	8.00E+06	ρ_y	1.25E-07
Perfectly Bonded 10 μm Cu Coating	σ_y	6.36E+07	ρ_y	1.57E-08

5.4.3. Observations

Thin copper coatings have significant influence in tailoring the electrical conductivity of initially insulative carbon foams. For 5 μm coatings, the increase in bulk electric conductivity is 4 orders of magnitude. This is evidenced by a large increase in electric current density in the copper layer while the carbon foam remains relatively inactive.

Additional investigation of thicker copper coatings, show an additional order of magnitude increase in effective electrical conductivity. This suggests a logarithmic relationship between coating thickness and effective electrical conductivity. Therefore, processing researchers may place design limits on coating thickness in efforts to tailor electrical conductivity values.

In addition to improvement in electric conductivity, copper coatings also impact the Joule heating effects. In insulative carbon foams, the Joule heating results in 10 ºK increases in temperature and relatively small thermal expansion stresses. However, in copper coated foams, the resulting temperature rises to 75 ºK and may have more significant impact on thermal expansion stresses.

6. SEVERAL INTERCONNECTED CAVITIES STUDY

The final and largest carbon foam geometric scale investigated is several interconnected cavities VOI as shown in Figure 6.1. This scale consists of four complete cavities composed of approximately 240 ligaments and is used to study how loads are transferred in the bulk body. The applied field is undertaken to identify the impact of coatings on the coupled mechanical, thermal and electrical response. In this example, the large number of elements used to describe the geometry, as detailed in Section 3.2.3, requires considerable computational resources for analysis. These requirements are outlined in Appendix D along with the computational resources used by illustrations in preceding sections.

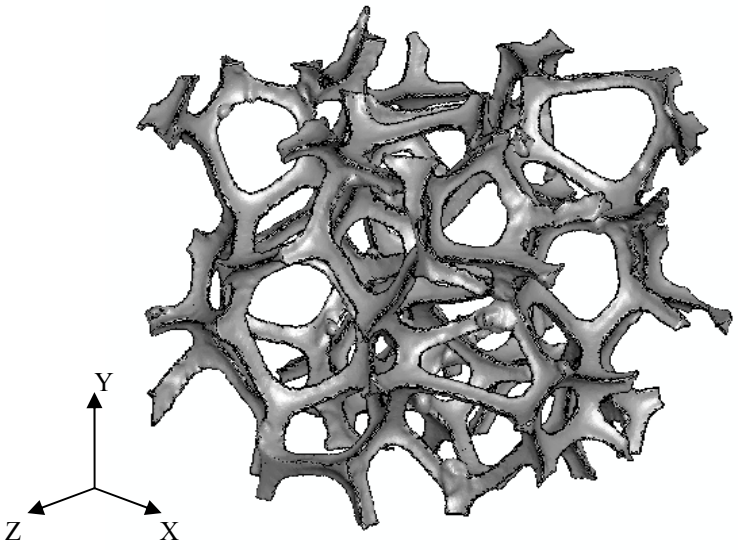

Figure 6.1. Several interconnected cavities VOI composed of four cavities

6.1. Coupled Thermal, Electric and Mechanical Response under Electric Fields

6.1.1. Problem Description

Recall that some applications may demand that the carbon foam product used is an RVC type, where the thermal and electrical conductivities are low due to an inability to graphitize the product. In order to tailor desired conductivities, a thin copper coating may be applied to the insulative foam. This tailorability is demonstrated with the four cavity VOI where the relevant properties are stated in Table 3.9 for the insulating RVC type carbon foam and the copper coating. Furthermore, the mechanical, thermal and electrical response at this scale is compared with observations from the smaller scale models presented previously.

The coating in this case is uniformly applied to the entire carbon foam substrate and is considered perfectly bonded in all regions. The coating is represented with two layers of elements as described in Section 3.2.3 for a total copper thickness of 10 μm. The total volume fraction of coating is 0.017 with respect to the entire enclosed volume, both solid material and empty cavity.

The analysis is undertaken in two parts to generate the full response of the structure to applied boundary conditions shown in Table 3.8. The initial analysis is a coupled thermal-electrical analysis to determine a steady state temperature distribution to the applied electric loading. This temperature distribution is used in the second part of the analysis to determine the mechanical response, through CTE coupling, to the electric load as previously described in Section 3.4.2.

6.1.2. Results

As with previous illustrations, the one dimensional form of Ohm's law is used to identify an effective electric conductivity in the loading direction for this VOI as outlined in Appendix C. At this scale, an insulative carbon foam with a thin 10 µm copper coating has an effective electrical conductivity of 5.52E+07 $(\Omega\text{-m})^{-1}$, or alternatively, an electric resistivity of 1.8E-08 Ω-m in the loading direction. These values are the same order of magnitude as calculations at the previous single enclosed cavity scale for the same coating configuration, but represent a decrease of 13%.

In addition to identifying an effective property, individual contour plots are studied to identify the mechanical, thermal and electrical response at this VOI. In the case of electrical response, the electric potential distribution is a direct consequence of the applied voltage conditions on the boundaries. As shown in Figure 6.2, the voltage varies in a linear relationship across the carbon foam from the voltage ground sink to the voltage source.

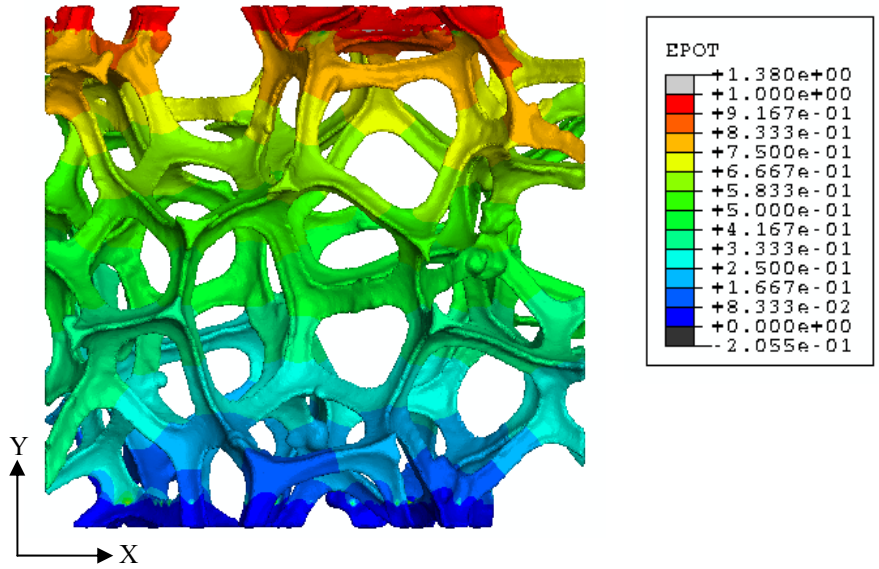

Figure 6.2. Electric potential (V) for 10 µm Cu coated foam

Furthermore, the boundary conditions develop an electric field across the carbon foam structure and result in current flowing through the ligaments. The current flow is characterized by the current density magnitude throughout the carbon foam structure as shown in Figure 6.3. The current density is restricted to the outer layer of copper coating, with the carbon foam itself displaying less than 0.3 A/mm^2.

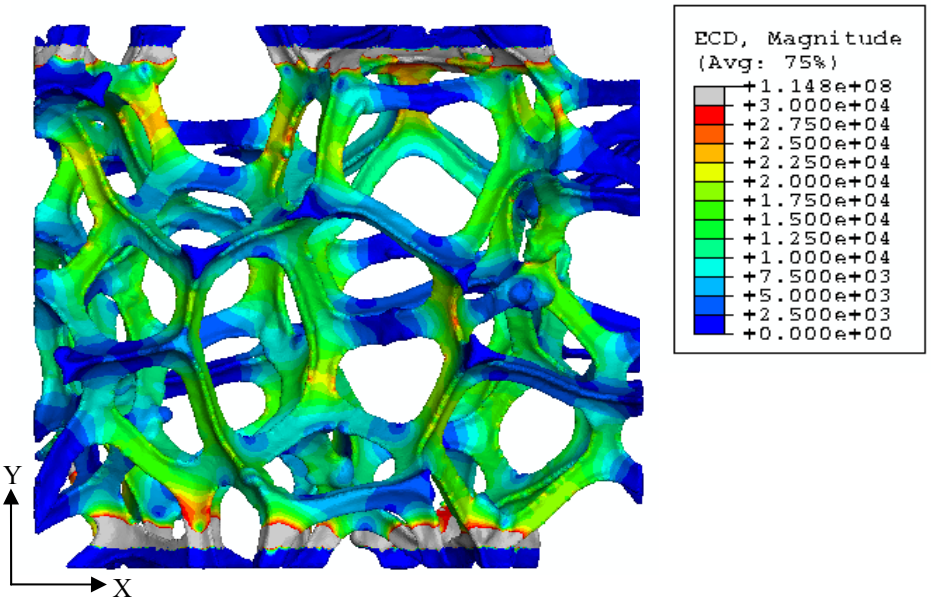

Figure 6.3. Electric current density magnitude (A/mm^2) for 10 µm Cu coated foam

To further examine the electric current present in the structure, the current density component in the loading direction is shown in Figure 6.4. This distribution indicates a preferred electric dissipation path corresponding with ligaments aligned with the global Y direction, with minor participation by off axis ligaments.

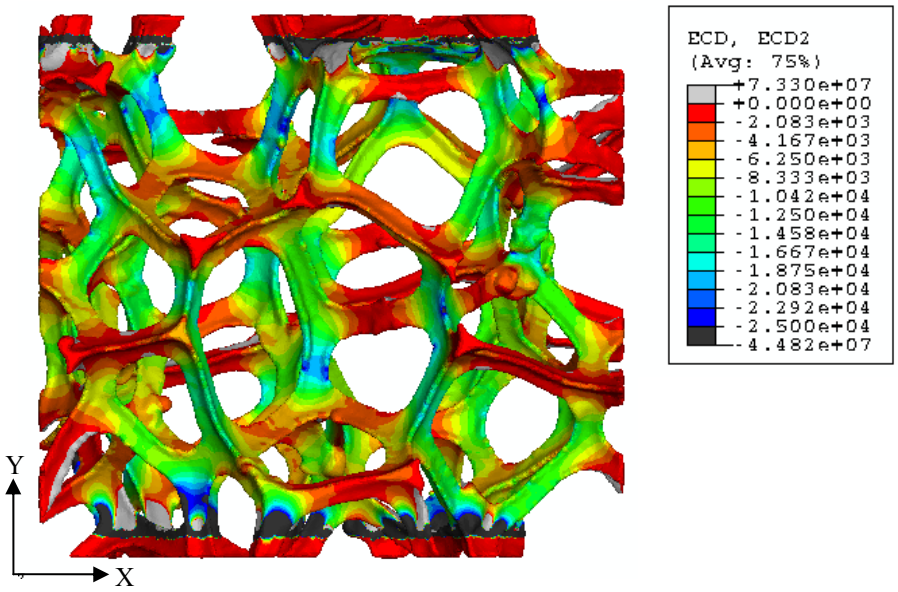

Figure 6.4. Electric current density (A/mm^2) Y component in 10 µm Cu coated foam

The current flow through the structure also impacts the thermal response of the structure through Joule heating as previously described. In this case, the temperature increases up to 100 ºK from the electric current, especially in regions adjacent to the high voltage boundary condition as shown in Figure 6.5. Further investigation shows that in the majority of the structure the carbon foam and coating achieve an equilibrium temperature; however, in the high voltage boundary area, the carbon foam is significantly cooler than the copper. This is attributed to a near zero current density magnitude in both the copper coating and carbon foam structure, which drives a lower temperature with a rapid increase in the area beyond.

The resulting temperature increase from initial conditions generates a mechanical deformation of the structure.. This deformation is a function of CTE with higher temperature regions undergoing larger expansions as shown in Figure 6.6. However, these deformations are small compared to the ligament cross section dimensions and are characterized by displacement magnitudes of less than 2 µm.

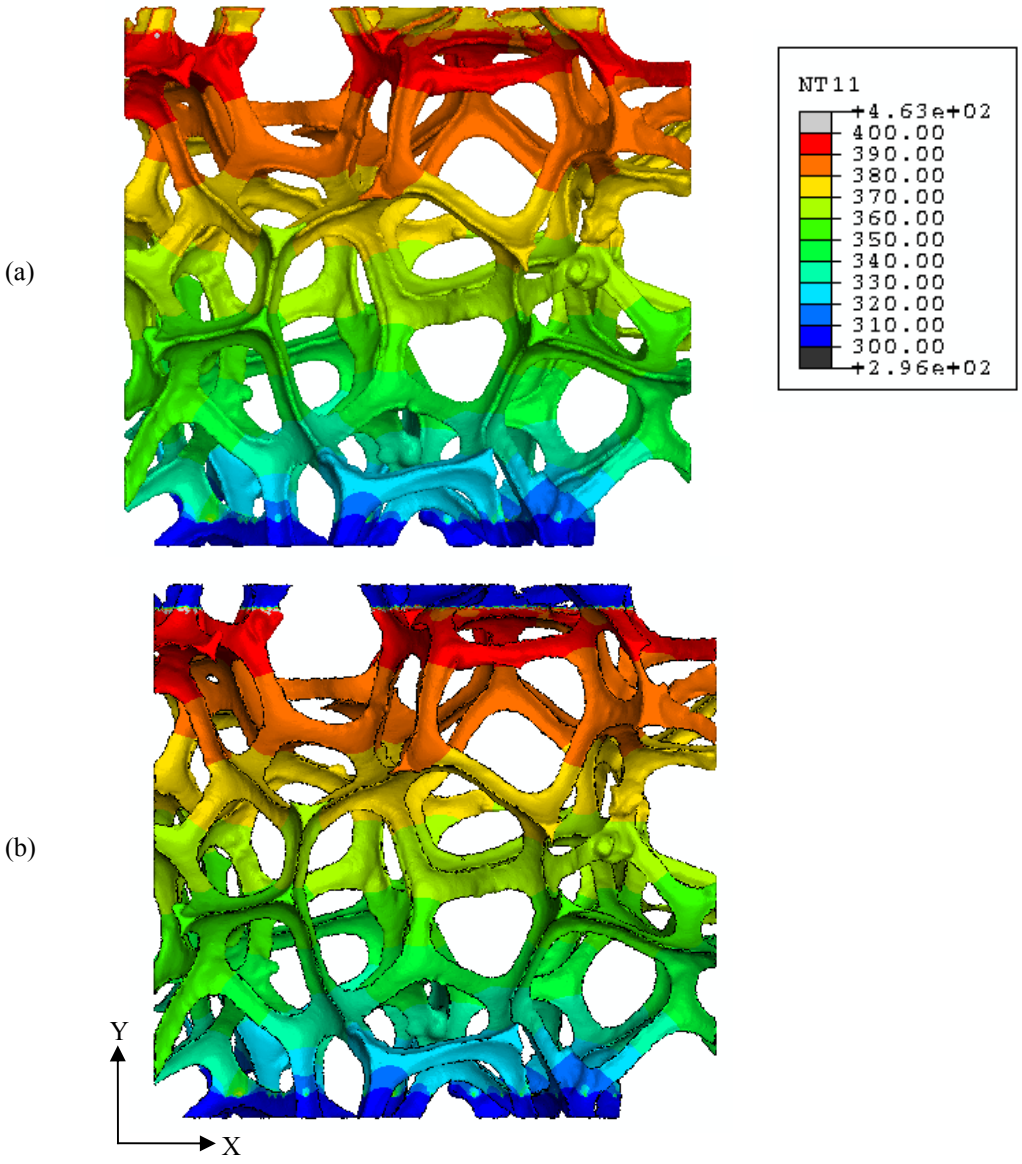

Figure 6.5. Nodal temperature (ºK) distribution for (a) Cu coating and (b) carbon foam due to Joule heating effects

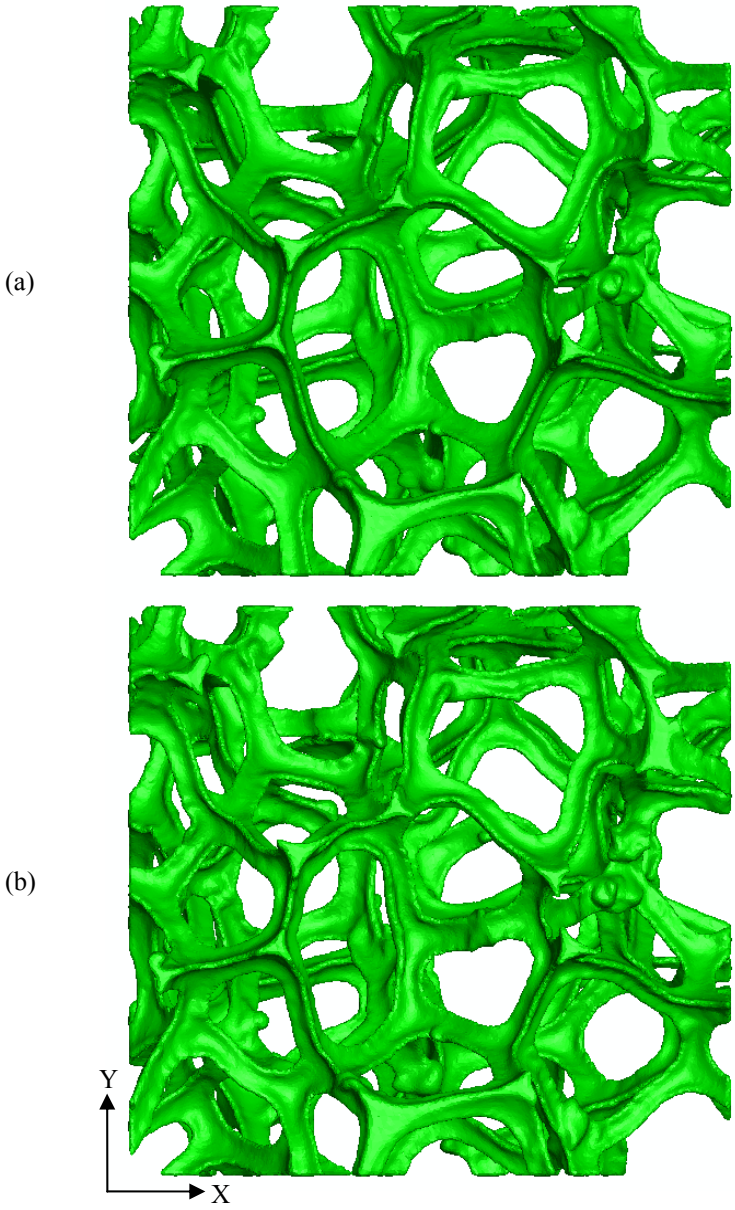

Figure 6.6. Carbon foam with 10 μm Cu coating in (a) reference and (b) deformed (50× scale) positions

As a final component of the current illustration, the impact of the Joule heating on the mechanical stress and strain response is evaluated. Although a uniform distribution in temperature develops between the carbon foam and copper coating in a given area, these materials have different CTE values driving thermal strain concentrations to develop. Figure 6.7 shows the maximum principal strain magnitude at the coating-carbon foam interface region. The highest maximum principal strain at the interface is in the range of 3000-4500 με. Moreover, more thermal strain concentrations appear in higher temperature regions with cooler areas having reduced strain levels.

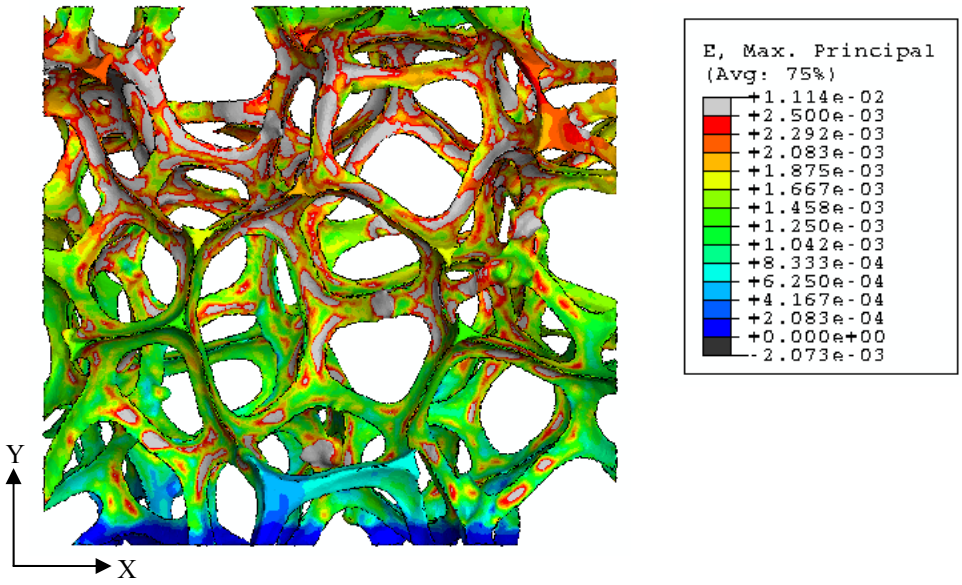

Figure 6.7. Maximum principal strain values at the coating-carbon foam interface

Inspection of the interface region also shows that processing artifacts—surface bump, globules and jagged edges—on individual ligaments appear drive strain concentrations as depicted in Figure 6.8. These strain concentrations also tend to form in the nodal regions suggesting that in local regions where the volume fraction of copper is changing, the impact of CTE mismatch is more significant.

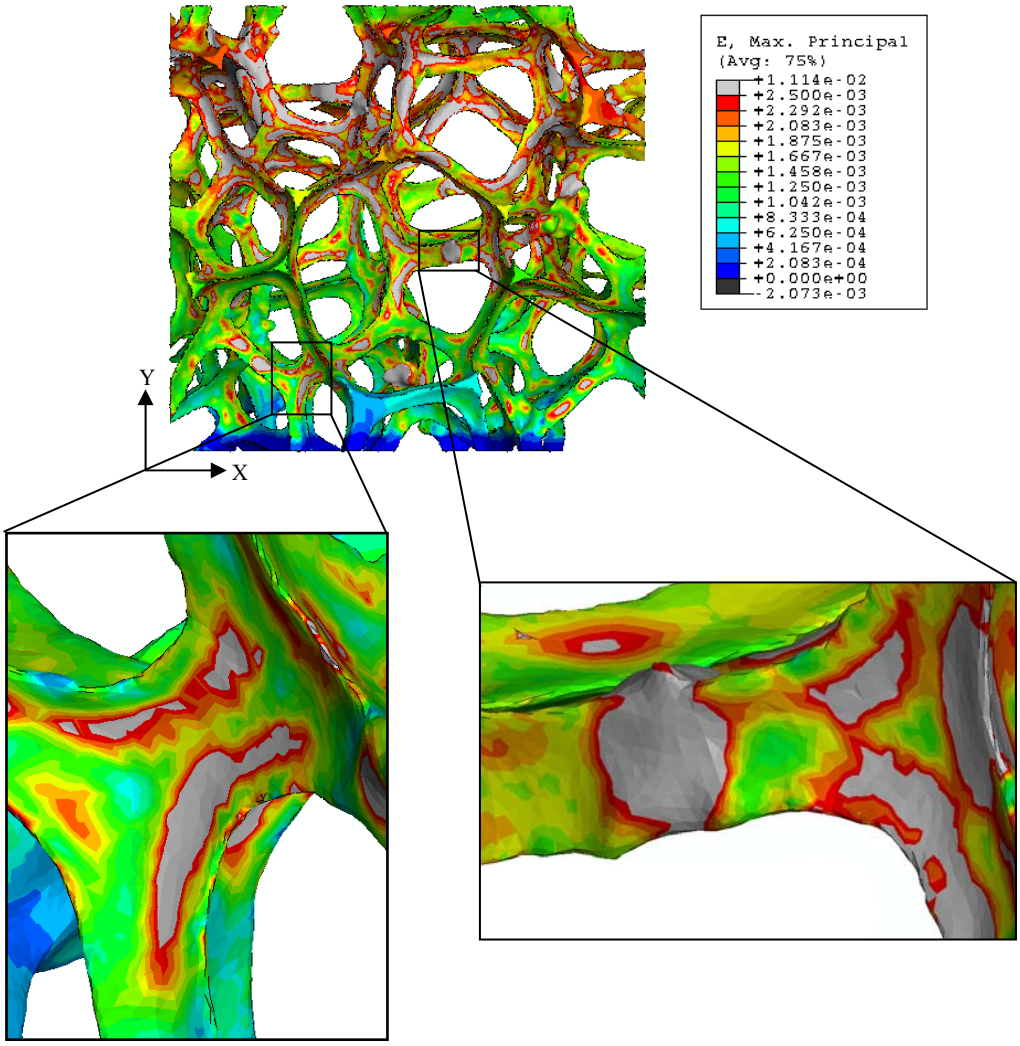

(a) (b)

Figure 6.8. Maximum principal strain concentrations at the interface in (a) nodal regions and (b) near processing artifacts

These interfacial strain concentration areas also appear to cause strain concentrations at the outer surface of the copper coating as shown in Figure 6.9. The maximum principal strain on this surface has a maximum value of approximately 2000 με, a reduction of 1500 με from interfacial values at the same local area.

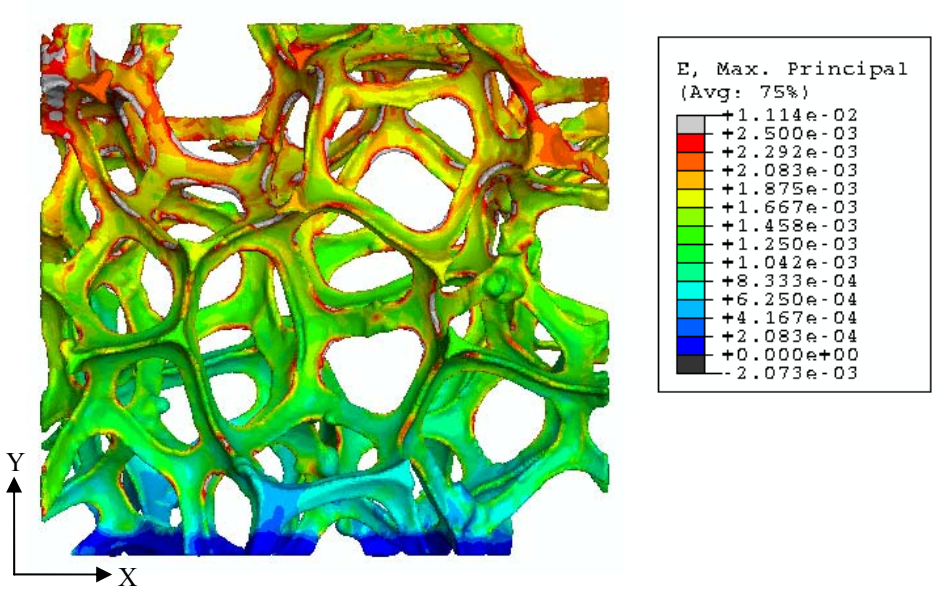

Figure 6.9. Maximum principal strain values at the outer surface of Cu coating

6.1.3. Observations

This study further supports smaller scale results indicating that thin copper coatings can tailor the electric conductivity of insulative carbon foams. The resulting effective conductivity values for thin 10 μm copper coatings at this scale confirm results found at smaller scales; however, the effective conductivity is more conservative at a larger scale indicating that a single enclosed cavity cannot fully predict the bulk behavior of carbon foams. As the largest geometric scale investigated in the present research, a definitive case for bulk behavior prediction at the several interconnected cavities VOI cannot be

made at this time; however, the order of magnitude of effective property calculations are likely to be validated by experimental bulk response.

In addition, this geometric scale illustration further demonstrates that the preferred dissipation path for electrical energy is in aligned ligaments to the loading direction. In order to further increase the electrical conductivity of copper coated carbon foams, processing research should focus on developing an oriented morphology to optimize the number of ligaments participating in electric dissipation. Furthermore, processing efforts should be undertaken to ensure that dissipation paths are not interrupted by coating defects previously described at other geometric scales.

Joule heating arising from electric current also appears to be a function of geometric scale investigated with the larger scale seeing a 25 ºK increase in temperature. Moreover, this temperature results in thermal strain development at the coating-carbon foam interface due to CTE mismatch between the materials. The highest strains occur in areas of high temperature; however large strain concentrations are also present in cooler areas where processing artifacts act to magnify the strain values. Processing researchers should focus on eliminating these features during the foaming process in order to minimize this impact and thereby reduce potential damage initiation points.

7. CONCLUSIONS

Multi-scale computational models are developed to facilitate and assess multi-functional carbon foams in an effort to interconnect and expand processing and property knowledge. A comprehensive protocol to translate microstructural features into a finite element mesh for computational simulation is created. Several case studies at different geometric scales were conducted to understand and assist the processing of tailored carbon foams. These examples centered around exploring an emerging technology requiring a low cost device with high thermal conductivity to dissipate energy while maintaining structural integrity. RVC carbon foams meet the requirement for a low cost base material and their low CTE values provide dimensional stability under thermal loading. Moreover, thin copper coatings on the initially insulative structure can functionalize the carbon foam providing enhanced thermal dissipation response.

The multi-scale approach was founded on detailed images of the carbon foam morphology obtained from high resolution micro-CT X-ray tomography. This method directly captures the geometry of individual ligaments along with the overall connectivity of the foam structure. This information was incorporated into the analytical model with an image to finite element conversion algorithm that included several unique optimization procedures to generate high quality elements, a requirement largely ignored by visualization research.

Material properties were defined by constructing a material unit cell composed of graphene regions to mimic the microstructures observed in carbon foams doped with additives. The resulting anisotropic properties were assigned to individual ligaments in the finite element model consistent with characterization of graphitized carbon foams under polarized light microscopy. Coating layers were included in the geometry of the model by introducing additional elements to the finite element mesh generated from micro-CT X-ray tomography. A procedure for modeling missing or debonded coating

was also developed. As an extension to coating, the entire cavity space was filled with finite elements to simulate complete infiltrations.

Several studies where undertaken to demonstrate the capabilities of the developed approach and provide valuable insight to processing researchers and designers. The first case study was devoted to the single ligament VOI and revealed that its thermo-mechanical response clearly highlighted the CTE mismatch between the carbon foam substrate and copper coating causing large thermal strains to develop in the coating at elevated temperatures. Furthermore, the development of large stresses in the copper coating led to amplified interfacial stresses in the bond area. Consequently, processing researchers should focus on utilizing copper alloys with enhanced strength properties and ensuring a quality bond with the substrate.

Further evidence of increased thermal performance through thin copper coatings was illustrated at the intermediate geometric scale of a single enclosed cavity VOI. At relatively small volume fractions, the thin copper coating served as a conduit for heat flux and facilitated a three order of magnitude improvement in effective thermal conductivity. Furthermore, this geometric scale was used to identify the impact of common coating imperfections—debonded or missing regions—on thermal performance since individual load paths could be isolated for examination. For small defects along a single dissipation path, the carbon foam ligament compensated for the imperfection carrying the energy across the gap with a 3% reduction in effective thermal conductivity. However, for large regions of missing coating, the path was eliminated for thermal energy dissipation and the effective thermal conductivity decreased 10% suggesting that processing researchers should emphasize complete coating coverage to maximize thermal performance. In the case of debonded area, an increase in interfacial stress was noted reiterating a need for high strength copper alloys with quality bonding between the copper and carbon foam substrate.

The impact of thin copper coatings on thermo-mechanical response at the largest geometric scale—several interconnected cavities—was used to explore the global deformation of the structure under thermal loads. As in the lower geometric scales, the consequence of CTE mismatch resulted in increased thermal strain in the coating subsequently creating additional stress at the interface. Furthermore, examination at this scale suggests that processing artifacts—surface irregularities, globules and jagged edges—on individual ligaments drive thermal strain concentrations and processing conditions need to be evaluated to minimize these features to reduce potential damage initiation sites.

In conclusion, unique and comprehensive physical knowledge gathered through micro-CT X-ray tomography images is successfully translated to computational models to assess the impact of micro- and macroscopic features in carbon foam morphology. This knowledge is essential in building in desirable physical and material properties at multiple scales for tailored response. The research undertaken herein forms the foundation for modeling multi-functional carbon foam response to aid processing researchers and designers as they explore applications in emerging technologies. The extension of the methodology is suitable to many difficult problems in the carbon foam community including diffusion driven tailoring of properties for oxidation resistance, or parametric design optimization in critical thermal management applications such as leading edges.

REFERENCES

1. Gallego, N.C. and Klett, J.W. (2003). Carbon foams for thermal management. *Carbon*, **41**: 1461-1466.
2. Hager, J.W. and Lake, M.L. (1992). Novel hybrid composites based on carbon foams. In: *Proceedings of the Material Research Society Symposium*, **270**: 29-34.
3. Kearns, K.M. (1999). Process for preparing pitch foams. U.S. Patent No. 5,868,947. Washington, DC: U.S. Patent and Trademark Office.
4. Kearns, K.M. (1999). Pitch foam products. U.S. Patent No. 5,961,814. Washington, DC: U.S. Patent and Trademark Office.
5. Klett, J.W. (2000). Process for making carbon foam. U.S. Patent No. 6,033,506. Washington, DC: U.S. Patent and Trademark Office.
6. Klett, J.W. (2001). Pitch-based carbon foam and composites. U.S. Patent No. 6,261,485. Washington, DC: U.S. Patent and Trademark Office.
7. Klett, J.W. (2002). Pitch-based carbon foam and composites. U.S. Patent No. 6,387,343. Washington, DC: U.S. Patent and Trademark Office.
8. Klett, J.W. (2002). Method for extruding pitch based foam. U.S. Patent No. 6,344,159. Washington, DC: U.S. Patent and Trademark Office.
9. Klett, J.W. (2002). Method of casting pitch based foam. U.S. Patent No. 6,398,994. Washington, DC: U.S. Patent and Trademark Office.
10. Stiller, A.H., Stansberry, P.G. and Zondlo, J.W. (1999). Method of making a carbon foam material and resultant product. U.S. Patent No. 5,888,469. Washington, DC: U.S. Patent and Trademark Office.
11. Stiller, A.H., Yocum, A. and Plucinski, J. (2001). Method of making a reinforced carbon foam material and related product. U.S. Patent No. 6,183,854. Washington, DC: U.S. Patent and Trademark Office.
12. Stiller, A.H., Stansberry, P.G. and Zondlo, J.W. (2001). Method of making a carbon foam material and resultant product. U.S. Patent No. 6,241,957. Washington, DC: U.S. Patent and Trademark Office.

13. Stiller, A.H., Stansberry, P.G. and Zondlo, J.W. (2002). Method of making a carbon foam material and resultant product. U.S. Patent No. 6,346,226. Washington, DC: U.S. Patent and Trademark Office.
14. Beechem, T.E. (2005). Growth mechanism and properties of novel carbon nanocomposite foams. M.S. Thesis, University of Dayton.
15. Rosebrock, G.J. (2005). Understanding and control of multifunctional graphitic foam properties. M.S. Thesis, University of Dayton.
16. Klett, J.W., McMillan, A.D., Gallego, N.C. and Walls, C.A. (2004). The role of structure on the thermal properties of graphitic foams. *Materials Science*, **39**: 3659-3676.
17. ERG Materials and Aerospace Corporation. Duocel Reticulated Vitreous Carbon Foam, http://www.ergaerospace.com (accessed November 2005).
18. Ultramet. Open cell Carbon Foam, http://www.ultramet.com (accessed November 2005).
19. Sihn, S. and Roy, A.K. (2001). Modeling and stress analysis of open cell carbon foam. In: *Proceedings of the 46th International SAMPE Symposium*, 230-242.
20. Oak Ridge National Laboratory. High Thermal Conductivity Graphite Foam, http://www.ms.ornl.gov/researchgroups/cmt/foam/foams.htm (accessed November 2005).
21. Poco Graphite. PocoFoam. http://www.poco.com (accessed November 2005).
22. Touchstone Research Laboratory. CFOAM Super Carbon Foam. http://www.cfoam.com (accessed November 2005).
23. Callister, W.D. (2000). *Material Science and Engineering: An Introduction*, **5th Edition**, John Wiley & Sons, Inc., New York.
24. Hall, R.B. and Hager, J.W. (1994). Evaluation of graphitic foams as low mass structural materials. In: *Proceedings of the Material Research Society Symposium*, **349**: 67-72.
25. Sarzynski, M.D. and Ochoa, O.O. (2005). Carbon foam core composite sandwich beams: flexure response. *Composite Materials*, **39**: 1067-1080.

26. Oberlin, A. (1984). Carbonization and graphitization. *Carbon*, **22**: 521-541.
27. Gaies, D. and Faber, K.T. (2002). Thermal properties of pitch-derived graphite foam. *Carbon*, **40**: 1131-1150.
28. Klett, J.W. and Burchell, T.D. (2000). Pitch-based carbon foam heat sink with phase change material. U.S. Patent No. 6,037,032. Washington, DC: U.S. Patent and Trademark Office.
29. Griffith, G. (2002). Carbon foam: a next-generation structural material. *Industrial Heating*, **69**(11): 47-52.
30. Gibson, L.J. and Ashby, M.F. (1997). *Cellular Solids: Structures and Properties*. **2nd Edition**. Cambridge University Press, Cambridge.
31. Yang, J., Shen, Z. and Hao, Z. (2004). Microwave characteristics of sandwich composites with mesophase pitch carbon foams as core. *Carbon*, **42**: 1882-1885.
32. Rodriguez, D.E, Ochoa, O.O, Hahn, M. and Sue, H.J.. (2007). Processing, morphology and biocompatibility of hydroxyapatite and carbon foam reinforced bioresorbable polymer. In: *Proceedings of the 22nd Annual ASC Technical Conference* [CD].
33. Ko, W.L. (1965). Deformations of foamed elastomers. *Cellular Plastics*, **1**: 45-50.
34. Christensen, R.M. (1986). Mechanics of low density materials. *Mechanics and Physics of Solids*, **34**: 563-578.
35. Warren, W.E. and Kraynik, A.M. (1988). The linear elastic properties of open cell foams. *Applied Mechanics*, **55**: 341-346.
36. Warren, W.E. and Kraynik, A.M. (1997). Linear elastic behavior of a low-density Kelvin foam with open cells. *Applied Mechanics*, **64**: 787-794.
37. Hashin, Z. (1962). The elastic moduli of heterogeneous materials. *Applied Mechanics*, **29**:143-150.
38. Hill, R. (1965). A self-consistent mechanics of composite materials. *Mechanics and Physics of Solids*, **13**:213-222.

39. Budiansky, B. (1965). On the elastic moduli of some heterogeneous materials. *Mechanics and Physics of Solids*, **13**:223-227.
40. Christensen, R.M. and Lo, K.H. (1979). Solutions for effective shear properties in three phase sphere and cylinder models. *Mechanics and Physics of Solids*, **27**:315-330.
41. Benveniste, Y. (1987). A new approach to the application of Mori-Tanaka's theory in composite materials. *Mechanics of Materials*, **6**:147-157.
42. Christensen, R.M. (1979). *Mechanics of Composite Materials*, Krieger Publishing Company, Malabar, FL.
43. Hashin, Z. and Shtrikman, S. (1963). A variational approach to the theory of the elastic behavior of multiphase materials. *Mechanics and Physics of Solids*, **11**:127-140.
44. Garboczi, E.J. and Day, A.R. (1995). An algorithm for computing the effective linear elastic properties of heterogeneous materials: three-dimensional results for composites with equal phase Poisson ratios. *Mechanics and Physics of Solids*, **43**: 1349-1362.
45. Arns, C.H., Knackstedt, M.A, Pinczewski, W.V. and Garboczi, E.J. (2002). Computation of linear elastic properties from microtomographic images: methodology and agreement between theory and experiment. *Geophysics*, **67**: 1396-1405.
46. Jaecques, S.V.N., Oosterwyck, H.V., Muraru, L., Cleynenbreugel, T.V., Smet, E.D., Wevers, M., Naert, I. and Vander Sloten, J. (2004). Individualised, micro-CT-based finite element modeling as a tool for biomechanical analysis related to tissue engineering of bone. *Biomaterials*, **25**: 1683-1696.
47. Saadatfar, M., Arns, C.H., Knackstedt, M.A. and Senden, T. (2004). Mechanical and transport properties of polymeric foams derived from 3D images. *Colloids and Surfaces A: Physicochemical Engineering Aspects*, **263**: 284-289.

48. Youssef, S., Marie, E. and Gaertner, R. (2005). Finite element modeling of the actual structure of cellular materials determined by x-ray tomography. *Acta Materialia*, **53**: 719-730.
49. Roberts, A.P. and Garboczi, E.J. (2002). Elastic properties of model random three-dimensional open cell solids. *Mechanics and Physics of Solids*, **50**: 33-55.
50. Ravindran, K., Brown, S.G.R. and Spittle, J.A. (1999). Prediction of the effective thermal conductivity of three-dimensional dendritic regions by the finite element method. *Materials Science and Engineering: A*, **269**: 90-97.
51. Sandhu, S.S. and Hager, J.W. (1992). Formulation of a mathematical process model for the foaming of a mesophase carbon precursor. In: *Proceedings of the Material Research Society Symposium*, **270**: 35-40.
52. Rosebrock, G., Elgafy, A., Beechem, T. and Lafdi, K. (2005). Study of the growth and motion of graphitic foam bubbles. *Carbon*, **43**: 3075-3087.
53. Beechem, T., Lafdi, K. and Elgafy, A. (2005). Bubble growth mechanism in carbon foams. *Carbon*, **43**: 1055-1064.
54. Anderson, D.P., Gunnison, K.E. and Hager, J.W. (1992). Ligament structure of open cell carbon foams and the construction of models based on that structure. In: *Proceedings of the Material Research Society Symposium*, **270**: 47-52.
55. Hager, J.W. (1992). Idealized strut geometries for open-celled foams. In: *Proceedings of the Material Research Society Symposium*, **270**: 41-46.
56. Maruyama, B., Spowart, J. E., Hooper, D. J., Mullens, H.M., Druma, A.M, Druma, C. and Alam, M.K. (2006). A new technique for obtaining three-dimensional structures in pitch-based carbon foams. *Scripta Materialia*, **54**: 1709-1713.
57. Mukhopadhyay, S.M., Mahadev, N., Joshi, P., Roy, A.K., Kearns, K.M. and Anderson, D.P. (2002). Structural investigation of graphitic foam. *Applied Physics*, **91**: 3415-3420.
58. Mehta, R., Anderson, D.P. and Hager, J.W. (2003). Graphitic open-celled carbon foams: processing and characterization. *Carbon*, **41**: 2174-2176.

59. Klett, J., Hardy, R., Romine, E., Walls, C. and Burchell, T. (2000). High-thermal-conductivity, mesophase-pitch-derived carbon foams: effect of precursor on structure and properties. *Carbon*, **38**, 953-973.
60. Li, K., Gao, X.L. and Roy, A.K. (2003). Micromechanics model for a three-dimensional open cell foams using tetrakaidecahedral unit cell and Castigliano's second theorem. *Composite Science and Technology*, **63**: 1769-1781.
61. Sihn, S. and Roy, A.K. (2004). Modeling and prediction of bulk properties of open cell carbon foam. *Mechanics and Physics of Solids*, **52**: 167-191.
62. Yu, Q., Thompson, B.E. and Straatman, A.G. (2006). A unit cube-based model for heat transfer and fluid flow in porous carbon foam. Contributed by the Heat transfer division of ASME for publication in the Journal of Heat Transfer, **128**: 352-360.
63. Tee, C.C., Klett, J.W., Stinton, D.P. and Yu, N. (1999). Thermal conductivity of porous carbon foam. *American Carbon Society, 24th Conference* in Charleston SC, 130-131.
64. SkyScan 1172 high-resolution micro-CT system. http://www.skyscan.be/. (accessed September 2007).
65. Herman, G. T. (1980). *Image Reconstruction from Projections: The Fundamentals of Computerized Tomography*. Academic Press, Inc., New York.
66. Kak, A.C. and Slaney, M. (1988). *Principles of Computerized Tomographic Imaging*. IEEE, Inc., New York.
67. Dresselhaus, M.S. (1996). *Science of Fullerenes and Carbon Nanotubes*. Academic Press, San Diego.
68. Robinson, P.C. and Bradbury, S. (1992). *Qualitative Polarized Light Microscopy*. Oxford University Press, New York.
69. Lorensen, W. and Cline, H.E. (1987). Marching cubes: a high resolution 3D surface construction algorithm. In: *Proceedings of the 14th Annual Conference on Computer Graphics and Interactive Techniques*, **21**(4): 163-169.

70. Ohtake, Y. and Belyaev, A. (2002). Dual-primal mesh optimization for polygonized implicit surfaces with sharp features. *Computing and Information Science in Engineering*, **2**:277-284.
71. Garland, M. and Heckbert P.S. (1997). Surface simplification using quadric error metrics. In: *Proceedings of the 24th Annual Conference on Computer Graphics and Interactive Techniques*, 209-216.
72. Vollmer, J., Mencl, R. and Müller, H. (1999). Improved laplacian smoothing of noisy surface meshes. *Computer Graphics Forum*, **18(3)**: 131-138.
73. Attali, D., Cohen-Steiner, D. and Edelsbrunner, H. (2005). Extraction and simplification of iso-surfaces in tandem. In: *Proceedings of the 3rd Annual Eurographics Symposium on Geometry Processing*, **255**: 139.
74. Ju, T., Losasso, F., Schaefer, S. and Warren, J. (2002). Dual countouring of hermite data. In: *Proceedings of the 29th Annual Conference on Computer Graphics and Interactive Techniques*, 339-346.
75. Alliez, P., Cohen-Steiner, D., Yvinec, M. and Desbrun, M. (2005). Variational tetrahedral meshing. In: *Proceedings of the 32nd Annual Conference on Computer Graphics and Interactive Techniques*, 617-625.
76. Slaughter, W.S. (2002). *The Linearized Theory of Elasticity*. Birkhäuser, Boston.
77. Chou, P.C. and Pagano, N.J. (1992). *Elasticity: Tensor, Dyadic and Engineering Approaches*. Dover, New York.
78. Mills, A.F. (1999). *Heat Transfer*. **2nd Edition**. Prentice Hall, Inc., Upper Saddle River, NJ.
79. Özişik, M.N. (1980). *Heat Conduction*. John Wiley & Sons, Inc., New York.
80. Simonyi, K. (1963). *Foundations of Electrical Engineering*. Peragmon Press Ltd, Oxford.
81. ABAQUS documentation collection, **Version 6.6**. (2006). ABAQUS, Inc., Pawtucket, RI.
82. Schaefer, S. Personal communication and unpublished research. 2006-2007.

83. Taubin, G. (1995). A signal processing approach to fair surface design. In: *Proceedings of the 26th Annual Conference on Computer Graphics and Interactive Techniques*, 351-358.
84. Ruoff, R.S. and Lorents, D.C. (1995). Mechanical and thermal properties of carbon nanotubes. *Carbon*, **33**: 925-930.
85. Lafdi, K. Personal communication and unpublished reports. Multiple dates from 2003-2007.
86. Renouf-Glauser, A., Rose, J., Farrar, D. and Cameron, R. (2005). The effect of cyrstallinity on the deformation mechanism and bulk mechanical properties of PLLA. *Biomaterials*, **26**: 5771-5782.
87. Nature Works. PLLA polymer engineering technical data sheets containing material properties, http://www.natureworksllc.com/ (accessed November 2005).
88. Nakagawa, T., Nakiri, T., Hosoya, R. and Tajitsu, Y. (2004). Electrical properties of biodegradable polylactic acid film. In: *Proceedings of the 7th International Conference on Properties and Applications of Dielectric Materials*, **2**: 499-502..
89. Reddy, J.N. (1993). *An Introduction to the Finite Element Method*, **2nd Edition**. McGraw-Hill, Boston.

APPENDIX A. FINITE ELEMENT FORMULATION

A variational approach is used to reduce the governing differential equations in Section 2.3 for finite element analysis formulation [89]. As an example, consider the following finite element formulation for the pure thermal field boundary value problem in three dimensions based on the governing heat conduction equation in Equation 13. With the assumptions of a homogeneous, anisotropic material with no internal heat generation, the heat conduction equation reduces to Equation 35.

$$\begin{aligned} 0 = &-\frac{\partial}{\partial x}\left(k_{11}\frac{\partial T}{\partial x} + k_{12}\frac{\partial T}{\partial y} + k_{13}\frac{\partial T}{\partial z} \right) \\ &-\frac{\partial}{\partial y}\left(k_{12}\frac{\partial T}{\partial x} + k_{22}\frac{\partial T}{\partial y} + k_{23}\frac{\partial T}{\partial z} \right) \\ &-\frac{\partial}{\partial z}\left(k_{13}\frac{\partial T}{\partial x} + k_{23}\frac{\partial T}{\partial y} + k_{33}\frac{\partial T}{\partial z} \right) \end{aligned} \qquad [35]$$

The first step in the finite element formulation is to express the variational form of the governing differential equation for a typical element (Ω^e). This is achieved by multiplying the residual of Equation 35 by a weight function (w) and integrating over the domain of the element as shown in Equation 36.

$$0 = \int_{\Omega^e} w\left(-\frac{\partial F_1}{\partial x} - \frac{\partial F_2}{\partial y} - \frac{\partial F_3}{\partial z} \right) dV \qquad [36]$$

where $$F_1 = k_{11}\frac{\partial T}{\partial x} + k_{12}\frac{\partial T}{\partial y} + k_{13}\frac{\partial T}{\partial z}$$

$$F_2 = k_{12}\frac{\partial T}{\partial x} + k_{22}\frac{\partial T}{\partial y} + k_{23}\frac{\partial T}{\partial z}$$

$$F_3 = k_{13}\frac{\partial T}{\partial x} + k_{23}\frac{\partial T}{\partial y} + k_{33}\frac{\partial T}{\partial z}$$

Next, the differentiation is distributed between the weight function (w) and the unknown function (T) through the application of integration by parts. This weakens the continuity requirement for the solution; hence the variational form shown in Equation 37 is often termed the weak form.

$$0 = \int_{\Omega^e}\left(\frac{\partial w}{\partial x}F_1 - \frac{\partial (wF_1)}{\partial x} + \frac{\partial w}{\partial y}F_2 - \frac{\partial (wF_2)}{\partial y} + \frac{\partial w}{\partial z}F_3 - \frac{\partial (wF_3)}{\partial z}\right)dV \qquad [37]$$

The final step in developing the variational form of the governing differential equation is to apply Gauss's theorem in Equation 3. From Equation 38, it is possible to identify the essential and natural boundary conditions. In this case, specification of temperature (T) is the primary, or essential, variable while specification of the heat flux normal to the surface (q_n) is the secondary, or natural variable.

$$0 = \int_{\Omega^e}\left(\frac{\partial w}{\partial x}F_1 + \frac{\partial w}{\partial y}F_2 + \frac{\partial w}{\partial z}F_3\right)dV - \int_S wq_n dS \qquad [38]$$

where $\quad q_n = n_x F_1 + n_y F_2 + n_z F_3$

Next, an approximation to the unknown function is assumed based on the Lagrange family of interpolation functions (ψ) as in Equation 39. In this case, T_j^e is the value of temperature as the jth node of the element.

$$T(x,y,z) \approx T^e(x,y,z) = \sum_{j=1}^{N} T_j^e \psi_j^e(x,y,z) \qquad [39]$$

The final step in formulating the finite element model is to identify an appropriate weight function. In this case, a Galerkin approach is used such that the weight functions (w) are identical to the interpolation functions (ψ). In order to identify the n unknowns (T_j) n independent equations are needed. In this example, the ith equation is shown in Equation 40 in summation and matrix formats.

$$\sum_{j=1}^{n} K_{ij}^e T_j^e = Q_i^e \qquad \left[K^e\right]\left\{T^e\right\} = \left\{Q^e\right\} \qquad [40]$$

where

$$K_{ij}^e = \int_{\Omega^e} \left[\begin{array}{l} \dfrac{\partial \psi_i}{\partial x}\left(k_{11}\dfrac{\partial \psi_j}{\partial x} + k_{12}\dfrac{\partial \psi_j}{\partial y} + k_{13}\dfrac{\partial \psi_j}{\partial z} \right) \\ + \dfrac{\partial \psi_i}{\partial y}\left(k_{12}\dfrac{\partial \psi_j}{\partial x} + k_{22}\dfrac{\partial \psi_j}{\partial y} + k_{23}\dfrac{\partial \psi_j}{\partial z} \right) \\ + \dfrac{\partial \psi_i}{\partial z}\left(k_{13}\dfrac{\partial \psi_j}{\partial x} + k_{23}\dfrac{\partial \psi_j}{\partial y} + k_{33}\dfrac{\partial \psi_j}{\partial z} \right) \end{array} \right] dV$$

$$Q_i^e = \int_S \psi_i q_n dS$$

This represents the system of equations for a single arbitrary element. For simplicity in calculating the integral expression, a master element and its interpolation functions are identified for the approximation. For a linear tetrahedral element, the approximation function is shown in Equation 41, where T_j represents the temperature at node j and (ξ, η, γ) are natural coordinates for the isoparametric element. Details regarding specific elements used in this research and their respective interpolation functions and approximations are discussed in Appendix B.

$$T^e = \sum_{j=1}^{N} \psi_j T_j = \psi_1 T_1 + \psi_2 T_2 + \psi_3 T_3 + \psi_4 T_4 = (1 - \xi - \eta - \gamma) T_1 + \xi T_2 + \eta T_3 + \gamma T_4 \qquad [41]$$

In order to calculate the integral expression in Equation 40 for the K_{ij} components, the derivatives with respect to the global coordinates must be transformed into the natural coordinates of the master element. This is achieved through the use of the chain rule shown in Equation 42, where J is termed the Jacobian matrix. This matrix must be invertible as determined through the relationship in Equation 43.

$$\begin{Bmatrix} \frac{\partial \psi}{\partial \eta} \\ \frac{\partial \psi}{\partial \xi} \\ \frac{\partial \psi}{\partial \gamma} \end{Bmatrix} = \begin{bmatrix} \frac{\partial x}{\partial \eta} & \frac{\partial y}{\partial \eta} & \frac{\partial z}{\partial \eta} \\ \frac{\partial x}{\partial \xi} & \frac{\partial y}{\partial \xi} & \frac{\partial z}{\partial \xi} \\ \frac{\partial x}{\partial \gamma} & \frac{\partial y}{\partial \gamma} & \frac{\partial z}{\partial \gamma} \end{bmatrix} \begin{Bmatrix} \frac{\partial \psi}{\partial x} \\ \frac{\partial \psi}{\partial y} \\ \frac{\partial \psi}{\partial z} \end{Bmatrix} = [J] \begin{Bmatrix} \frac{\partial \psi}{\partial x} \\ \frac{\partial \psi}{\partial y} \\ \frac{\partial \psi}{\partial z} \end{Bmatrix} \qquad [42]$$

$$\det[J]=\begin{vmatrix}\frac{\partial x}{\partial \eta} & \frac{\partial y}{\partial \eta} & \frac{\partial z}{\partial \eta}\\ \frac{\partial x}{\partial \xi} & \frac{\partial y}{\partial \xi} & \frac{\partial z}{\partial \xi}\\ \frac{\partial x}{\partial \gamma} & \frac{\partial y}{\partial \gamma} & \frac{\partial z}{\partial \gamma}\end{vmatrix} > 0 \qquad [43]$$

Using the inverse Jacobian relationships, the finite element model equation in the natural coordinates for a master element take the form of Equation 44, where J^*_{ij} is the ijth position in the inverse Jacobian matrix.

$$\sum_{j=1}^{n} K_{ij}^e T_j^e = Q_i^e \qquad \left[K^e\right]\left\{T^e\right\}=\left\{Q^e\right\} \qquad [44]$$

where

$$K_{ij}^e = \int_{\Omega^e} \begin{bmatrix} G_i^1\left(k_{11}G_j^1 + k_{12}G_j^2 + k_{13}G_j^3\right) \\ + G_i^2\left(k_{12}G_j^1 + k_{22}G_j^2 + k_{23}G_j^3\right) \\ + G_i^3\left(k_{13}G_j^1 + k_{23}G_j^2 + k_{33}G_j^3\right)\end{bmatrix} \det[J]\, d\xi\, d\eta\, d\gamma$$

$$G_k^1 = J_{11}^* \frac{\partial \psi_k}{\partial \eta} + J_{12}^* \frac{\partial \psi_k}{\partial \xi} + J_{13}^* \frac{\partial \psi_k}{\partial \gamma}$$

$$G_k^2 = J_{21}^* \frac{\partial \psi_k}{\partial \eta} + J_{22}^* \frac{\partial \psi_k}{\partial \xi} + J_{23}^* \frac{\partial \psi_k}{\partial \gamma}$$

$$G_k^3 = J_{31}^* \frac{\partial \psi_k}{\partial \eta} + J_{32}^* \frac{\partial \psi_k}{\partial \xi} + J_{33}^* \frac{\partial \psi_k}{\partial \gamma}$$

$$Q_i^e = \int_S \psi_i q_n dS$$

In the case of an isotropic material system, calculation of the master element equations is straightforward; however, in the case of anisotropic materials, the thermal conductivity matrix must also be transformed to the master coordinate. Alternatively, these material constants can be transformed to the global coordinate system and substituted in the transformed element equations prior to assembly of the finite element equations.

The integral expressions in Equation 44 are difficult to calculate exactly due to the complex algebraic coefficients; therefore numerical integration schemes are employed to approximate the value of these expressions. A common approach to numerical integration is the use of Gauss quadrature as shown in Equation 45. In this case, several integration points are selected based on the element order. At these positions, the function is evaluated and then weighted accordingly. The sum of result at each integration point is an approximation of the volume integral. In finite element methods, this procedure would be undertaken for each K_{ij} matrix value.

$$\int_{\Omega} F(\xi,\eta,\gamma)d\xi d\eta d\gamma \approx \sum_{K=1}^{P}\sum_{J=1}^{M}\sum_{I=1}^{N} F(\xi_I,\eta_J,\gamma_K)W_I W_J W_K \qquad [45]$$

After calculating the master element equations through Gauss quadrature and transforming to a global coordinate system through the Jacobian matrix, it is possible to assemble the equations for each individual element in the global mesh. Consider the transformed element equations in Equation 46 where the superscript n references a specific element number.

$$\begin{bmatrix} K_{11}^n & K_{12}^n & K_{13}^n & K_{14}^n \\ K_{21}^n & K_{22}^n & K_{23}^n & K_{24}^n \\ K_{31}^n & K_{32}^n & K_{33}^n & K_{34}^n \\ K_{41}^n & K_{42}^n & K_{43}^n & K_{44}^n \end{bmatrix} \begin{Bmatrix} T_1^n \\ T_2^n \\ T_3^n \\ T_4^n \end{Bmatrix} = \begin{Bmatrix} Q_1^n \\ Q_2^n \\ Q_3^n \\ Q_4^n \end{Bmatrix} \quad [46]$$

For the two element linear tetrahedral mesh shown in Figure A.1, assembly is undertaken by populating the K_{ij} matrix for each element based on the global node numbers. This assembly procedure ensures that the primary variable (T) is continuous at connecting nodes. In addition, the secondary variable (Q) is balanced such that if no external heat flux boundary condition is applied, the assembled value is zero; otherwise it is the externally applied condition (Q_o). The final assembled system of equations is in Equation 47, where the T_1 is the temperature at node 1, etc.

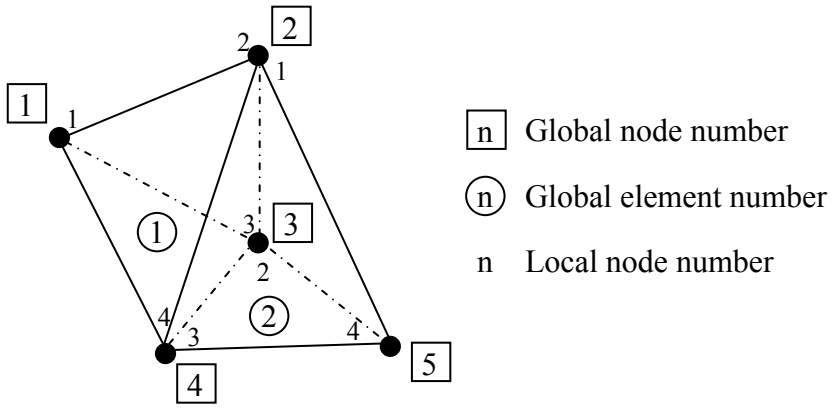

Figure A.1. Finite element mesh composed of two linear tetrahedral elements

$$\begin{bmatrix} K_{11}^1 & K_{12}^1 & K_{13}^1 & K_{14}^1 & 0 \\ K_{21}^1 & K_{22}^1+K_{11}^2 & K_{23}^1+K_{12}^2 & K_{24}^1+K_{13}^2 & K_{14}^2 \\ K_{31}^1 & K_{32}^1+K_{21}^2 & K_{33}^1+K_{22}^2 & K_{34}^1+K_{23}^2 & K_{24}^2 \\ K_{41}^1 & K_{42}^1+K_{31}^2 & K_{43}^1+K_{32}^2 & K_{44}^1+K_{33}^2 & K_{34}^2 \\ 0 & K_{41}^2 & K_{42}^2 & K_{43}^2 & K_{44}^2 \end{bmatrix} \begin{Bmatrix} T_1 = T_1^1 \\ T_2 = T_2^1 + T_1^2 \\ T_3 = T_3^1 + T_2^2 \\ T_4 = T_4^1 + T_3^2 \\ T_5 = T_4^2 \end{Bmatrix} = \begin{Bmatrix} Q_1 = Q_1^1 \\ Q_2 = Q_2^1 + Q_1^2 \\ Q_3 = Q_3^1 + Q_2^2 \\ Q_4 = Q_4^1 + Q_3^2 \\ Q_5 = Q_4^2 \end{Bmatrix} \quad [47]$$

The final step in the finite element formulation is to apply nodal boundary conditions to Equation 47. For instance, consider the case where a temperature sink of T_{cold} occurs at node 1, while a temperature source of T_{hot} is at node 5. These boundary conditions would result in a temperature gradient across the two element mesh. To apply these boundary conditions, simply set the values in the T_j matrix as shown in Equation 48. In addition, balance of the secondary variable (Q) must be enforced such that if no heat flux is applied directly to connected nodes the assembled value is zero.

$$\begin{bmatrix} K_{11}^1 & K_{12}^1 & K_{13}^1 & K_{14}^1 & 0 \\ K_{21}^1 & K_{22}^1+K_{11}^2 & K_{23}^1+K_{12}^2 & K_{24}^1+K_{13}^2 & K_{14}^2 \\ K_{31}^1 & K_{32}^1+K_{21}^2 & K_{33}^1+K_{22}^2 & K_{34}^1+K_{23}^2 & K_{24}^2 \\ K_{41}^1 & K_{42}^1+K_{31}^2 & K_{43}^1+K_{32}^2 & K_{44}^1+K_{33}^2 & K_{34}^2 \\ 0 & K_{41}^2 & K_{42}^2 & K_{43}^2 & K_{44}^2 \end{bmatrix} \begin{Bmatrix} T_1 = T_{cold} \\ T_2 \\ T_3 \\ T_4 \\ T_5 = T_{hot} \end{Bmatrix} = \begin{Bmatrix} Q_1 \\ Q_2 = 0 \\ Q_3 = 0 \\ Q_4 = 0 \\ Q_5 \end{Bmatrix} \quad [48]$$

Equation 48 represents a system of five equations with five unknowns—T_2, T_3, T_4, Q_1 and Q_2. The unknown nodal temperature values are determined by solving the condensed system of equations in Equation 49. After solving the condensed system, it is then possible to calculate the heat flux unknowns using the remaining equations as in Equation 50.

$$\begin{bmatrix} K_{21}^{1} & K_{22}^{1}+K_{11}^{2} & K_{23}^{1}+K_{12}^{2} & K_{24}^{1}+K_{13}^{2} & K_{14}^{2} \\ K_{31}^{1} & K_{32}^{1}+K_{21}^{2} & K_{33}^{1}+K_{22}^{2} & K_{34}^{1}+K_{23}^{2} & K_{24}^{2} \\ K_{41}^{1} & K_{42}^{1}+K_{31}^{2} & K_{43}^{1}+K_{32}^{2} & K_{44}^{1}+K_{33}^{2} & K_{34}^{2} \end{bmatrix} \begin{Bmatrix} T_{cold} \\ T_2 \\ T_3 \\ T_4 \\ T_{hot} \end{Bmatrix} = \begin{Bmatrix} 0 \\ 0 \\ 0 \end{Bmatrix} \quad [49]$$

$$\begin{bmatrix} K_{11}^{1} & K_{12}^{1} & K_{13}^{1} & K_{14}^{1} & 0 \\ 0 & K_{41}^{2} & K_{42}^{2} & K_{43}^{2} & K_{44}^{2} \end{bmatrix} \begin{Bmatrix} T_{cold} \\ T_2 \\ T_3 \\ T_4 \\ T_{hot} \end{Bmatrix} = \begin{Bmatrix} Q_1 \\ Q_5 \end{Bmatrix} \quad [50]$$

Through extension of the concepts above, the finite element formulation can be carried out for the other governing equations such as pure mechanical or thermal-electrical boundary value problems. In addition, other isoparametric element shapes or higher order elements can be implemented. As more elements are added to the mesh, the number of unknown values increases; however, the assembly and solution phases of the formulation remain the same. After solving the resulting system for the primary variables (displacements, temperatures, etc), the final step in the finite element analysis is post processing of the results to compute secondary variables (stress, strain, heat flux, etc).

APPENDIX B. ISOPARAMETRIC FINITE ELEMENTS

The main element used in this research is a linear, 4 noded tetrahedral element as shown in Figure B.1. This isoparametric element is shown in its natural coordinate system, with its interpolation functions shown in Equation 51 [81]. In addition, the approximation function is shown in Equation 52, where T_j represents the temperature at node j. This element is used to model the carbon foam geometry as well as any infiltration materials since the tetrahedral is efficient at filling volumes with curved surfaces.

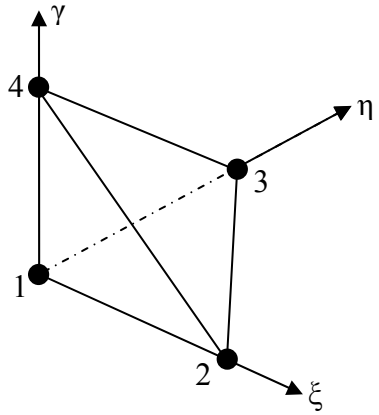

Figure B.1. Four node linear tetrahedral master element in natural coordinates

$$\begin{aligned}\psi_1 &= 1-\xi-\eta-\gamma \\ \psi_2 &= \xi \\ \psi_3 &= \eta \\ \psi_4 &= \gamma\end{aligned} \qquad [51]$$

$$T^e = \sum_{j=1}^{N} \psi_j T_j = \psi_1 T_1 + \psi_2 T_2 + \psi_3 T_3 + \psi_4 T_4 = (1-\xi-\eta-\gamma)T_1 + \xi T_2 + \eta T_3 + \gamma T_4 \qquad [52]$$

The second element shape used in this research is a linear wedge element, shown in Figure B.2 with its natural coordinate system. Its associated interpolation functions are shown in Equation 53, while the approximation for temperature T_j at any node j appears in Equation 54 [81]. This shape is used to define coatings on the surface of the carbon foam that were generated based on the original isosurface triangulation.

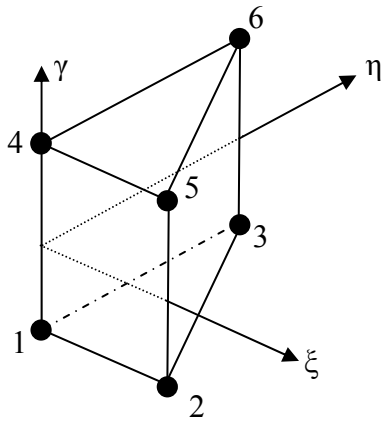

Figure B.2. Six node linear wedge master element in natural coordinates

$$\psi_1 = \frac{1}{2}(1-\xi-\eta)(1-\gamma) \qquad \psi_4 = \frac{1}{2}(1-\xi-\eta)(1+\gamma)$$
$$\psi_2 = \frac{1}{2}\xi(1-\gamma) \qquad \psi_5 = \frac{1}{2}\xi(1+\gamma) \qquad [53]$$
$$\psi_3 = \frac{1}{2}\eta(1-\gamma) \qquad \psi_6 = \frac{1}{2}\eta(1+\gamma)$$

$$T^e = \sum_{j=1}^{N} \psi_j T_j = \psi_1 T_1 + \psi_2 T_2 + \psi_3 T_3 + \psi_4 T_4 + \psi_5 T_5 + \psi_6 T_6$$
$$= \frac{1}{2}(1-\xi-\eta)(1-\gamma)T_1 + \frac{1}{2}\xi(1-\gamma)T_2 + \frac{1}{2}\eta(1-\gamma)T_3 \qquad [54]$$
$$+ \frac{1}{2}(1-\xi-\eta)(1+\gamma)T_4 + \frac{1}{2}\xi(1+\gamma)T_5 + \frac{1}{2}\eta(1+\gamma)T_6$$

The final element shape used in this research is a quadratic hexahedral element, shown in Figure B.3 with its natural coordinate system. Its associated interpolation functions are shown in Equation 55, while the approximation for temperature T_j at any node j appears in Equation 56 [81]. Quadratic hexahedrals are used as host elements when introducing loads into the VOI models. A higher order element was chosen here to provide more information in interpolating the response of the embedded elements.

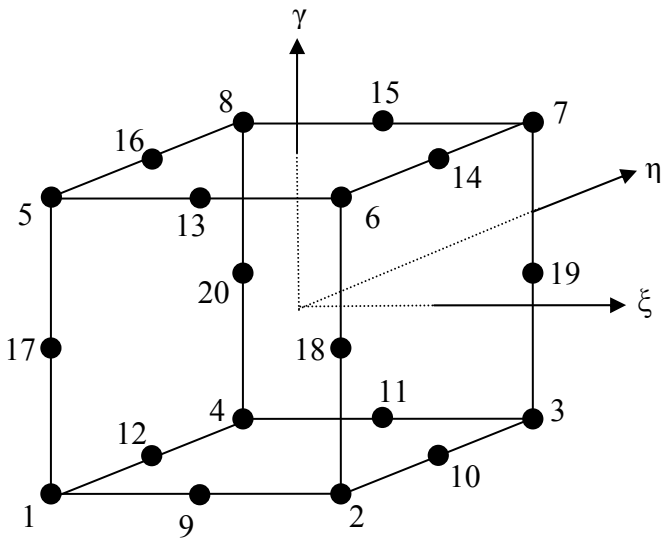

Figure B.3. Twenty node quadratic hexahedral master element in natural coordinates

$$
\begin{aligned}
\psi_1 &= -\frac{1}{8}(1-\xi)(1-\eta)(1-\gamma)(2+\xi+\eta+\gamma) & \psi_{11} &= \frac{1}{4}(1-\xi)(1+\xi)(1+\eta)(1-\gamma)\\
\psi_2 &= -\frac{1}{8}(1+\xi)(1-\eta)(1-\gamma)(2-\xi+\eta+\gamma) & \psi_{12} &= \frac{1}{4}(1-\eta)(1+\eta)(1-\xi)(1-\gamma)\\
\psi_3 &= -\frac{1}{8}(1+\xi)(1+\eta)(1-\gamma)(2-\xi-\eta+\gamma) & \psi_{13} &= \frac{1}{4}(1-\xi)(1+\xi)(1-\eta)(1+\gamma)\\
\psi_4 &= -\frac{1}{8}(1-\xi)(1+\eta)(1-\gamma)(2+\xi-\eta+\gamma) & \psi_{14} &= \frac{1}{4}(1-\eta)(1+\eta)(1+\xi)(1+\gamma)\\
\psi_5 &= -\frac{1}{8}(1-\xi)(1-\eta)(1+\gamma)(2+\xi+\eta-\gamma) & \psi_{15} &= \frac{1}{4}(1-\xi)(1+\xi)(1+\eta)(1+\gamma)\\
\psi_6 &= -\frac{1}{8}(1+\xi)(1-\eta)(1+\gamma)(2-\xi+\eta-\gamma) & \psi_{16} &= \frac{1}{4}(1-\eta)(1+\eta)(1-\xi)(1+\gamma)\\
\psi_7 &= -\frac{1}{8}(1+\xi)(1+\eta)(1+\gamma)(2-\xi-\eta-\gamma) & \psi_{17} &= \frac{1}{4}(1-\gamma)(1+\gamma)(1-\xi)(1-\eta)\\
\psi_8 &= -\frac{1}{8}(1-\xi)(1+\eta)(1+\gamma)(2+\xi-\eta-\gamma) & \psi_{18} &= \frac{1}{4}(1-\gamma)(1+\gamma)(1+\xi)(1-\eta)\\
\psi_9 &= \frac{1}{4}(1-\xi)(1+\xi)(1-\eta)(1-\gamma) & \psi_{19} &= \frac{1}{4}(1-\gamma)(1+\gamma)(1+\xi)(1+\eta)\\
\psi_{10} &= \frac{1}{4}(1-\eta)(1+\eta)(1+\xi)(1-\gamma) & \psi_{20} &= \frac{1}{4}(1-\gamma)(1+\gamma)(1-\xi)(1+\eta)
\end{aligned}
\qquad [55]
$$

$$
\begin{aligned}
T^e = \sum_{j=1}^{N}\psi_j T_j = {} & \psi_1 T_1 + \psi_2 T_2 + \psi_3 T_3 + \psi_4 T_4 + \psi_5 T_5 \\
& + \psi_6 T_6 + \psi_7 T_7 + \psi_8 T_8 + \psi_9 T_9 + \psi_{10} T_{10} \\
& + \psi_{11} T_{11} + \psi_{12} T_{12} + \psi_{13} T_{13} + \psi_{14} T_{14} + \psi_{15} T_{15} \\
& + \psi_{16} T_{16} + \psi_{17} T_{17} + \psi_{18} T_{18} + \psi_{19} T_{19} + \psi_{20} T_{20}
\end{aligned}
\qquad [56]
$$

APPENDIX C. EFFECTIVE PROPERTY FORMULATION

C.1. Effective Mechanical Stiffness

Strain energy density is calculated as the dot product of the individual stress and strain components at each integration point in the model as described by Equation 57 [76, 77]. The total strain energy for that integration point is calculated by multiplying by the integration volume as in Equation 58.

$$U_o^{\text{int}} = \frac{1}{2}\sigma_{ij}\varepsilon_{ij} \qquad [57]$$

$$U^{\text{int}} = U_o^{\text{int}} V^{\text{int}} = \frac{1}{2}\sigma_{ij}\varepsilon_{ij} V^{\text{int}} \qquad [58]$$

In order to reduce boundary effects near the loading surfaces, a volume sufficiently removed from the boundary is identified, and the total strain energy for the model is calculated as the sum of the individual element total strain energy values. Using the identified region's dimensions, the total volume, both solid and pore phases, is used to calculate the strain energy density as in Equation 59.

$$U_o^{total} = \frac{\sum U^{\text{int}}}{V^{solid} + V^{pore}} \qquad [59]$$

This strain energy density represents the total work done by the system when loaded by a compressive displacement load. Furthermore, work is also represented as the area under

the characteristic stress-strain curve for this compressive loading which induces a global strain according to Equation 60. Therefore, using the assumption of linear stress-strain curve, an effective modulus in the loading direction is calculated using the total strain energy density of the model and the global strain state in Equation 61.

$$\varepsilon = \frac{\delta}{L} \qquad [60]$$

$$\overline{E} = \frac{2U_o^{total}}{\varepsilon^2} \qquad [61]$$

C.2. Effective Thermal Conductivity

This method is based on the one dimensional form of Fourier's law and results in an effective property characteristic of the thermal gradient in the loading direction [78, 79]. Initially, a volume weighted heat flux vector is identified at each integration point using Equation 62.

$$\vec{q}_w^{\,\text{int}} = \vec{q}^{\,\text{int}} V^{\,\text{int}} \qquad [62]$$

In order to reduce boundary effects near the loading surfaces, a volume sufficiently removed from the boundary is identified, and the total heat flux vector for the model is calculated as the sum of the individual volume weighted heat flux vectors. Using the identified region's dimensions, the total volume, both solid and pore phases, is used to calculate the average heat flux vector as in Equation 63.

$$\vec{q}_{average} = \frac{\sum \vec{q}_w^{\,\mathrm{int}}}{V^{solid} + V^{pore}} \qquad [63]$$

The applied temperature gradient is calculated using Equation 64 based on temperature boundary conditions. Using the appropriate average heat flux component and the applied temperature gradient, an effective thermal conductivity in the loading direction is calculated using Equation 65 based on the one dimensional form of Fourier's law.

$$\frac{dT}{dx} = \frac{T^{hot} - T^{cold}}{L} \qquad [64]$$

$$\overline{k} = q_{average} \frac{dx}{dT} \qquad [65]$$

C.3. Effective Electrical Conductivity

This method is based on the one dimensional form of Ohm's law and results in an effective property characteristic of the applied electric potential gradient in the loading direction [80]. Initially, a volume weighted current density vector is identified at each integration point using Equation 66.

$$\vec{J}_w^{\,\mathrm{int}} = \vec{J}^{\,\mathrm{int}} V^{\mathrm{int}} \qquad [66]$$

In order to reduce boundary effects near the loading surfaces, a volume sufficiently removed from the boundary is identified, and the total electric current density vector for

the model is calculated as the sum of the individual volume weighted current density vectors. Using the identified region's dimensions, the total volume, both solid and pore phases, is used to calculate the average electric current density vector as in Equation 67.

$$\vec{J}_{average} = \frac{\sum \vec{J}_{w}^{\,\mathrm{int}}}{V^{solid} + V^{pore}} \qquad [67]$$

The applied electric field is calculated using Equation 68 based on potential gradient. Using the appropriate average electric current density component and the applied electric field, an effective electric conductivity in the loading direction is calculated using Equation 69 based on the one dimensional form of Ohm's law.

$$E = -\frac{d\varphi}{dx} \qquad [68]$$

$$\overline{\sigma^{e}} = -J_{average}\frac{dx}{d\varphi} \qquad [69]$$

APPENDIX D. COMPUTATIONAL RESOURCES

			Mesh Statistics			CPU Time Required (min)			
Illustration	**Description**	**Analysis Type**	**Elements**	**Nodes**	**Total DOF**	**Input**	**Analysis**	**Memory (GB)**	**Diskspace (GB)**
Section 4.1	Shallow Crack	Mechanical	506,383	146,588	439,764	12.7	52.3	7.10	12.68
	Filled	Mechanical	606,376	196,588	589,764	17.4	54.5	8.52	15.58
	Medium Crack	Mechanical	506,383	146,588	439,764	12.6	52.3	7.10	12.68
	Filled	Mechanical	606,376	196,588	589,764	17.7	55.4	8.52	15.58
	Deep Crack	Mechanical	506,383	146,588	439,764	13.1	53.4	7.10	12.68
	Filled	Mechanical	606,376	196,588	589,764	17.5	56.4	8.52	15.58
Section 4.2	Uncoated	Thermal	498,383	109,586	109,586	1.5	795.9	1.88	0.19
		Thermo-mechancial	506,383	146,588	439,764	4.9	351.4	5.33	12.71
	Cu Coat	Thermal	598,376	159,586	159,586	1.8	1,487.2	2.30	0.30
		Thermo-mechancial	606,376	196,588	589,764	4.5	840.6	7.38	13.04
	PLLA Coat	Thermal	598,376	159,586	159,586	1.8	908.2	2.30	0.30
		Thermo-mechancial	606,376	196,588	589,764	4.3	176.4	7.38	13.04
Section 5.1	$1^m \equiv Z^L$ Orientation	Mechanical	1,728,224	684,513	2,053,539	39.6	134.7	9.99	19.12
	$2^m \equiv Z^L$ Orientation	Mechanical	1,728,224	684,513	2,053,539	39.5	212.4	9.99	19.12
	$3^m \equiv Z^L$ Orientation	Mechanical	1,728,224	684,513	2,053,539	39.0	133.7	9.99	19.12
Section 5.2	PLLA Infiltration	Mechanical	9,169,914	1,821,889	5,465,667	91.3	3,471.6	100.43	301.38
Section 5.3	Uncoated	Thermal	1,667,690	381,697	381,697	4.9	10.5	3.26	0.55
		Thermo-mechancial	1,728,224	684,513	2,053,539	15.2	45.0	11.52	19.22
	Cu Coat	Thermal	2,464,006	779,799	779,799	7.3	19.3	5.18	1.41
		Thermo-mechancial	2,524,540	1,082,615	3,247,845	33.0	81.7	17.11	31.96
	Small Scale Defect	Thermal	2,464,006	779,992	779,992	7.3	16.7	9.22	1.45
		Thermo-mechancial	2,524,540	1,082,808	3,248,424	33.2	81.4	16.51	31.58
	Large Scale Defect	Thermal	2,464,006	779,799	779,799	7.4	22.1	5.18	1.41
		Thermo-mechancial	2,524,540	1,082,615	3,247,845	32.9	87.8	17.11	31.96
Section 5.4	Uncoated	Thermal-electrical	1,667,690	381,697	763,394	15.8	67.5	5.85	3.11
	5 μm Cu Coat	Thermal-electrical	2,065,848	580,748	1,161,496	20.4	100.6	5.30	5.93
	10 μm Cu Coat	Thermal-electrical	2,464,006	779,799	1,559,598	25.1	135.0	9.47	9.44
Section 6.1	Cu Coat	Thermal-electrical	1,982,309	697,268	1,394,536	7.8	33.4	13.17	7.02
		Thermo-mechancial	2,033,218	939,340	2,818,020	50.4	121.0	25.08	32.76

VITA

Melanie Diane Sarzynski entered the Department of Mechanical Engineering at Texas A&M University in 1998. Her undergraduate education included a two-term engineering co-op assignment with a semiconductor fabrication facility at Texas Instruments in Dallas, Texas. In the summer of 2002, she further diversified her educational experiences by participating in the Undergraduate Research Program under the direction of Professor O. Ochoa.

Upon completion of her Bachelor of Science degree in December 2002, she expanded her summer research project for a Master of Science degree in Mechanical Engineering at Texas A&M University. During the course of her studies, she received honorable mention in the NSF Graduate Research Fellowship competition acknowledging her research potential. She received her Master's degree in December 2003 upon completion of her research project entitled *Carbon Foam Characterization: Sandwich Flexure, Tensile and Shear Response*.

Continuing at Texas A&M University, Melanie built upon her previous research in carbon foams. She spent a summer working with researchers at the Air Force Research Laboratory at Wright-Patterson Air Force Base in Dayton, OH gaining valuable experience in processing of carbon foams. Working closely with the carbon foam community throughout her studies, she received her Ph. D. in Mechanical Engineering in May 2008 under the continual guidance of Professor O. Ochoa.

Melanie can be reached at:

Melanie Sarzynski, c/o Ozden O. Ochoa
Department of Mechanical Engineering, Texas A&M University
MS 3123-TAMU
College Station, TX 77843-3123